FACULTY OF ENGINEERING AND ARCHITECTURE

Targeted drug delivery for liver cancer: modelling the impact of cancer burden on the particle distribution in a patient-specific cirrhotic liver

Tim Bomberna
Student number: 01404812

Supervisors: Prof. dr. ir. Charlotte Debbaut, Prof. dr. ir. Patrick Segers
Counsellor: Ghazal Adeli Koudehi

Master's dissertation submitted in order to obtain the academic degree of
Master of Science in Biomedical Engineering

Academic year 2018-2019

GHENT UNIVERSITY

FACULTY OF ENGINEERING AND ARCHITECTURE

Targeted drug delivery for liver cancer: modelling the impact of cancer burden on the particle distribution in a patient-specific cirrhotic liver

Tim Bomberna
Student number: 01404812

Supervisors: Prof. dr. ir. Charlotte Debbaut, Prof. dr. ir. Patrick Segers
Counsellor: Ghazal Adeli Koudehi

Master's dissertation submitted in order to obtain the academic degree of
Master of Science in Biomedical Engineering

Academic year 2018-2019

GHENT UNIVERSITY

Permission of use on loan

"The author gives permission to make this master dissertation available for consultation and to copy parts of this master dissertation for personal use. In all cases of other use, the copyright terms have to be respected, in particular with regard to the obligation to state explicitly the source when quoting results from this master dissertation."

Tim Bomberna, May 2019

Acknowledgement

First and foremost, I want to express my sincere gratitude to my supervisors Prof. Charlotte Debbaut and Prof. Patrick Segers. Ever since setting foot in her office way back in April of last year, Prof. Charlotte Debbaut has guided me every step of the way. She has supported my ideas and reinforced them with her expertise. Prof. Patrick Segers has offered me advice and counselling throughout my Master's degree. I want to thank them both for always being close-by and readily available.

A thesis requires a close collaboration with several people. I want to thank my counsellor Ghazal Adeli Koudehi for her support. I wish you the best in the remainder of your career and I'm absolutely sure you'll finish your doctoral degree in style. Furthermore, I want to thank Charlotte Claerebout, as her work was crucial for my thesis to succeed. And I want to thank Lowie Swaenepoel, with whom I had many fruitful discussions about our work. In particular, I want to thank Prof. Stefaan de Smedt, who introduced me to the world of targeted drug delivery. If it wasn't for his passionate lectures, I probably never would've discovered this topic.

In a way, this thesis is a culmination of a journey I set on about five years ago. Back then, I never could've imagined I would actually make it this far. But as it turns out, you can surprise even yourself when you're surrounded by the right people. I want to thank all of my friends and family for the undying support they have offered me throughout these years. In particular, I want to thank Nele, for always being by my side in the face of adversity. It's no easy feat to support someone as intensely and brilliantly as you do, and I'll never take it for granted.

This thesis is dedicated to Georgette and Christine, who fought valiantly but lost their battle with cancer. The world you left behind is shaped by your ideals and values, and is a better one for it.

Tim Bomberna
26th of May, 2019

Abstract

HCC is the third leading cause of cancer-related deaths worldwide. For the intermedium stage, the preferred treatment option is transarterial therapy. The main goal of transarterial therapies is to cut off the blood supply of the tumour tissue by local administration of embolizing particles. Since tumour tissue in the liver is generally fed by arterial blood, obstruction of these arteries will lead to starvation and tumour cell death. Numerical modelling plays an important role in the planning of these therapies as it is typically used to simulate the particle distribution in a patient-specific vasculature and to determine the influence of certain parameters that are variable in the clinic (e.g. catheter location, catheter orientation, particle type, etc.). By optimizing these parameters, the objective is to maximize the deposition of particles at the tumour tissue and minimize the leak to healthy tissue. Since particle distribution tends to mimic overall flow distribution, the choice of boundary conditions in these numerical models in essential. While in the past Murray's law has often been used, this thesis implements an alternate boundary condition that more accurately describes the impact of cancer burden or, more specifically, the impact of the sizes and the distribution of tumour nodules throughout the liver. The particle distribution for eleven different cancer scenarios is compared with Murray's law. The results show that cancer burden has a great impact on the particle distribution in the arterial network. By extent, this means that the choice of boundary conditions is crucial. Going forward, a clear choice between Murray's law and the alternative discussed here should be made.

Key words: hepatocellular carcinoma, targeted drug delivery, boundary conditions, cancer burden

Targeted drug delivery for liver cancer: modelling the impact of cancer burden on the particle distribution in a patient-specific cirrhotic liver

Tim Bomberna

Supervisor(s): Charlotte Debbaut, Patrick Segers
Counsellor: Ghazal Adeli Koudehi

Abstract— **Numerical models play an important role in the planning of transarterial therapies for the treatment of hepatocellular carcinoma (HCC). As particle distribution tends to match flow distribution, the choice of boundary conditions in these models is crucial. This thesis proposes an alternative boundary condition (BC) to Murray's law. This BC aims to describe the impact of cancer burden on flow and particle distribution.**

Keywords—**Targeted drug delivery, hepatocellular carcinoma, boundary conditions**

I. Hepatocellular carcinoma

Hepatocellular carcinoma (HCC) is the most common liver malignancy in the world and the third leading cause of cancer-related deaths worldwide. Due to its high prevalence, HCC has become a global economic burden on society. Risk factors for HCC include Hepatitis B (HBV) infection, Hepatitis C infection (HCV), excessive alcohol intake and Non-Alcoholic Fatty Liver Disease (NAFLD). HCC regularly develops from cirrhosis, although it may also develop in absence of cirrhosis in some cases. In this thesis, a patient-specific cirrhotic liver is considered.

II. Targeted drug delivery

Targeted drug delivery aims to maximize the dose delivery to tumour tissue and to minimize the leak to healthy tissue. At the intermedium stage of HCC, transarterial therapies are the preferred choice of treatment. The objective of transarterial chemoembolization (TACE) and transarterial radioembolization (TARE) is to inject embolizing particles in the feeding arteries of the tumour. Obstruction of these arteries will lead to starvation of the tumour tissue and tumour cell death.

However, the arterial network is often tortuous, especially in cirrhotic livers, which makes it difficult for catheters to advance in these arteries. Therefore, particles are injected at a more upstream point in the hepatic vasculature. The goal is then to manipulate these particles in such a way that they reach their downstream target (the tumour tissue) in as high a fraction as possible. At the injection site, several variable parameters (e.g. catheter location, catheter orientation, particle type, etc.) are under control of the clinician. The impact of each of these parameters on the downstream particle distribution is estimated through numerical modelling. Once these numerical results have identified the parameters that are most effective in steering the drug carriers towards the tumour tissue, the clinician can attempt to mimic these conditions and use these parameters to increase the efficiency of the treatment.

As is clear, numerical models play a crucial role in the planning of these transarterial therapies as they are used to predict the particles' route from injection site to target site. However, as particle distribution tends to mimic flow distribution, the choice of boundary conditions in these models is key. In this thesis, an alternative boundary condition proposed by Aramburu et al [1] is compared to Murray's law.

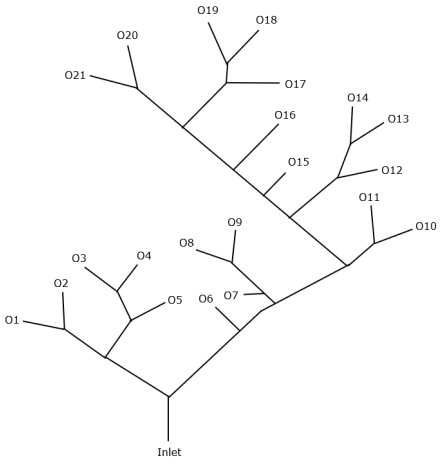

Fig. 1. Schematic overview of the arterial network of the liver.

III. Geometry and Mesh Generation

Detailed datasets of a patient-specific cirrhotic liver were obtained in two succinct steps: vascular corrosion casting and micro-CT-imaging. Segmentation of the arteries was performed by Claerebout. A 3D model of the arterial network was imported into 3-matic (Materialise, Leuven, Belgium) to generate the surface mesh. A schematic outline of the arterial network is visualized in Figure 1. The volume mesh was generated in ICEM CFD (Ansys, Canonsburg, USA). The optimal mesh density was determined through a mesh sensitivity analysis. The mesh of 9 million elements was imported in ANSYS Fluent (Ansys, Canonsburg, USA).

IV. Boundary Conditions

The alternative boundary conditions were defined according to the arterial perfusion model proposed by Aramburu et al [1]. For these boundary conditions, a constant velocity was imposed at each of the outlets of the computational domain. The key insight of [1] is that the arterial perfusion of tumour tissue is over

four times as high than the arterial perfusion of non-cancerous tissue. The flow rate through outlet m (which perfuses liver segment s) can be calculated as:

$$q_{m,s} = x_{n,s}(K_{h,s} + K_{c,s})q_{0,s} \quad (1)$$

In Equation 1, $K_{h,s}$ and $K_{c,s}$ are macroscopic perfusion parameters that depend on the tumour burden of segment s, $q_{0,s}$ is the arterial flow to the healthy liver segment s and $x_{n,s}$ is the flow rate ratio that is determined by the degree of branching n within a certain segment s. These volume and flow measures are computed on a patient-specific basis for the cirrhotic liver considered in this study. To determine the tumour burden, several hypothetical cancer scenarios were considered varying in the distribution and total volume of tumour nodules.

The difference with Murray's law is that Murray's law does not differentiate between the different cancer scenarios. Flow distribution according to Murray's law is based only on the geometric properties of the arterial network and not on the metabolic demands of the tissue.

Figure 2 compares the flow distribution as calculated with Murray's law to the flow distribution as calculated with the arterial perfusion model (under the assumption that tumours were constricted to Segment 4). As is obvious, the discrepancy in flow distribution for the two boundary conditions is large. The impact on particle distribution will be discussed in VI.

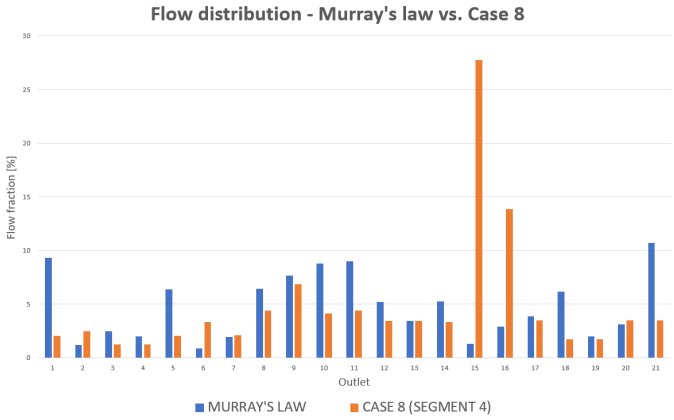

Fig. 2. Comparing flow distribution as obtained with Murray's law with flow distribution as obtained with the arterial perfusion model.

V. Computer Simulations

Fourteen one-way steady simulations were run: eleven different cancer scenarios based on the alternative boundary condition, one simulation based on Murray's law and two repeated cancer scenarios for different radioembolization treatment particles. To this end, the Discrete Phase Model (DPM) in ANSYS Fluent was employed.

VI. Results

The results of the computer simulations were exported to CFD-Post and then imported into Matlab to generate Particle Release Maps (PRMs). PRMs are helpful visual aids in the evaluating the target-specificity of the proposed therapy. These

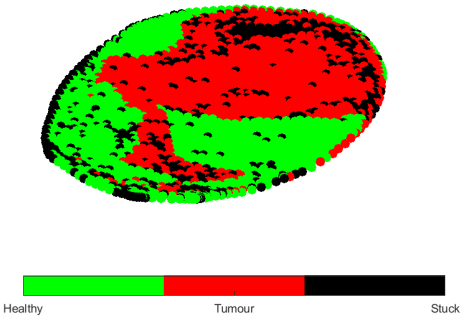

Fig. 3. Tumours constricted to Segment 4. Flow distribution calculated with arterial perfusion model (moderate burden).

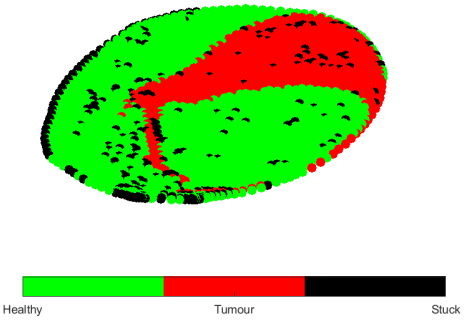

Fig. 4. Tumours constricted to Segment 4. Flow distribution calculated with Murray's Law.

maps visualize the areas of the inlet plane where particles need to objected to deposit in a certain type of tissue, i.e. healthy or cancerous.

In Figure 3, the PRM is generated for a cancer scenario in which all tumour nodules were constricted to Segment 4 of the liver. The cancer scenario was modelled using the arterial perfusion model. The green area outlines the region of the injection plane where particles need to be injected to deposit in the healthy tissue (which is, of course, undesirable). The red area outlines the region of the injection plane where particles need to be injected to deposit in the tumour tissue. In Figure 4, the PRM is generated using Murray's law as a boundary condition.

As is clear from Figures 3 and 4, the borders of the red and green regions depend on the chosen boundary condition. This creates an unwanted ambiguity for the clinician in charge. Therefore, going forward, a clear choice regarding the use of boundary conditions must be made. As patient-specificity is a key factor in the success of these therapies, the arterial perfusion model proposed by Aramburu et al [1] is the author's preferred choice of boundary condition.

References

[1] J. Aramburu, R. Anton, A. Rivas, J. C. Ramos, B. Sangro and J. I. Bilbao, "Liver cancer arterial perfusion modelling and CFD boundary conditions methodology: a case study of the haemodynamics of a patient-specific hepatic artery in literature-based healthy and tumour-bearing liver scenarios," *International Journal for Numerical Methods in Biomedical Engineering*, vol. 32, no. 11, 2016, doi: 10.1002/cnm.2764.

Contents

List of Figures

List of Tables

List of Abbreviations

Chapter 1: Hepatocellular carcinoma

HCC	Hepatocellular Carcinoma
TACE	Transarterial Chemoembolization
TARE	Transarterial Radioembolization
HBV	Hepatitis B Virus
HCV	Hepatitis C Virus
NAFLD	Non-alcoholic Fatty Liver Disease
ALD	Alcoholic Liver Disease
CT	Computed Tomography
MRI	Magnetic Resonance Imaging
BCLC	Barcelona Clinic Liver Classification
RBA	Radio-frequency Ablation
SIRT	Selective Intra-arterial Radiation Therapy

Chapter 2: State of the art

EPR	Enhanced Permeation and Retention
PEG	Polyethylene glycol
RES	Reticulo-endothelial system
DEB	Drug-eluding beads
DOX	Doxorubicin
Y	Yttrium
Tc	Technetium
MAA	Macro-aggregated albumin
SPECT	SPECT
Ho	Holmium
CFD	Computational Fluid Dynamics
PRM	Particle Release Map
SMC	Smart Micro Catheter
MSA	Medicine Supply Apparatus
ATM	Angled Tip Microcatheter
CMMP	Computational Medical Management Program

Chapter 3: Geometry and Mesh Generation

HA	Hepatic Artery
PV	Portal Vein
HV	Hepatic Vein

Chapter 4: Computer Simulations

DPM	Discrete Phase Model
PHA	Proper Hepatic Artery

Chapter 5: Boundary Conditions

RHA	Right Hepatic Artery
LHA	Left Hepatic Artery
DPI	Doppler Perfusion Index

List of Symbols

Chapter 4: Computer Simulations

u	Fluid velocity
ρ	Density
p	Fluid pressure
τ	Shear stress
F_G	Gravitational force
μ	Dynamic viscosity
$\dot{\gamma}$	Shear rate
μ_0	Minimum viscosity
μ_∞	Asymptotic viscosity
τ_0	Apparent yield stress
λ	Shear stress modifier
u_p	Discrete particle velocity
ρ_p	Particle density
F_D	Drag force
d_p	Particle diameter
C_D	Drag coefficient
F	Fluid pressure force
Q	Volumetric flow rate
R	Vessel radius
v_{inlet}	Velocity at inlet plane
A_{inlet}	Area of inlet plane

Chapter 5: Boundary Conditions

$k_{1,s}$	Arterial perfusion of healthy tissue
$k_{2,s}$	Arterial perfusion of cancerous tissue in diseased liver
$k^{\star}_{1,s}$	Arterial perfusion of normal tissue in diseased liver
$q_{o,s}$	Arterial flow to healthy liver segment
$V_{o,s}$	Volume of healthy liver segment
$q_{c,s}$	Arterial flow to tumour (within a segment)
$V_{c,s}$	Tumour volume (within a segment)
q_s	Total arterial flow to segment
$\triangle V_s$	Alteration in liver volume due to regeneration or shrinkage
$K_{h,s}$	Macroscopic perfusion parameter 1
$K_{c,s}$	Macroscopic perfusion parameter 2
$q_{m,s}$	Arterial flow rate feeding outlet m
$x_{n,s}$	Flow rate ratio determined by degree of branching n in segment s

Part I

Literature Study

Chapter 1

Hepatocellular carcinoma

Hepatocellular carcinoma (HCC) is the most common primary liver malignancy in the world [20]. It is the third leading cause of cancer-related deaths worldwide. Due to its high prevalence, HCC has become a global economic burden on society [1].

This chapter will focus on HCC. Risk factors and prevention measures will be discussed. Treatment options, which depend on the stage of the cancer, will be listed. The main focus of thesis is two of those treatment options: transarterial chemoembolizaton (TACE) and transarterial radioembolization (TARE).

1.1 Epidemiology

HCC occurs more in men than in women with a ratio that typically varies between 2 and 4 among populations [4, 5]. As can be seen in Figure 1.1, in countries such as Vietnam, South Korea, Singapore, Portugal, Spain and France the ratio is remarkably high (even as high as 5 in Portugal) while, in countries such as Colombia, Mexico and Chile this ratio is much lower (well below 2). This discrepancy between genders is not well understood and may be attributed to several factors such as hormones, epigenetics, immune response and sex-specific exposure to risk factors (e.g. smoking and excessive alcohol intake) [3, 4].

Figure 1.2 displays the worldwide age-adjusted incidence rates of HCC. There is a distinct geographical pattern visible. Countries with the highest incidence are located in East and South-East Asia (e.g. China, South Korea, etc.) and Western and Central Africa (e.g. Senegal, Gambia, etc.) [1]. The incidence for China is notably high, while the incidence in America, Northern Europe and Oceania are particularly low [4]. The geographic pattern displayed in Figure 1.2 is such that it matches the distribution of infection with the Hepatitis B Virus (HBV) and Hepatitis C Virus (HCV) around the world. A strong link exists between HCC and HBV and HCV infections since HCC regularly develops from the cirrhotic liver, which, in itself, can develop from hepatitis infection [3].

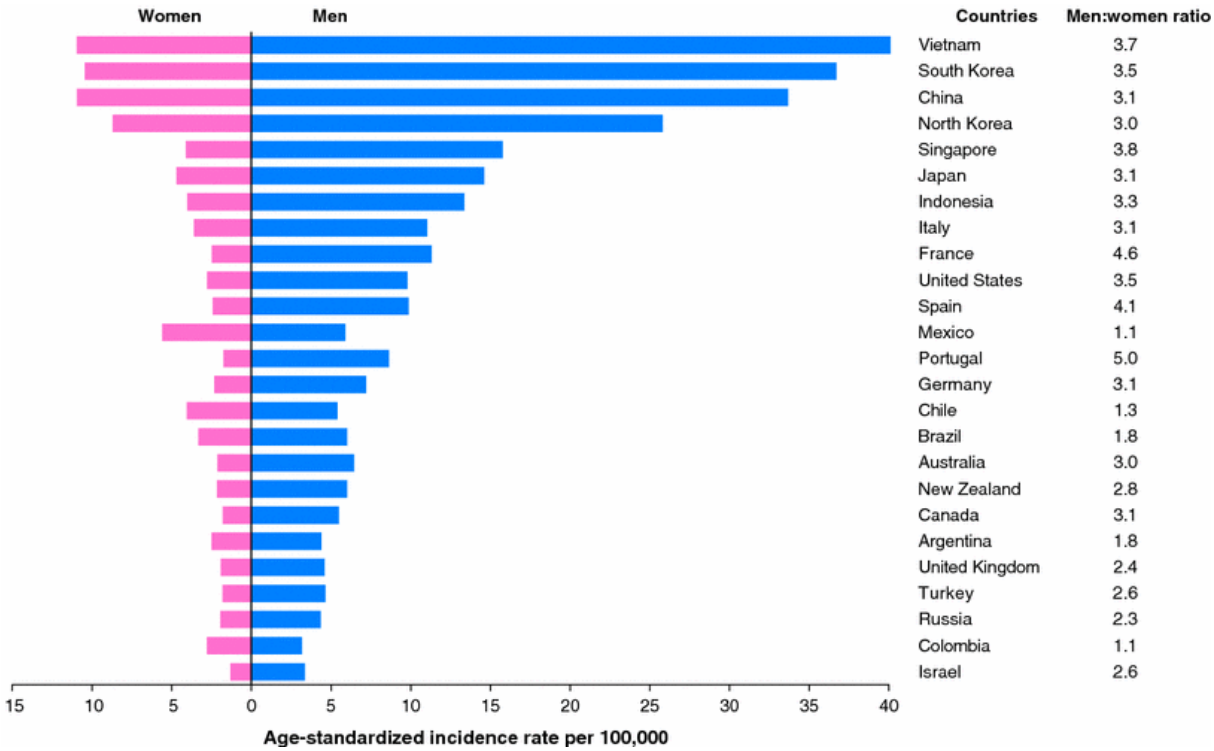

Figure 1.1: Gender comparison for age-adjusted incidence rates for HCC (per 100.000 persons) [3]

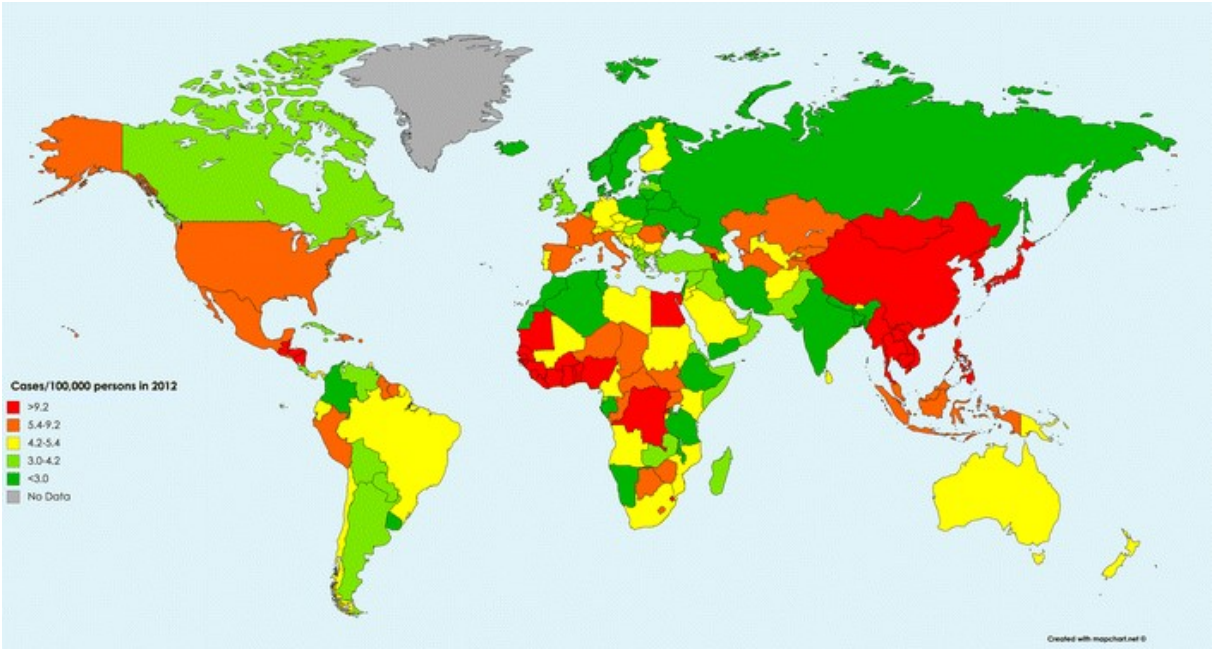

Figure 1.2: Worldwide age-adjusted incidence rates for HCC per 100.000 persons [3]

1.2 Risk factors

A multitude of risk factors are associated with the development of HCC, most notably HBV infection, HCV infection, excessive alcohol intake and non-alcoholic fatty liver disease (NAFLD) [4, 20].

Very frequently, HCC develops in patients with cirrhosis (70-90%). Cirrhosis in itself can be caused by hepatitis infection, smoking, excessive alcohol abuse and then progress onwards to HCC. This process is visualized in Figure 1.3. It should be noted that this scheme represents only one possible pathway of the development of HCC, since cirrhosis may develop even in the absence of hepatitis infection, for example due to smoking or excessive alcohol intake. However, HCC can also develop in the absence of cirrhosis. [4].

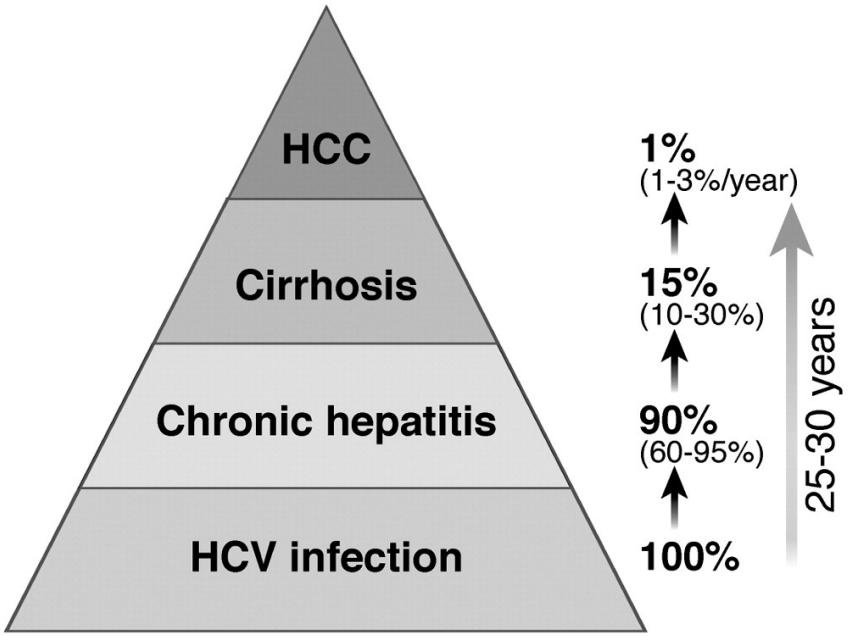

Figure 1.3: Development of HCC after HCV infection [4].

1.3 Prevention

Below, prevention measures for each of the four common risk factors for HCC as mentioned in Section 1.2 are discussed.

HBV infection

HBV infection accounts for about 50% of all reported HCC cases [21]. While steps have been made towards treating HBV infection as the global burden that it represents, full control over the infection is still unimaginable. To that end, measures need to be implemented in all corners of society. On the one hand, the goal must be to increase global health and halt the virus from spreading. This can be done, for example, by the overall

improvement of sanitation and living conditions and educating people about the risks of HBV. On the other hand, integration of the HBV vaccine into the global routine immunization program is a must. Effective antiviral agents need to be introduced to treat HBV patients who are already in the chronic stage of the disease [22].

HCV infection

HCV infection also significantly increases the risk for developing HCC. Infection with hepatitis C is mainly caused by intravenous drug use and sexual transmission. Blood transfusion was a significant problem in the past, but this risk has been reduced by the introduction of anti-HCV testing in blood samples [23].

Excessive alcohol intake (ALD)

Chronic alcoholic liver disease (ALD) is, of all the risk factors mentioned in this section, probably the one that benefits most from public awareness programs. Especially in the Western world, excessive alcohol intake is a growing problem [23]. An accompanying issue is that patients who develop HCC from ALD are often diagnosed relatively late, because they are often unaware of the risks associated with copious amounts of alcohol consumption. Patients with hepatitis infection tend to be diagnosed earlier on. As is explained in Section 1.4, the more the disease has progressed at the stage of diagnosis, the less likely chance of survival becomes [24].

Non-alcoholic fatty liver disease (NAFLD)

Obesity and diabetes are key influencing factors in the development of NAFLD into HCC. Therefore, physical exercise, strict diets and weight loss surgery are important prevention measures in these specific cases. Chemopreventive drugs are aimed at decreasing obesity-related inflammation and insulin resistance, but these are still under research [24].

1.4 Diagnosis

Early diagnosis, as will be stressed in Section 1.5, is important to increase survival odds. A guideline for the steps that need to be taken in order to make a proper diagnosis of HCC is given in Figure 1.4.

At a certain minimal size, lesions are generally hard to assess, particularly if they are less than 1 cm. For these small lesions, surveillance by ultrasound every three or six months is recommended to check whether the lesion is stable or enlarging [25, 5].

For lesions larger than 1 cm, the first attempt at a diagnosis is made with non-invasive imaging. The two imaging modalities that are mostly used to diagnose HCC are four-phase CT contrast (unenhanced, arterial, venous and delayed) or dynamic contrast enhanced

MRI [5]. Since tumours are mainly fed by the arterial system, the presence of a tumour can be indicated on each of these modalities by bright spots in the arterial phase, followed by washout of contrast in the delayed or venous phase. A typical example of a contrast MRI that confirms the presence of such a tumour is given in Figure 1.5. Panel (a) shows the arterial phase, where the hyperenhanced region shows the tumour mass, while panel (b) shows the venous phase [6]. The advantages and disadvantages of these two modalities are well-known: while MRI provides the better contrast, it also more expensive and prone to artefacts than CT. Which modality is used for the first round of diagnosis, is up to the clinician. In the cases where one of these imaging modalities does not provide enough information for diagnosis, the other modality (CT/MRI) can be used. If atypical features for the cancer are found, or if the CT/MRI studies give discordant findings, then an invasive liver biopsy must be performed to make a final diagnosis [5]. If the biopsy returns negative, then regular surveillance is opted to check any changes in the cancer. If the biopsy returns positive, then a fitting treatment based on the specific case must be considered. An overview of the various treatment option is give in Section 1.5.

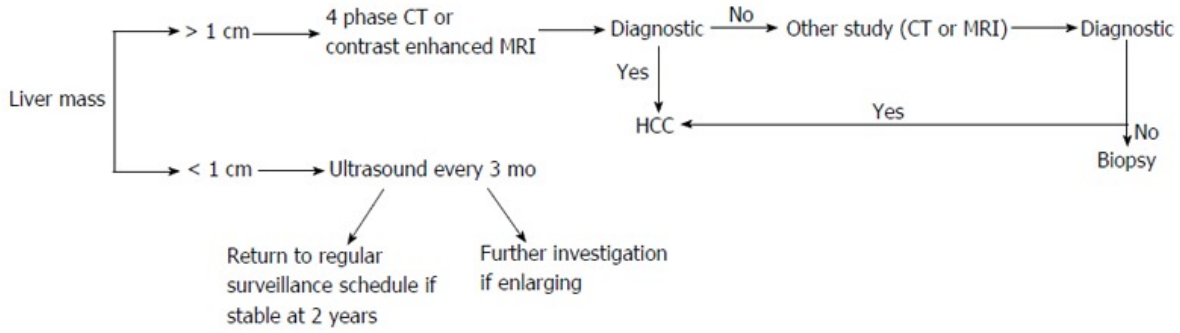

Figure 1.4: Diagnosis guidelines for HCC [5].

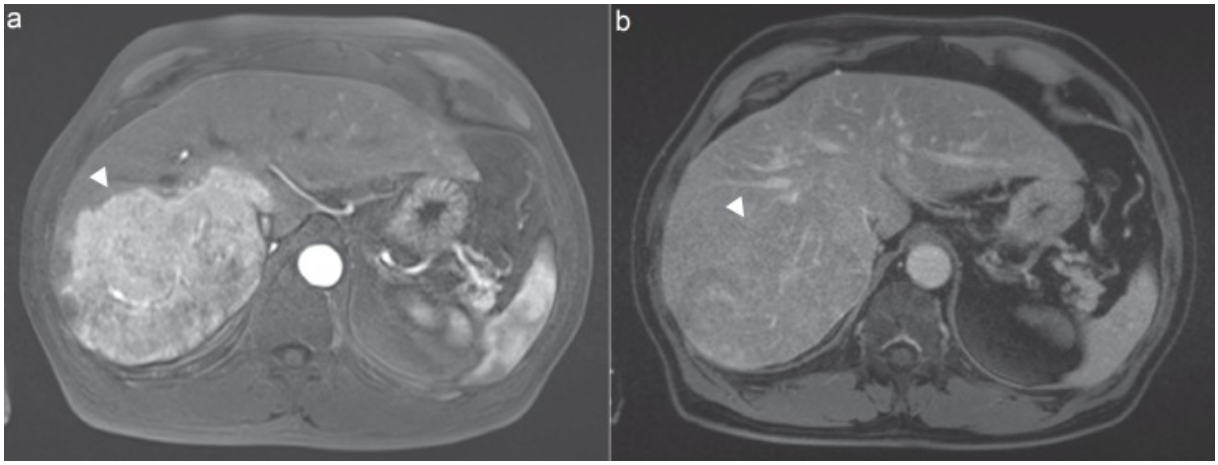

Figure 1.5: Arterial phase (a) and venous phase (b) for contrast MRI of HCC [6].

1.5 Treatment

One of the most important factors in treating HCC is evaluating to what stage the cancer has developed. To this end, the Barcelona Clinical Liver Cancer (BCLC) staging system has been introduced, to quantify the prognosis of the disease and adapt the treatment accordingly [21]. As is clear from Figure 1.6, the BCLC staging system is divided up in four subcategories, ranked A to D for severity of the condition.

Very early-stage HCC is difficult to diagnose since it is presented by only a single nodule with a diameter less than 2 cm. Early-stage HCC is characterized by a larger nodule or 3 smaller nodules, with each less than 3 cm in diameter. For patients with a single nodule, the preferred treatment is surgical resection. However, it is important to consider the functional capacity of the remaining liver volume after the procedure. If patients with cirrhosis are presented with no portal hypertension and normal bilirubilin levels, then this is a good predictor for sufficient hepatic reserve and resection presents itself as a valid option. Although survival rates are generally high here, recurrence rates are also significant since the tumour mass was surgically removed but the underlying chronic condition was not addressed. If resection is not an option, transplantation may be opted. The downsides of transplantation are well-known: along with a need for immunosuppressive therapy, there is organ scarcity and generally very long waiting lists. If transplantation is not possible, then radio-frequency ablation (RBA) may be considered. In the rarer non-cirrhotic cases, patients usually have a well-preserved liver function and and a lower risk of re-occurrence than patients with cirrhosis. Therefore, in these cases, transplantation is often not necessary and either RBA or resection is preferred [6, 21].

The intermedium stage (B) of HCC, which is characterized by large or multifocal lesions, transarterial chemoembolization (TACE) presents itself as a valid option. In TACE, microparticles are injected in the feeding arteries of the tumour to have a combined chemotherapeutic and embolizing effect that hopefully proves to be fatal for the tumour. TACE is the focus of Section 2.2, along with another transarterial therapy named TARE. However, TACE is the dominant therapy in clinical practice. The reasons for this will be further explored in Section 2.2.3. These transarterial therapies are the main subject of this thesis.

Advanced stage HCC (C) presents itself with extrahepatic spread and vascular invasion and is usually treated with administration of the oral chemotherapeutic drug sorafenib. As of recently, advancements have been made in discovering new systemic therapies that improve on or parallel the efficacy of sorafenib. Lenvatinib was approved by the FDA as front-line therapy alongside sorafenib in 2018. Regorafineb and other systemic drugs been approved as a suitable second-line treatment [7]. It is also not unlikely that TACE is also considered in this scenario, but this must evaluated on a patient-specific basis [6, 21].

For patients with end-stage HCC (D), none of the therapies mentioned above work.

The one-year survival rate is below 10% [6, 21].

With all of this in mind, it is important to re-iterate that early diagnosis is key, and that properly mapping the progression of the disease is also essential to explore the patient's options and increase his/her chances at survival.

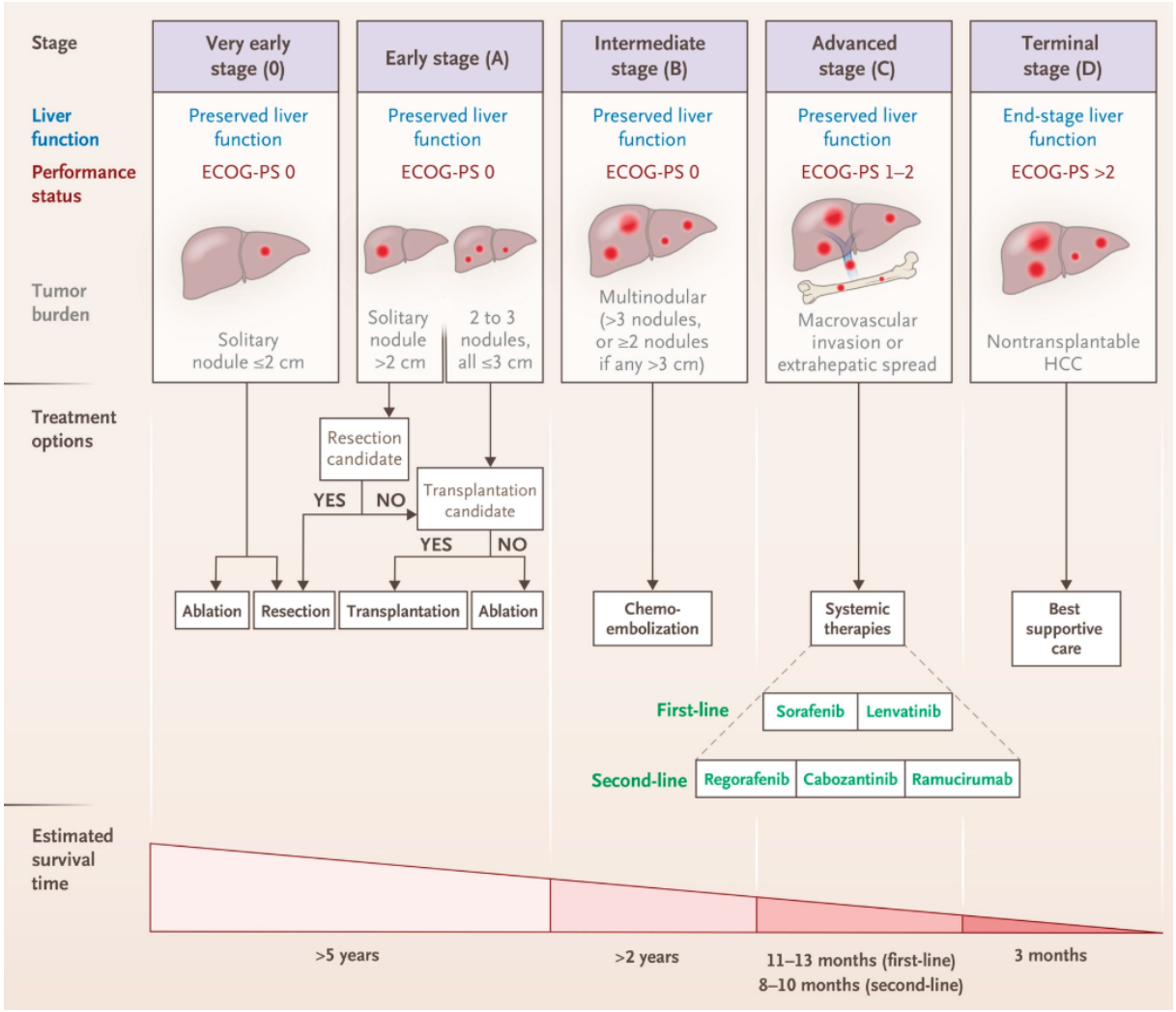

Figure 1.6: BCLC staging system with preferred treatment options [7].

Chapter 2

State of the art

As explained in Section 1.5, there are several treatment options for HCC, depending on the stage of progression of the cancer. The transarterial therapies TACE and TARE are the preferred choice of treatment at the intermedium stage of HCC. These transarterial therapies belong to a particular class of "targeted drug delivery" therapies, which stand in stark contrast with standard chemoembolization techniques because of their target-specificity. In Section 2.1, the concept of targeted drug delivery is explored, along with its general advantages and limitations. In Section 2.2 the procedures of TARE and TACE are explained more in detail. In Section 2.3 the role that numerical modelling plays in the planning of these transarterial therapies is described. Key findings from past studies are listed. Special attention is given to the general conclusions from Koudehi's Master's thesis [26] and Sanchez's Bachelor's thesis [14]. Their findings will lead to the definition of the overall goal of this thesis.

2.1 Targeted drug delivery

The main goal of targeted drug delivery therapy is to maximize the drug dose delivered to the tumour bed. The effect is twofold: on the one hand, increasing the effective dose to the tumour should increase the efficiency of the treatment, and the overall chance of it being successful; on the other hand, this specific targeting should limit the amount of toxicity delivered to healthy tissues. This stands out against unspecific drug delivery, such as conventional systemic chemotherapy, where side-effects occur as a result of an unwanted dose delivery to healthy tissue. The principal difference between these two techniques is depicted in Figure 2.1, where the indicated orange region denotes the region of drug administration and the indicated red region denotes the region of drug delivery. It should be stated that, although Figure 2.1 may indicate otherwise, targeted drug delivery is never 100% effective. There will always be some kind of leak to healthy tissue [8].

Put simply, the goal of targeted drug delivery is to maximize the dose to the target tissue and minimize the leak to healthy tissue.

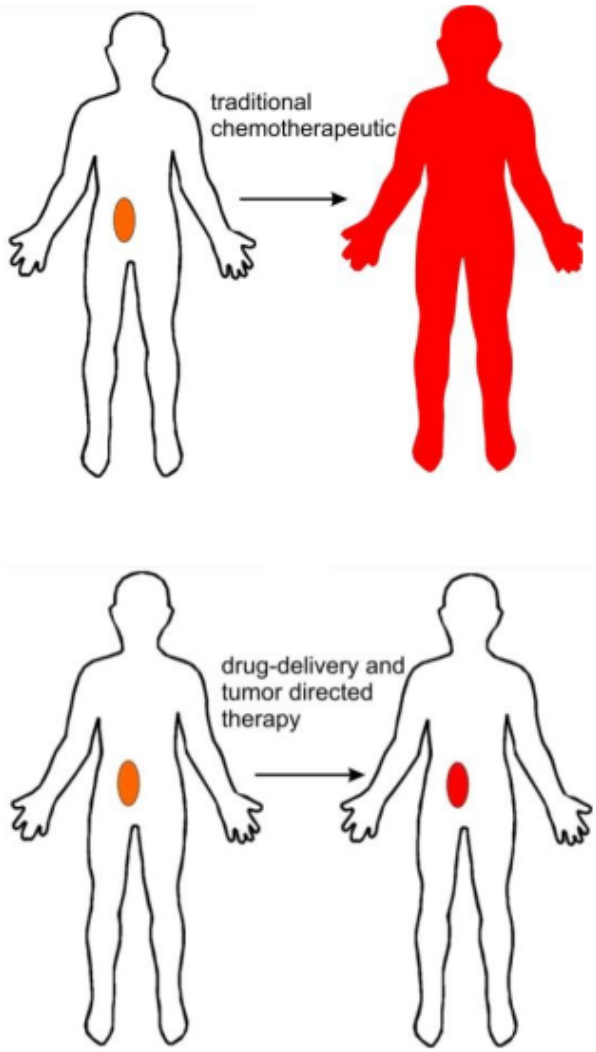

Figure 2.1: Principle of targeted drug delivery [8].

2.1.1 Passive and active targeting

Targeting, in itself, is only a vague concept and deserves further exploration. The distinction can be made between passive and active targeting, which is shown in Figure 2.2.

Passive targeting began, historically, with the discovery of the Enhanced Permeation and Retention (EPR) effect by Hiroshi Maeda in 1984. EPR refers to two important pathophysiological aspects of tumour tissue. Solid tumours are fed by an aberrant leaky neovascalature that increases the vascular permeability. This allows for specifically designed drug particles of certain sizes and weights (generally larger than 40 kDa) to enter more easily into the tumour tissue, whereas, in healthy tissues, these particles would not

be able to exit the much less leaky vessels (hence, enhanced permeation). Similarly, EPR refers to the fact that tumours often lack functioning lymphatic vessels to properly drain these particles from the tissue (hence, enhanced retention). Due to these two properties, drugs accumulate in the cancerous tissue and their average dwell time increases [8, 27].

Even though the discovery of the EPR effect was essential in the development of targeted drug delivery, this concept often goes hand-in-hand with misinterpretation and oversimplification. It should be stressed that the EPR effect is a highly heterogeneous phenomenon, differing wildly between patients and tumours. Some types of tumours, such as Kaposi sarcoma, show this enhanced degree of vascular leakiness, while others do not, or much less so [8, 27].

The difference between concept and reality is shown in panels A and B of Figure 2.2. Conceptually, the leaky vasculature should allow the drug particles to penetrate deeply inside the tumour tissue. But, in practice, the architecture of the tumour mass is still largely heterogeneous and dense, and large regions of the tumour may remain impenetrable throughout the course of therapy [8, 27].

Active targeting, on the other hand, does not only depend on the properties of the tumour tissue. The technique also relies on the qualities of binding ligands bound to the drug particles, which are designed especially to bind to receptors on the tumour surface and drag the particles along with them. These techniques are designed to improve the efficiency of cellular uptake and to allow for selection of certain cell types. However, since drug particles only exit the vasculature and enter the tumour interstitium through passive mechanisms, active targeting does not increase the overall accumulation of drugs inside the tumour nor does it allow for deeper penetration into the tissue. The stark difference between concept and reality of active drug targeting is shown in panels C and D of 2.2. [9]

For both the active and passive targeting techniques to be successful, it is necessary that the particles are able to get in close proximity to the tumour cells, which is not straightforward since the particles' route to the tumour cells is hindered by many barriers. A key barrier - the high density of the tumour mass - is visualized in Figure 2.2 as one of the reasons why both active and passive targeting are often hard to realize in practice. These barriers are the focus of Section 2.1.2.

2.1.2 Barriers and opportunities

In recent years, targeted drug delivery has proven to be somewhat of a double-edged sword. While these therapies offer unique opportunities that could have profound effects on the future of cancer treatment, they are also plagued by complex problems that threaten to overcomplicate their design. This is because the drug's route to the tumour bed is often hindered by a plenitude of barriers.

Each one of these barriers forms a problem on its own, and the solution for one barrier

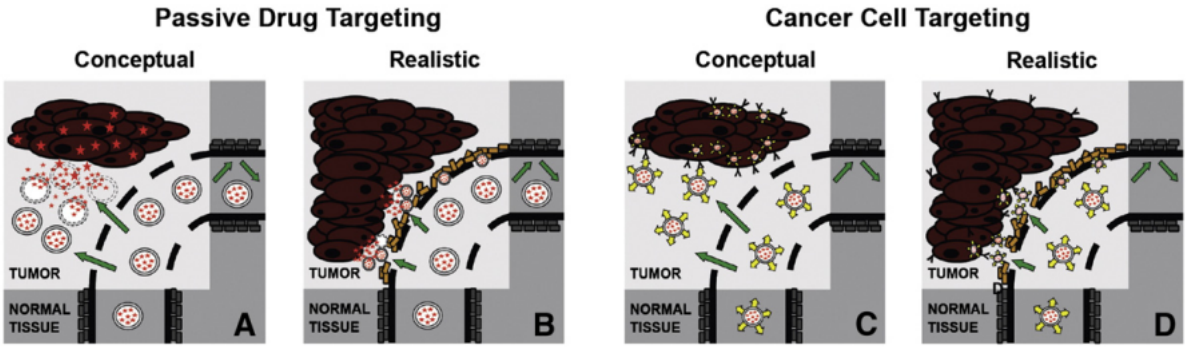

Figure 2.2: Active and passive targeting - expectation versus reality. Although, in theory, the EPR effect allows for larger particles to exit the leaky vasculature (panel A) and active targeting aims to improve cellular uptake (panel C), it is found that the tumour mass is often too dense for particle penetration (panels B and D). [9]

might prove to have a negative effect on another one. For example, nanoparticles are often PEGylated to increase stability inside the bloodstream and avoid premature RES clearance by the liver or the spleen. This process of PEGylation, while effective, renders the particle chemically neutral, thereby greatly decreasing its affinity to bind with the tumour endothelium and cross over to the tumour cells.

Other barriers include the dense, extracellular matrix made up of elastin and collagen surrounding the tumour cells and the high interstitial pressure inside the tumour, which make it particularly hard for the drug particles to penetrate the tumour mass [10, 8].

However, each one of these barriers characterize the environment of the tumour in a very specific way and set it aside from the healthy environment. This means that, in theory, each barrier can become an opportunity for targeting, if used correctly.

For example, the intratumoral environment is characterized by a reduced pH. This is due to the Warburg effect: instead of entering the mitochondria, glucose is diverted to lactate pathways, even in the presence of oxygen, which leads to acidification of tissue. Even though this effect is generally associated with increased tumour growth, this drop of pH differentiates the tumour tissue in such a way that it can be used as a targeting measure. For example, "cluster nanobombs" have been created in a lab environment which disintegrate and release their nanoparticles at the lower intratumoral pH but stay intact at the higher peritumoral pH of the surrounding tissue. By breaking up into smaller particles, it becomes easier for these nanoparticles to penetrate the dense tumour mass. [8, 28].

Even though these barriers offer unique opportunities and solutions, it should be stressed that these barriers are common pitfalls, and that they can overcomplicate the design of the nanoparticles in a way that renders them ineffective.

2.1.3 The road from injection site to target site

In Section 2.1.1, it was noted that active and passive targeting techniques are only effective when drug particles are able to reach the vicinity of the tumour cells. However, the particles' route to these cells is often complicated by the dense extracellular matrix, the high interstitial pressure inside the tumour and other barriers. As described in Section 2.1.2, several complex nanoparticle-designs were invented to deal with these barriers and orient the drug particles across the extracellular matrix. However, this does not tell the complete story of targeted drug delivery. For drug-targeting to work, the delivery of drug particles from the injection site to the target site must be taken into account as well. This was noted by Kleinstreuer, Feng and Childress [10] as a factor that is often underestimated in the development of targeted drug delivery systems.

For the transarterial therapies briefly mentioned in Section 1.5, this problem arises from the fact that the catheters that are used to inject the drug particles often cannot be oriented into the smaller, more tortuous arteries that feed the cancerous tissue. Instead, they must be injected somewhere more upstream and steered in such a way that they reach their target and not deposit in the healthy tissue. This can be done only by varying certain parameters at the injection site that the clinician can control (e.g. injection velocity, injection timing, catheter placement, catheter type, etc.) [10].

Before delving deeper into specifics of this way of direct-drug targeting, first, the general procedures of TARE and TACE will be explained in Section 2.2.

2.2 Transarterial therapies

Transarterial therapies play an important role in the treatment of HCC. The main goal of this type of treatment is to cut off the blood supply of the tumour tissue by local administration of embolizing particles. These techniques benefit from the fact that healthy liver tissue is supplied by both the portal veins as the hepatic artery, whereas tumour tissue in the liver is mainly fed by arterial blood only. Obstruction of these feeding arteries will lead to starvation and tumour cell death. Aside from embolization, the administered drugs can have secondary malignant effects. Here, the difference is drawn by a chemotherapeutic effect (chemoembolization) and radiation effects (radioembolization) [29, 30, 31, 32].

2.2.1 Chemoembolization (TACE)

The idea behind chemoembolization is to occlude the feeding arteries of the tumour with an embolizing agent and inject a chemotherapeutic drug simultaneously. This process is visualized in Figure 2.3. The vascular occlusion should increase the dwell time and concentration of the chemotherapeutic drug in the embolized tumour tissue [29, 30].

There are two distinct ways to deliver these two particles. Either the drug (e.g. doxorubicin) and the embolizing agent (e.g. polyvinyl alcohol particles) are administered separately, or these two agents are combined in a particle that holds the two together. This latter method is known as DEBDOX, in which DEB stands for drug-eluting beads and DOX refers to doxorubicin. These drug-eluting beads consist of polymeric microspheres in which a solution of doxorubicin is injected. As the beads occlude the feeding arteries of the tumour, doxorubicin is slowly released and diffuses radially in the embolized tissue with its concentration gradually decreasing with distance [29, 30]. Comparison between these two methods shows similar to better results for DEBDOX than for conventional TACE [33].

The main idea here is that tumour necrosis occurs because of the combined pharmacological effect of the two agents: both the chemotherapeutic drug as the embolizing agent add to the overall response in such a way that they are complementary to each other [29].

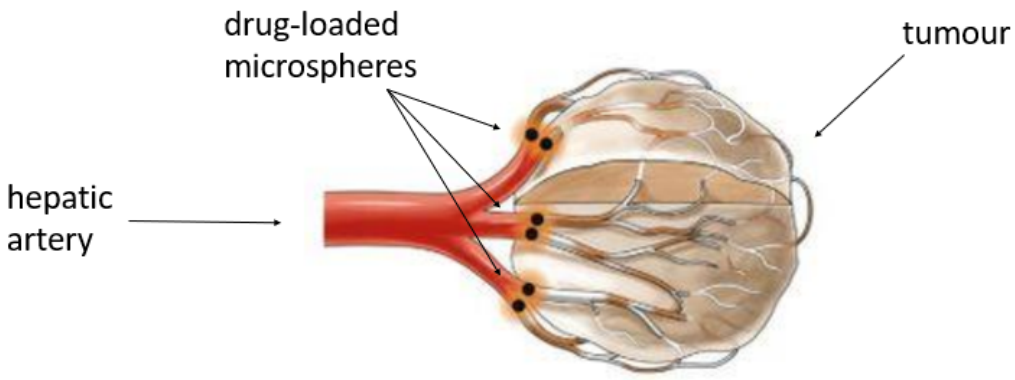

Figure 2.3: Principle of chemoembolization. The microspheres occlude the feeding arteries of the tumour and release a chemotherapeutic drug for a combined effect. Adapted from [10].

2.2.2 Radioembolization (TARE)

Radioembolization is currently a less standard clinical procedure than chemoembolization, but it is steadily gaining popularity as an alternative to TACE. [31, 32] The reasons for this will be outlined in Section 2.2.3. As for the principle of TARE, it is both deceptively similar and dissimilar to TACE. The two processes are alike in the way that they both require catheterization and injection of particles in the feeding arteries of the tumour. However, they differ in the way the tumour tissue is damaged.

In TACE, as mentioned above, the damaging effect is actually the combination of an embolic and a chemotherapeutic effect. In TARE, this embolic effect is much less important. The main pathway by which the cancerous tissue is fatally damaged, is by a

very local delivery of radiation. Yttrium-90 (Y-90), embedded in small microspheres, is injected in the hepatic arteries and emits a high-intensity but short-lived beta-radiation. As is known, these beta-particles cause damage by ionizing water molecules and creating free radicals that destroy DNA molecules. For this damage to be maximal, blood flow and adequate perfusion of this area is desired, which is a huge difference with TACE, where perfusion is halted and ischemia occurs. [32]

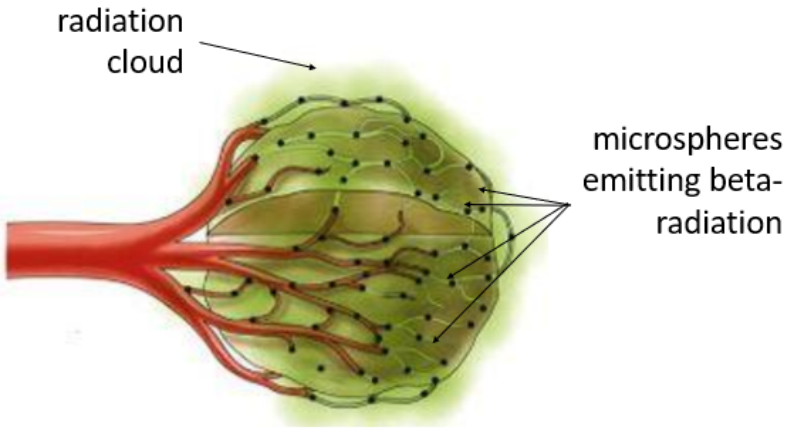

Figure 2.4: Principle of radioembolization. The microspheres emit local high-intensity beta radiation which destroys the nearby tumour tissue. Adapted from [10]

Currently, there are two types of products on the market: the TeraSphere and the SIR-Sphere. These microspheres differ in composition: the TeraSphere is made of glass, while the SIR-Sphere is made of resin. There is still ongoing discussion on which one yields the better results in clinical practice. In either case, both the TeraSphere and the SIR-Sphere contain Y-90. The amount of healthy tissue that is exposed to this kind of radiation should remain limited. [31]

The procedure of TARE is relatively complicated, especially when compared to the more straightforward TACE. This is because TARE requires extra cautionary steps. Due to the small size of the microspheres, the particles may spread outside the liver to the lung if an arteriovenous shunt is present. To avoid this unwanted effect, a pre-treatment scan must be performed to determine lung shunt fraction (which must be below 20 percent at all times). This screening is done by labelling macro-aggregated albumin (MAA) particles with Tc-99m and injecting them in the hepatic arterial vessel. Shunt fraction is then determined by measuring the lung dose. Only if the patient passes this first test, it can be assured that radiation to the lungs will be minimal, and treatment can proceed. If not, then alternative treatment options such as TACE must be explored.

Furthermore, a pre-treatment angiography must be performed to assess the patient-specific vasculature of the tumour. Locating and identifying the feeding arteries of the

tumour in this step is crucial: if one of the feeding arteries is missed, this artery will not be targeted and the procedure will be incomplete. In some cases vessels like the gastroduodenal artery are pre-emptively embolized to prevent flow of microspheres (and, by extent, radiation) in the gastrointestinal tract. [31, 11]

The third step of treatment is to calculate the amount of activity that must be administered to reach the desired dose in the tumour, all while taking into account that the dose limit for healthy liver tissue is about 40 to 50 Gy (depending on the circumstances). The preferred dosimetric approach is patient-specific and makes use of information obtained from SPECT-CT fusion scans. An example of such an image is given in Figure 2.5. The healthy and cancerous liver tissue, as well as the lungs, are divided up in compartments. The masses of each compartment are calculated using CT scans, and the fractional uptake of activity of each compartment is determined using the Tc-99m SPECT scans from before. It should be noted here that the Tc-99m-MAA particles have totally different properties than the Y-90 microspheres (i.e. the two particles have different sizes and different specific gravities), which means that distribution of activity obtained from the earlier scans are only approximations of the reality [34]. If such personalized approach is not available, activity can also be calculated using generalized, empirical formulas as prescribed by the manufacturers, but this approach is considerably less accurate [32, 11].

As of recently, a third particle type, Holmium-166 (Ho-166), has been under study. Ho-166 has the added advantage over the standard particles used for TARE that it emits both high-energy beta particles and low-energy gamma photons. In practice, this means that these Ho-166 particles can be used for both the pre-treatment scans and the actual treatment, whereas, for Y-90 particles, different particles with different properties (namely, the Tc-99m-MAA particles) had to be used for the pre-treatment scans. The Ho-166 particles are even slightly paramagnetic, which makes them visible on MRI scans. If the discrepancy between the Y-90 and the pre-treatment Tc-99m-MAA proves too large in certain cases, then the Ho-166 particles can offer an interesting new route [35].

In general, due to the small size of the microspheres and the radiation limits in healthy tissue, the TARE procedure is relatively complicated. The overall success of the treatment depends on the correct execution and integration of all of these steps.

2.2.3 Comparison between TACE and TARE

At this point, it should be noted that it is currently unknown which of the two procedures outperforms the other when it comes to efficacy and safety. This is simply because, as to date, there has not been a large-scale, randomized study to evaluate long-term parameters such as overall survival rate and quality of life. However, several smaller-scale studies have been performed. These suggest that postembolization syndrome is less severe in TARE than in TACE, because less tissue is embolized. Hospitalization time is also usually shorter

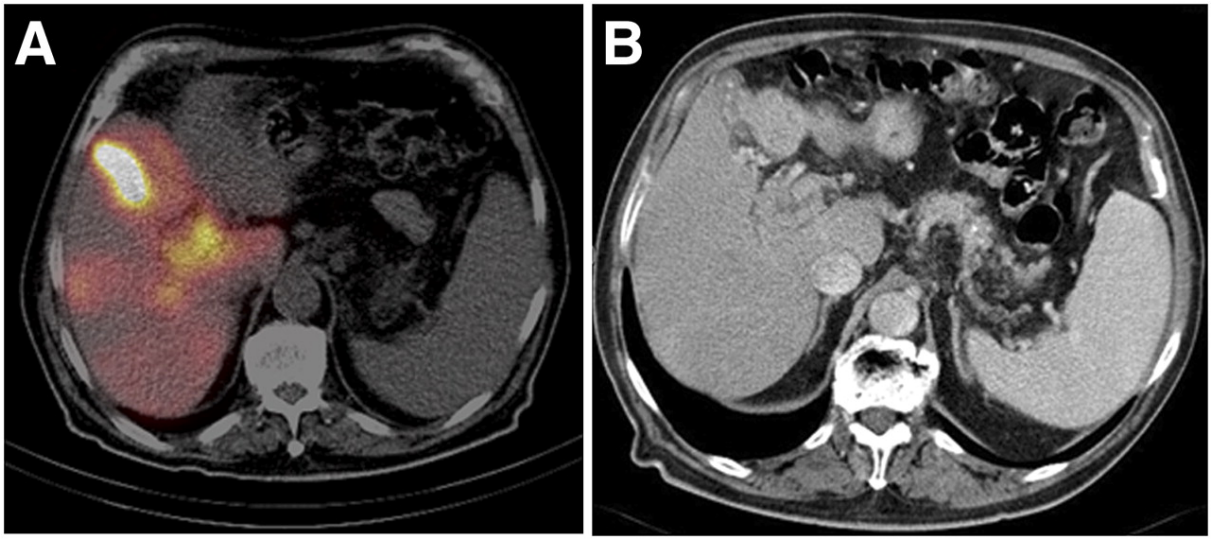

Figure 2.5: SPECT/CT fusion scan showing tumour mass in portal vein [11].

with TARE [32, 36]. An important rationale behind choosing one method over the other is solely based on the technical complexities of the procedures. TARE requires intricate dosimetric calculations and pre-treatment scans, while TACE is a much more standard and less costly procedure. [31, 36]

2.2.4 The importance of personalized medicine

For transarterial therapies, which are the main focus of this thesis, one of the key barriers to overcome is the lack of homogeneity between and within tumours. It is of noteworthy importance to stress the difference between inter-tumour heterogeneity (the differentiation of tumours between multiple patients) and intra-tumour heterogeneity (the differentiation between sub-clones of a tumour in one patient). The difference between these two principles is depicted in Figure 2.6. This heterogeneity is the main cause for a lack of standardized therapy for both TACE and TARE procedures and will be an essential factor to consider later on, when discussing the exact methodology of these procedures in Section 2.4 [12].

2.3 The added value of computer modelling in drug-targeting

2.3.1 Principle

As explained in Section 2.2, catheterization of the hepatic arteries is an essential step in the TACE and TARE procedures. The goal is to guide the damaging particles to the tumour tissue. The steering of these particles from an upstream injection point to the

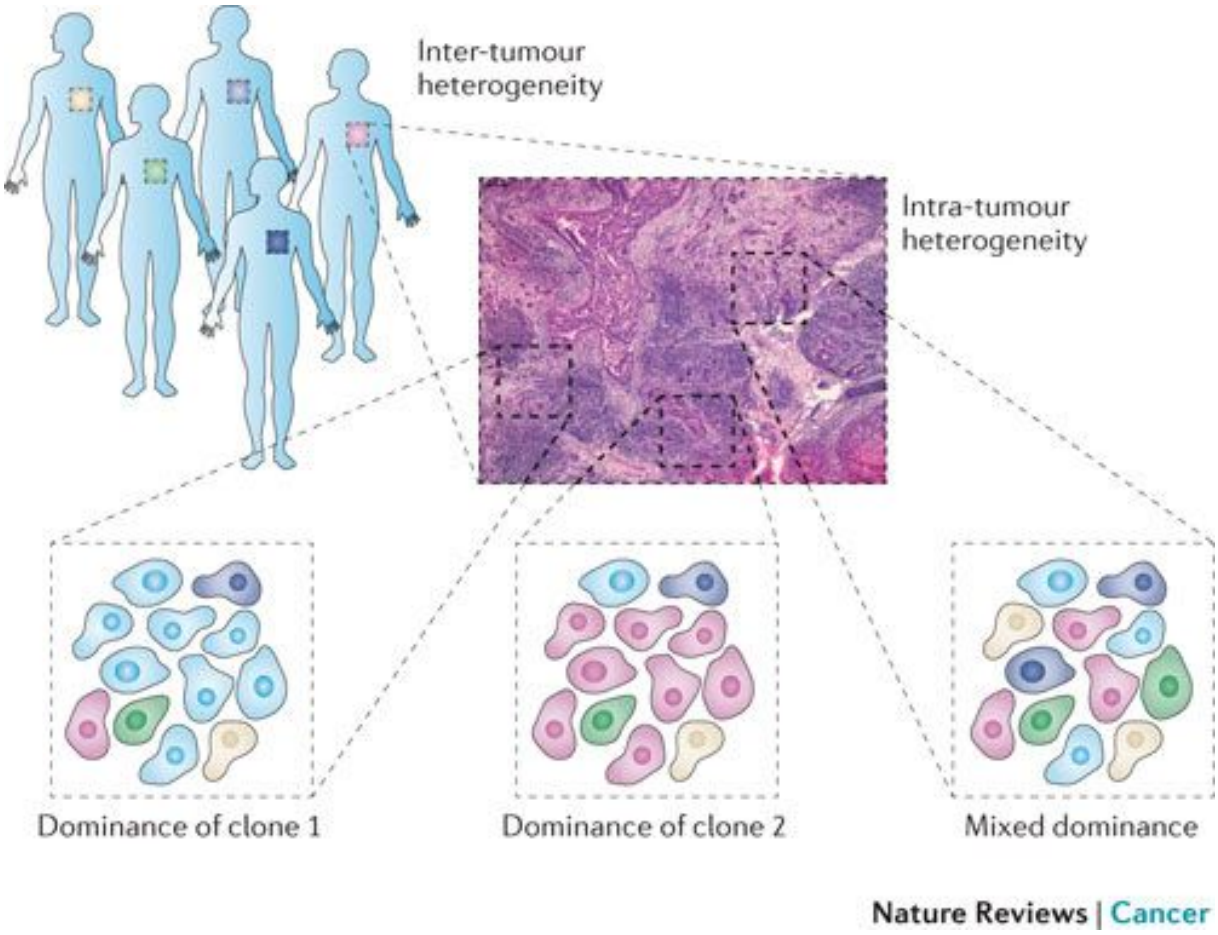

Figure 2.6: Inter-tumour and intra-tumour heterogeneity [12].

downstream target site is achieved by exploiting the blood flow and by determining the optimal location of the catheter inside the blood vessel lumen. This is done through numerical modelling. Using computational fluid dynamics (CFD), the trajectories of the particles inside a representative model of the patient's arterial network are simulated. By tracking back these trajectories to the plane where they were injected, a particle release map (PRM) is generated. This PRM, as shown in Figure 2.7, visualizes at what point in the injection plane a particle needs to be injected in order to end up in a specific exit branch of the vasculature. Suppose, in Figure 2.7, that exit branch 3 is located near the tumour, then the particles must be injected at the outer periphery of the vessel (pink zone). Likewise, if images show that exit branch 5 is connected to the tumour, then the particles must be injected more centrally (yellow zone). This technique lends to extend itself to even more parameters that are variable in clinical procedures, such as injection velocity, injection timing, catheter type, catheter tip orientation, particle type, etc. By varying these parameters over multiple simulations, the simulation that gives the PRM with the largest injection area for the tumour tissue can be determined as the most optimal one. Once a sufficient amount of CFD simulations have been run, the ideal set of conditions that maximize the particle delivery at the target site can be found.

By using CFD to model the influence of patient-specific geometries, flow patterns and parameters such as catheter position on particle behaviour inside the bloodstream, steps can be taken towards overcoming the barrier of inter-tumour and intra-tumour heterogeneity that was mentioned in Section 2.2.4 [10].

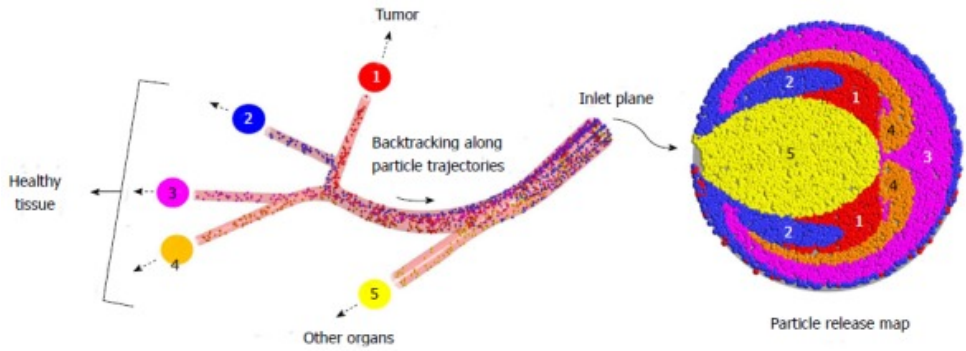

Figure 2.7: Particle release map of a planar idealised hepatic arterial geometry [10].

2.3.2 Parameters of interest

In Section 2.3.1, several clinically variable parameters were mentioned that could have an influence on particle distribution in the truncated hepatic arterial tree. In the best-case scenario, the clinician can use one or multiple of these parameters to steer the particles towards specific exit branches. Below, the following parameters are discussed: particle size and quantity, particle density, catheter tip position and injection velocity. It should be noted that the full list of possible parameters is exhaustive and extends beyond what is discussed here.

To this end, several studies from literature are discussed. Special attention is paid to Koudehi's Master's thesis [26] and Sánchez's Bachelor's thesis [14]. In her Master's thesis, Koudehi performed a parametric study in a healthy liver. She also performed a validation study to check if the PRM generated in the baseline situation could be validated by a experimental in vitro set-up with a 3D printed model of the liver vasculature. In her Bachelor's thesis, Sánchez performed a similar parametric study in a liver from a radioembolization responder patient. The emphasis is put explicitly on their key insights as they laid the foundations for this research.

Catheter tip position

Aramburu et al [13] shown that even a 5-mm shift between catheter tip positions could result in a significant difference in downstream particle distribution. This is visualized in Figure 2.8. On the left side (Simulation 8), it can be seen that the injected particles only travel down the right hepatic artery. On the right side (Simulation 9), the catheter tip is placed near the same bifurcation with a shift of 5 mm. In this case, a significant fraction

of the particles also travel down the left hepatic artery. The dependency on position is high because the haemodynamic patterns near bifurcations are largely variable, even for such small shifts. Aramburu et al also note that the effect of catheter tip positions most likely decreases when particles are injected further away from bifurcations, because the variations in the haemodynamic patterns are much smaller in straight vessel segments.

In their respective works, both Koudehi [26] and Sánchez [14] remarked that the PRMs looked distinctly different when particles were injected near a bifurcation than when they were injected further away from it. Sánchez also noted that the PRMs in her study appear more dissimilar to each other than the ones in Koudehi's Master's thesis. However, the results are highly patient-specific and are, by extent, hard to generalise.

Particle properties

According to Aramburu et al [37], particle density is not a critical parameter and the influences of particle size and quantity are also minimal. However, it was noted that these results depend highly on the specific arterial geometries and may have noticeably different results in other studies.

In her Bachelor's thesis, Sánchez [14] noted that the largest influence with regards to the different types of particles modelled in her study was found in the numbers of particles exiting the domains. As can be seen in Figure 2.9, the particles that exit in the largest fraction are the Tc-99m particles, which also have the lowest density (1100 kg/m^3, compared to the density of 1600 kg/m^3 for the SIR-Spheres). The particles that exit the lowest fraction are the Thera-Spheres, which are also the densest (3290 kg/m^3). These conclusions match the conclusions drawn by Koudehi in [26], where it was shown that the bigger and denser particles tend more to remain inside the domain, as their size and density notably makes transport through the arterial system more difficult. Sánchez [14] remarked that this also corresponds to a study conducted by Jernigan et al [38], where the penetration depths of glass and resin microspheres were also investigated. There, it was reported that the average penetration depths of resin microspheres were larger than the average penetration depths of the denser glass microspheres.

Thus, these studies seem to partly disagree with the conclusions drawn in the study by Aramburu et al, arguing that particle density does play a critical role in particle distribution.

Injection velocity

Kleinstreuer et al [15] reasoned that, as the injection velocity of the particles increased, it would become harder to steer them toward a specific exit branch. This is shown in the lower panels of Figure 2.10. With speeds higher than the blood flow, the particles gain the ability to cross streamlines and exit non-target branches. At ten times the speed of the surrounding blood flow, particle inertia effects dominate, and the momentum of the

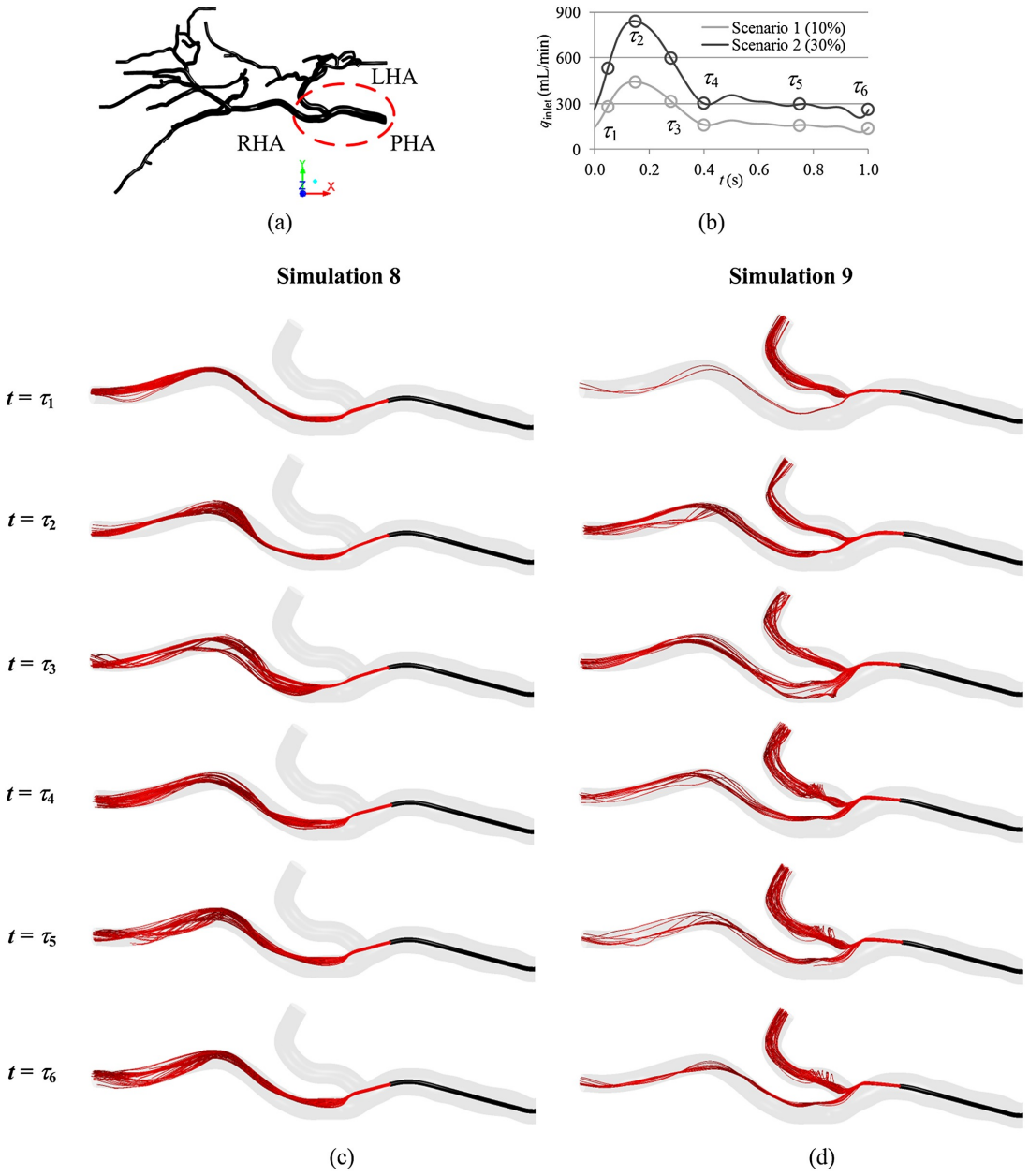

Figure 2.8: Influence of catheter tip position on particle flow. A 5-mm shift of catheter tip near a bifurcation greatly impacts downstream particle distribution [13].

incoming flow of particles becomes too high to dissipate, which makes targeting much more difficult.

In her Master's thesis, Koudehi [26] concluded that varying injection velocity did not have an substantial influence on the particle distribution and that the other varied parameters in her study (particle density, particle size and location of the injection plane) were more influential. However, the range to which Koudehi increased the injection velocity was not nearly as large as the range at which Kleinstreuer et al [15] reported a significant impact of injection velocity, which most likely explains the discordance in conclusions. Similarly, Sánchez [14] concluded that lowering the injection velocity by 20% did not have

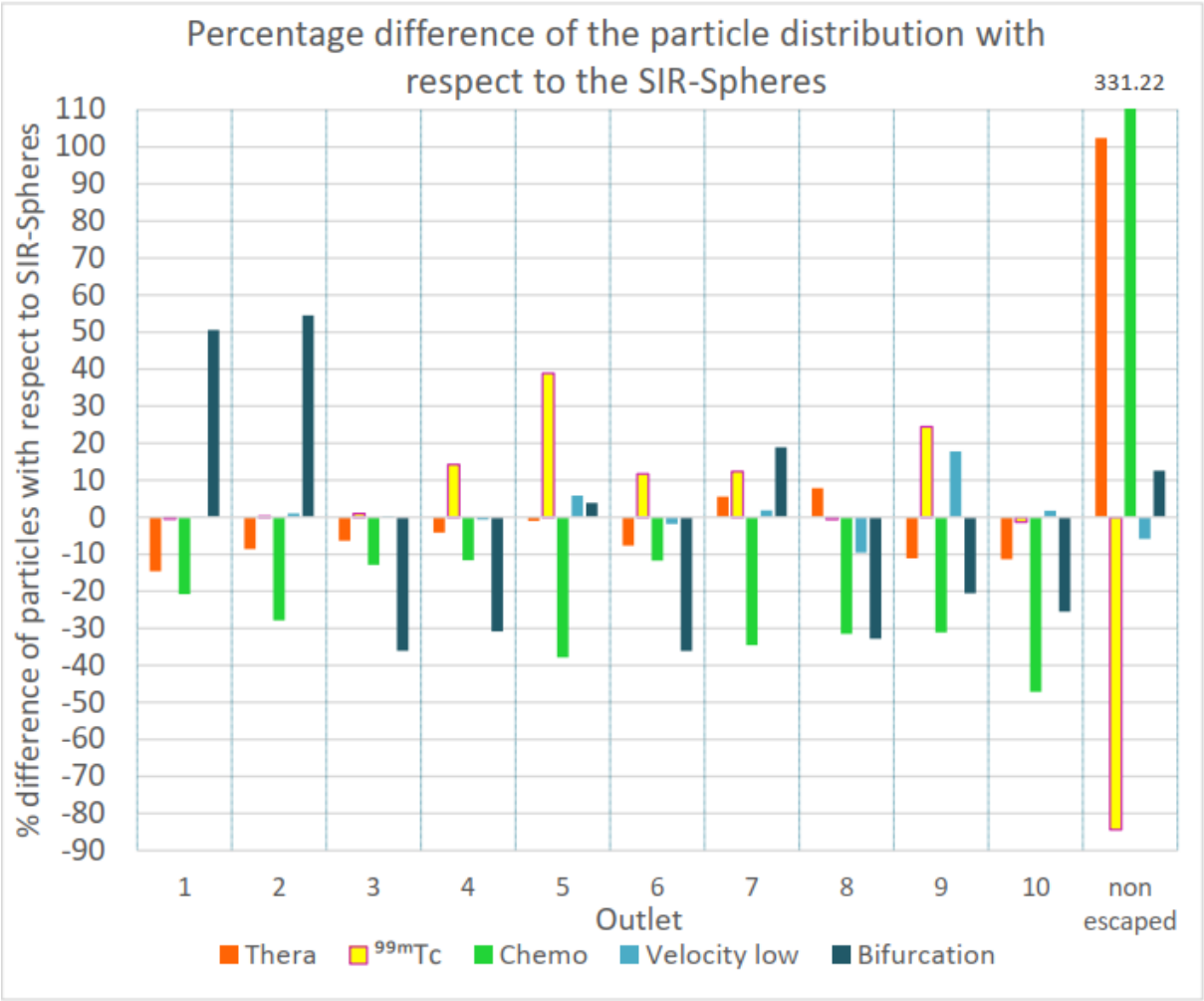

Figure 2.9: Percentage variation of the particles exiting through each outlet with respect to the SIR-Spheres. As can be seen, the largest differences are found in the amount of the particles that exit through the different outlets. The less dense Tc-99m particles exit in the largest numbers, while the much denser TheraSpheres and HepaSpheres exit the least [14].

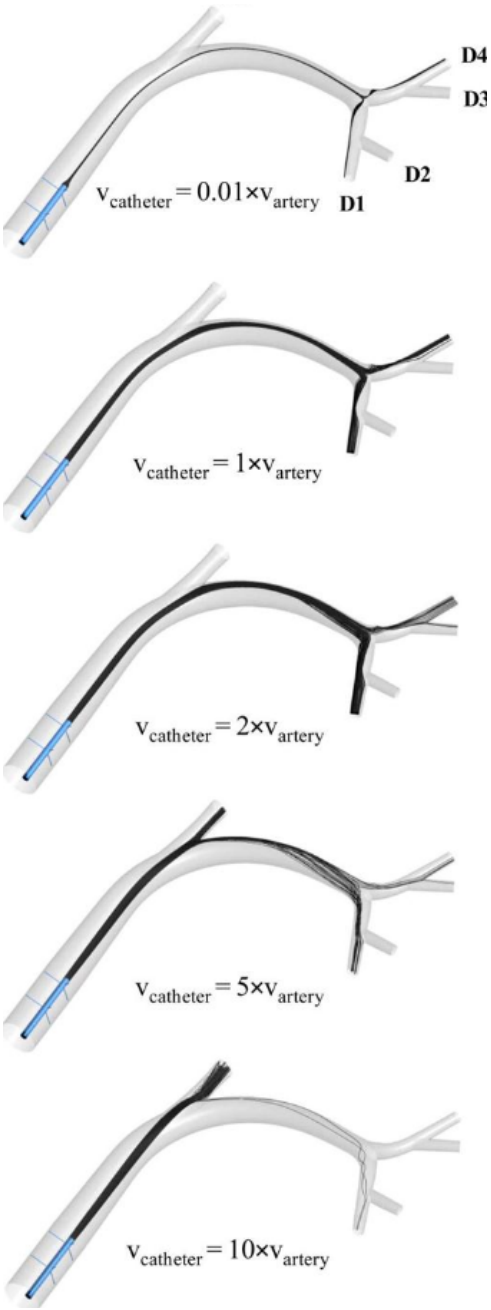

Figure 2.10: Influence of injection velocity on particle distribution. As injection velocity becomes significantly larger than the velocity of blood, particle inertia effects dominate and it becomes harder to steer these particles towards a specific exit branch [15].

a significant influence of particle distribution

In short, it can be stated that injection velocity (or more specifically, the ratio of catheter flow to surrounding blood flow) can have a definite impact on particle distribution, but only when it is increased significantly.

2.3.3 Computational complexities

For computer simulations the desire to create models that are both close to reality and computationally time-manageable is often hard to balance. Therefore, several assumptions and simplifications are made to simplify the existing reality in a way that not too much of the results' eventual accuracy is sacrificed. As CFD simulations play an essential role in the evaluation of clinical parameters and will need to be performed on a clinical patient-to-patient basis, it is of crucial importance that they are computationally manageable. In the sections below, three computational complexities are considered: arterial wall deformation, the degree of coupling between the discrete particles and the fluid phase and cancer burden. Cancer burden will be deemed an important factor that will feature throughout the remainder of this research.

Fluid-structure interaction

When generating PRMs at multiple time points, it should be considered that the arterial wall, which is put under significant stresses, deforms during the cardiac cycle. This means that the diameters of the arteries change and, with them, the size of the PRMs. Childress and Kleinstreuer [16] have modelled such time-varying, flexible PRMs for a representative hepatic arterial geometry and compared these to the PRMs generated in the case of rigid arterial walls. In Figure 2.11, the representative geometry of the hepatic arterial tree is visualized in panel (a). In panel (b) of Figure 2.11, the evolution of the arterial wall diameter during the cardiac cycle is visualized for three models: a flexible model, a rigid model using a time-averaged diameter and a rigid model using the diameter in diastole. It was found that the ideal targeting interval takes place during the diastolic phase of the pulse, because the changes in the deforming geometry are significantly lower than during systole. In this case, the rigid-diastolic PRM could be used because it closely resembles the geometry in diastole.

In this thesis, the arterial walls were assumed to be rigid. Including fluid-structure interactions would make this model increasingly more complex but this could be a point of interest in future research.

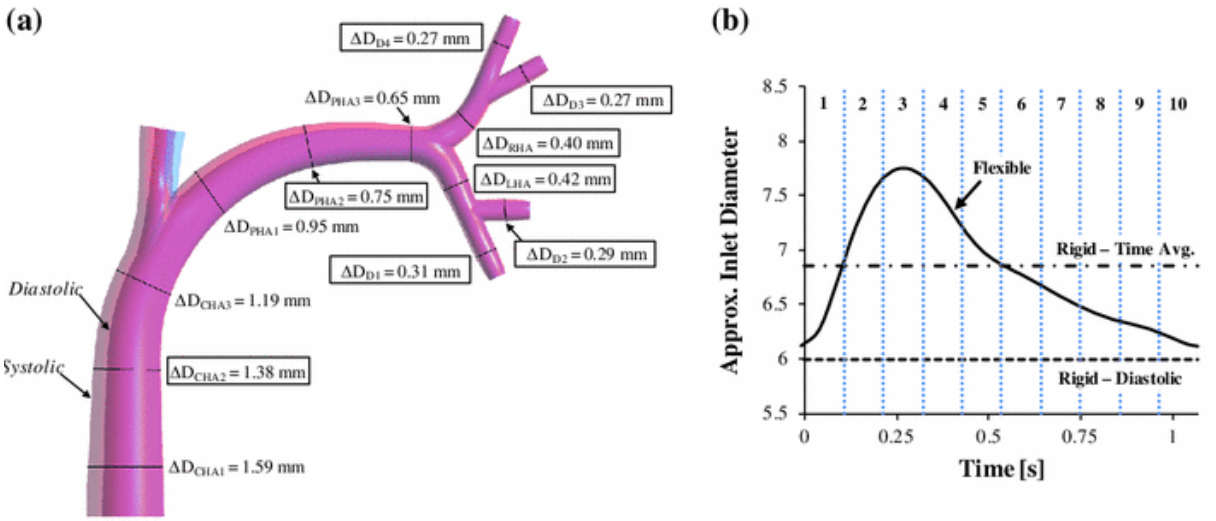

Figure 2.11: Evolution of diameter of arterial wall throughout cardiac cycle. Childress and Kleinstreuer [16] concluded the rigid-diastolic PRM is best used during the diastolic phase of the cardiac cycle for targeting.

One-way versus two-way coupling

As the discrete particles traverse the fluid continuum, they may exchange heat, mass and momentum with the fluid phase. It is important to consider the impact the two phases exert on each other, because this will determine the degree of coupling between the continuous and discrete phases and this will, in turn, determine the accuracy of the results and the computational time needed to obtain them. In one-way coupling, the fluid flow is calculated first and then the particle trajectories are generated afterwards. In two-way coupling, the situation is more complicated as the impact of the discrete phase on the continuous phase is also taken into account. The continuous and discrete phase calculations are alternatively solved until the solutions in both phases have stopped changing [39].

Koudehi used one-way coupling in her Master's thesis [26], stating that this was a good approximation since the particle solution was dilute. Aramburu et al [37] have reported that, even though when two-way coupling is chosen, the particles do not significantly influence the blood flow. Due to this conclusion, Sánchez opted to use one-way coupling in her Bachelor's thesis [14]. The same assumptions was made for this thesis.

Cancer burden

Cancer burden, which is determined by the precise type and volume of the tumour, plays an important role when it comes to end-distribution of the particles, because the higher the burden, the more blood will flow to the tumour and the higher the "dragging force" of the blood will become. Aramburu et al [13] have shown that with a higher cancer burden, the effect of catheter-tip position lessens, because the power of blood flow to carry the particles to the tumour increases significantly. In Figure 2.12, the panels on the right

side (Scenario 2) represent a situation in which the cancer burden is considerably higher than in the panels on the left side (Scenario 1). For each segment (denoted S1 to S8), the last three bars compare the particle distribution (in %) for different particle properties and different catheter positions with each other. Here, it can be seen that the maximal differences in particle distribution for the different cases in Scenario 1 are much higher than for the different cases in Scenario 2, which is reportedly due to the higher cancer burden in the latter scenario [13].

Both in Koudehi's Master's thesis [26] as Sánchez's Bachelor's thesis [14], cancer burden was not considered to have an impact on the outflow characteristics of the model, which were described by Murray's Law in Equation 4.10. However, in this thesis, an alternate boundary condition, as proposed by Aramburu et al [2], was considered that does takes the effect of cancer burden into account.

2.4 Standardized workflow

What the description of these transarterial therapies lacks up until this point, is a form of standardization. Therefore, a workflow in three distinct steps was proposed by Kleinsteuer, Feng and Childress [10]. This workflow, named the Computational Medical Management Program (CMMP), must be followed for each patient undergoing transarterial therapies . A schematic outline of this work flow is shown in Figure 2.13. Below, the three distinct steps of the CMMP are shortly discussed. The general workflow of this thesis will partly mimic the CMMP.

2.4.1 Patient evaluation

The first step of the CMMP includes classifying the tumour and choosing the best treatment option. This was already discussed in Section 1.5. For TARE specifically, it was stressed in Section 2.2.2 that pre-treatment tests should establish that lung shunt fraction is below 20% at all times and that amount of activity in the healthy tissue should remain below the described dose limit, otherwise the procedure is not deemed safe. Since these estimations are usually made by injecting Tc-99m-labelled MAA-particles and evaluating resulting SPECT images, it is obvious that medical images play an important role in this review. If either TARE or TACE are viewed the ideal treatment option, then the procedure should proceed as described below [10].

2.4.2 Computer modelling

In this step, anatomical and metabolic information is extracted from medical images to segment the tumour and its feeding arteries. By using computer software, a 3D geometry of the arterial network of the tumour is created and meshed. Next, a model is set up by

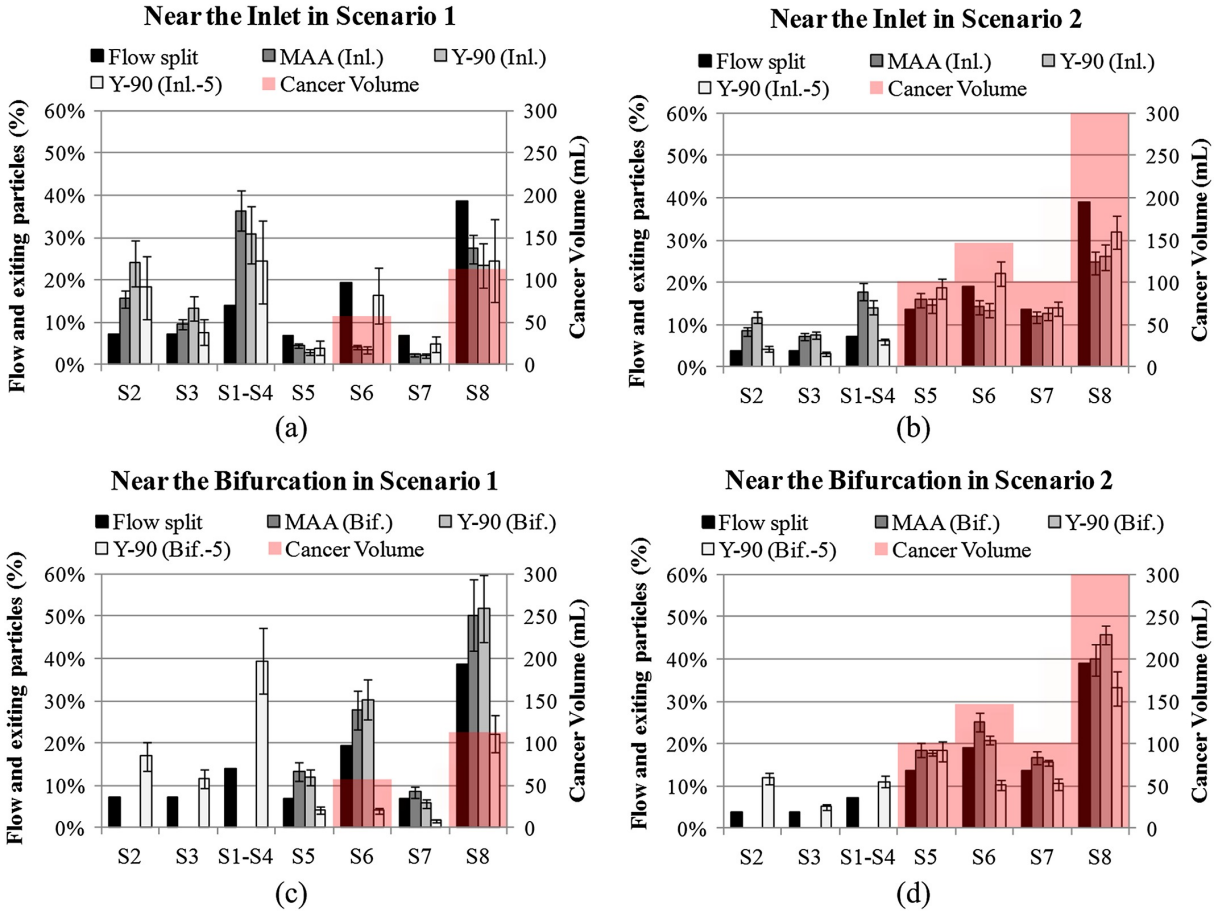

Figure 2.12: Influence of injection characteristics on segmental distribution. The second and third bars compare the distribution of MAA-particles used for scout scans to the distribution of Y-90 particles used for actual therapy. The fourth bar compares injection with a 5 mm-shift in catheter position as opposed to the situation in the third bar. The top panels compare injection near the artery inlet to injection near a bifurcation in the bottom panels. The panels on the right side compare a situation in which the cancer burden is considerably higher than the situation of the panels on the left side [13]

.

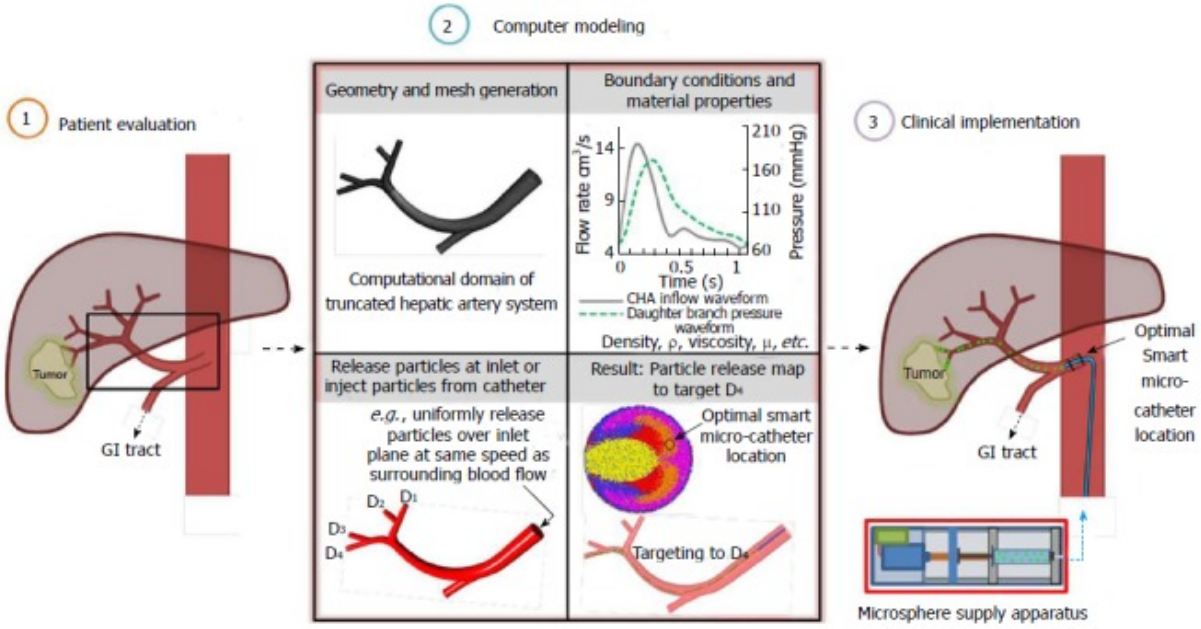

Figure 2.13: Treatment planning strategy.

specifying material conditions and the appropriate boundary conditions for the inlet and the outlets of the computational domain. Then, numerous simulations of downstream segment-to-segment particle distribution are run, and the PRMs at the injection plane are generated. These simulations can vary in all of the parameters discussed in Section 2.3.2 and more. From the result of these simulations, the parameters that give the most optimal downstream particle distribution (i.e. the most particles at the tumour sites) can be identified. The ideal placement of the catheter at the injection plane can also be determined [10].

2.4.3 Clinical implementation

Once the generated PRMs have supplied the necessary information, the clinician can proceed with the actual treatment. In order to target specific branches, the clinician must be able to inject the particles at a specific point with a specific velocity at the injection plane. To this end, the Smart Micro-Catheter (SMC) was developed.

Catheter design: Smart Micro-Catheter

The Smart Micro-Catheter (SMC) was designed to ensure stable positioning of the catheter tip inside the vessel lumen on the ideal radial location. The ultimate goal is to deliver the damaging particles in the feeding arteries of the cancerous tissue by injecting them in the injection area as predicted by the PRMs. The schematic design of the SMC is visualized in Figure 2.14. Here, it can be seen that the catheter is connected to an automated particle syringe or medicine supply apparatus (MSA) that pumps the particles into the catheter at the right speed and interval as predicted by CFD simulations. This MSA resides ex-

ternally, while the SMC is positioned inside the vessel lumen and stabilized using struts. The main components of the MSA are a piston-displacement motor, a syringe containing the microsphere solution and tubing connecting the MSA with the SMC [10, 14, 40].

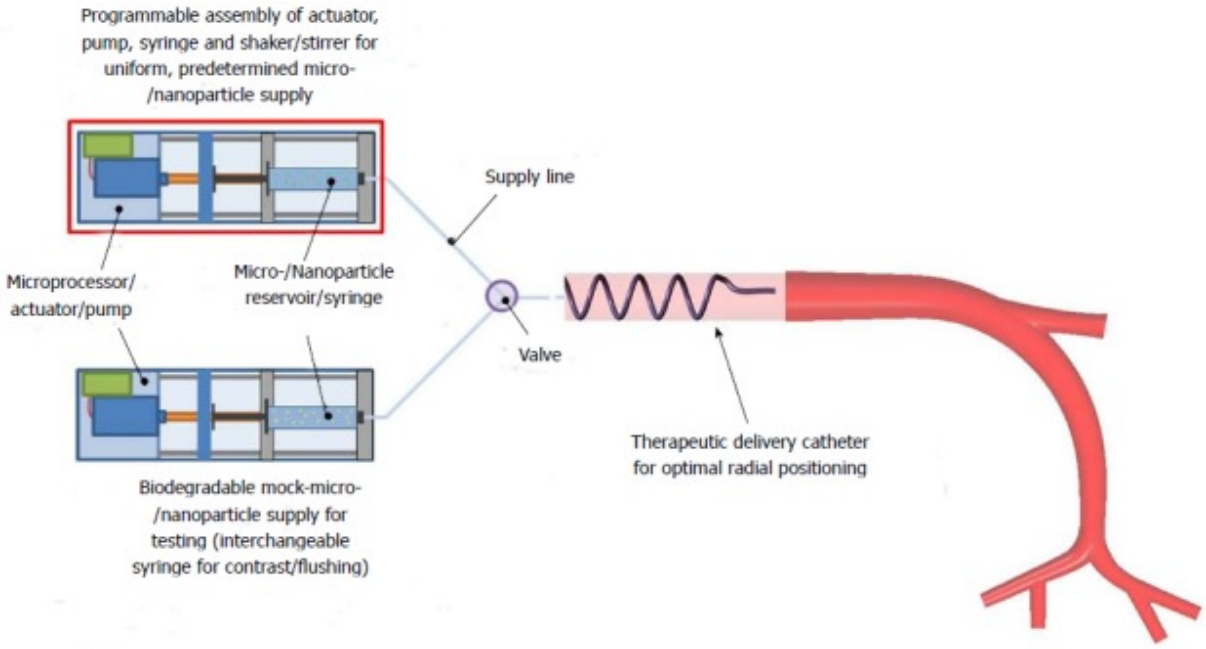

Figure 2.14: Combination of MSCA and SMC to ensure correct catheter positioning and particle delivery at the right speed and interval [10].

2.5 Goal

As was already stated in Section 2.3.3, both Koudehi [26] and Sánchez [14] have made significant contributions to this field of study. This thesis will aim to build upon their accomplishments.

In her Bachelor's thesis, Sánchez [14] suggested using an alternate boundary condition to Murray's law. In Murray's law, the flow distribution throughout the arterial network is calculated based on geometrical properties of the network. It is not taken into account that cancer tissue has different metabolic demands than non-cancerous tissue. The alternate outlet boundary condition, first described by Aramburu et al [2], hypothesizes that the arterial perfusion of a cancerous tissue is over four times as high as the arterial perfusion of healthy tissue. This could have a severe impact on flow distribution throughout the arterial network. As Koudehi [26] and Sánchez [14] have already concluded that particle distribution at the outlets tends to match the overall flow distribution, the impact of the volumes and distribution of tumour nodules through the liver - in short, the *cancer burden* - could have a severe impact on particle distribution. To investigate the impact of cancer burden on the eventual particle distribution, eleven different hypothetical cancer scenarios are developed and the PRMs are generated for each of these scenarios. These

PRMs are helpful visual tools that will help compare the different cancer scenarios with each other and with the PRM generated by using Murray's law as a boundary condition.

In her Master's thesis, Koudehi [26] worked with a healthy liver. However, the vascular architecture of a cirrhotic liver and a healthy differ distinctly from each other. It was already reported in Section 2.3.2 that all the results of the parametric study are highly patient-specific. Therefore, the impact of using a cirrhotic geometry that is typically more tortuous than a non-cirrhotic one could be significant. This is particularly interesting in the case of patients with HCC since HCC regularly develops from cirrhosis, as mentioned back in Sections 1.1 and 1.2. With this in mind, the patient-specific geometry of a cirrhotic liver is used in this research.

In short, the goal of this thesis is to investigate the impact of cancer burden on the particle distribution in a patient-specific cirrhotic liver.

Part II

Computer Modelling

Chapter 3

Geometry and Mesh Generation

As described in Section 2.4, the generation of a computational domain of the truncated hepatic artery system is a crucial step in the planning of transarterial therapies. In this thesis, the arterial network of a patient with cirrhosis was used, as cirrhosis often plays an important role in the development of HCC. Since cirrhosis affects the hepatic architecture, the effects of the geometry on the eventual particle distribution can be significant.

In Section 3.1, it is described how a 3D model of the arterial network of a cirrhotic liver was obtained. In Sections 3.2 and 3.3, the steps that were taken to create a surface and a volume mesh of this model are outlined. The results of the mesh sensitivity analysis that were evaluated to determine the optimal mesh density are also described. Finally, this volume mesh was imported into ANSYS Fluent (Ansys, Canonsburg, PA, USA), which will be the focus of Chapter 4.

3.1 Data acquisition

According to Peeters et al [41] cirrhosis is characterized by diffuse fibrosis, the conversion of normal liver architecture into structurally abnormal regenerative nodules and the formation of an abundant vascular network. This alteration of the hepatic architecture has a large impact on the hemodynamics and overall function of the liver. To investigate the altered perfusion characteristics in a cirrhotic liver, Peeters et al [41] reconstructed the 3D hepatic vasculature of a cirrhotic liver that was discarded for transplantation. Detailed datasets of this liver were generated in two succinct steps: vascular corrosion casting followed-up by micro-CT imaging. Later, Claerebout performed a segmentation of the arteries to obtain an accurate model of the arterial network.

Vascular corrosion casting

The goal of vascular corrosion casting is to obtain an accurate 3D replica of the liver's vascular system. This was done by injecting a polymer solution into the hepatic artery (HA)

and portal vein (PV) until it emerged from the hepatic veins (HV) and vena cava inferior. Red and blue color dyes were also included in the solution to distinguish between the arterial and venous circulation. After polymerization, the liver was immersed in potassium hydroxide and the tissue around the hardened vessels dissolved. After maceration, only the polymerized resin that was contained in the vessel lumen remained [41, 26, 42].

Micro-CT imaging

An in-house developed high-resolution micro-CT scanner was used to obtain a 3D geometry of the liver cast. The difference between the micro-CT scanner and conventional CT-scanners lies in the fact that the sample rotated whereas the X-ray tube and flat panel detector remained static. The tube operated at 90 keV and 250 μA. The reconstruction was performed with Octopus-software (Ghent University, Ghent, Belgium). The 3D datasets were rebinned to restrict the size of the output files and the new image datasets were then converted to DICOM format to perform image processing [42].

Segmentation

The segmentation was done by Claerebout as part of her Master's thesis at the Faculty of Medicine and Health Sciences. Images were processed using Mimics Software (Materialise, Leuven, Belgium). The initial segmented 3D geometry is visible in Figure 3.1. However, the architecture of this model was very complex. Using this model as the basis for computer simulations would result in high computational expenses. As the goal of Claerebout's Master's thesis was to make a 3D print of the geometry, for which the initial geometry was also far too complex, the geometry was simplified. Only the hepatic arteries up to and including the fourth (and in some branches the fifth) generation were segmented. Arteries in further generations were excluded from the model with the tool *Cut Centerline Ending*. The reasons for segmenting only up until the level of the fifth generation were the general difficulties that arise with segmenting the smaller arteries and the feasibility of making a 3D print out of model. Similarly, in Koudehi's Master's thesis, only arteries up until the fourth generation were considered as well [26]. The segmentation itself was done based on the difference in gray values between veins and arteries. However, this difference was slight in various places, which meant arteries and veins were difficult to separate from each other. To correctly differentiate between the two, a lot of manual editing was required. With the tools *Edit Mask* and *Multiple Slice Edit* the mask was corrected. With this improved mask, a 3D model of the arterial network of the cirrhotic liver was generated.

Further manual editing was performed by Claerebout to optimize the model even more. The centerline was determined using *Fit Centerline*. The diameters of the arteries, which will be used later on in this thesis, were estimated with *Best Fit Diameter*. The largest

Figure 3.1: Initial 3D model of the arterial network of the cirrhotic liver.

diameter was the one of the inlet plane, equalling about 7.37 mm, while the smallest diameter of the outlets was about 0.97 mm. The final 3D geometry is visualized in Figure 3.2.

3.2 Surface mesh

The 3D arterial network was imported into 3-matics (Materialise, Leuven, Belgium) to obtain a smooth surface mesh. This process was done by the author in several succinct steps.

Smoothing, manual editing and remeshing

The geometry was smoothed both globally and locally, paying special attention to the parts of the body that were located near the outlets and the bifurcations. A general workflow for smoothing over the coarser parts of the body was to reduce the amount of triangles in an area, apply the Smoothing function with a specific smoothing factor and then subdivide the amount of triangles again. This process allowed for fast and extensive smoothing. For the main body of the geometry, a smoothing factor as large as 0.8 was used. However, this factor was reduced for parts of the geometry closer to the outlets (to 0.6 or even 0.4 at the outlets themselves) to prevent a rounding of the rims of the outlets. The bigger bumps of the geometry that were unable to be removed by using the Smoothing function alone were manually deleted by the author and then re-edited to obtain a more gradual transition. An example of such an edit is given in Figure 3.3. However, this editing process resulted in a very uneven mesh. So during the process as described above,

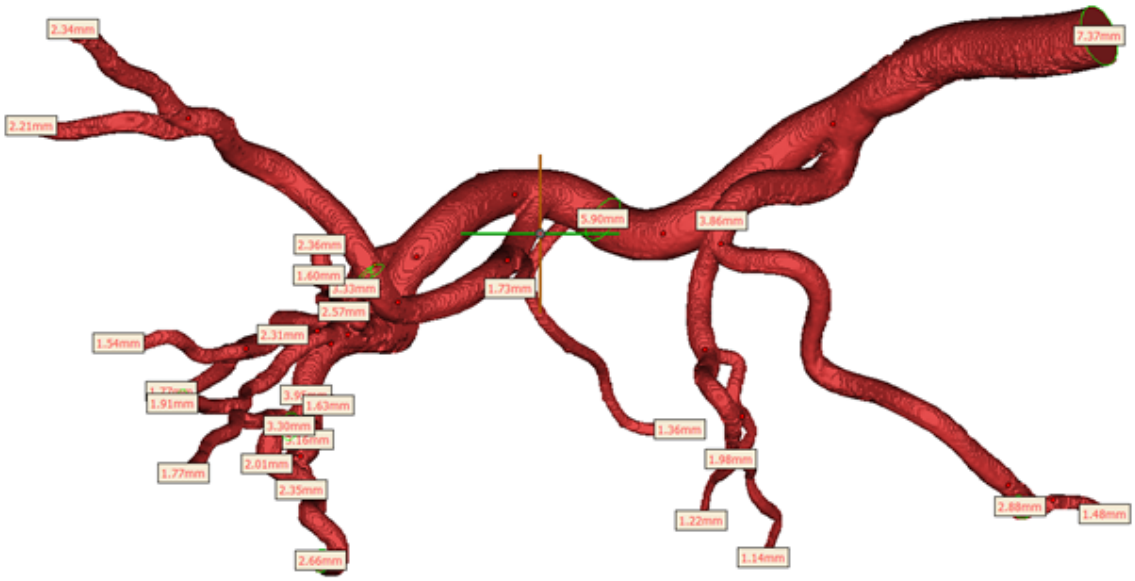

Figure 3.2: 3D model of the arterial network of the cirrhotic liver after editing by Claerebout.

the geometry was re-meshed several times using the Adaptive Remesh function (known in previous versions of 3-matic as the Auto Remesh function). The maximum geometrical error was set to 0.0225 mm, as was done in Koudehi's Master's thesis [26]. To prevent a rounding of the rims of the outlets, the option 'Preserve surface contours' was checked.

Shape modifications of outlets

As will be explained in Sections 4.1.5 and 5.1, boundary conditions of constant velocity are imposed at the outlets. To implement these boundary conditions, it is of crucial importance that the outlets have a regular, roundish shape of known size and are cut perpendicular to the vessels' centerline. The diameters of each outlet were already estimated by Claerebout. However, these were only rough estimations as some of the outlets lost parts of their round shape during the segmentation process. Therefore, most outlets were manually edited to restore their roundish shape. This was done by carefully removing and adding manually-drawn triangles and rounding the sharp edges of the outlet contours. In Figure 3.4, one of these manually edited outlets is visualized to serve as an example.

Final mesh

A final Adaptive Remesh with the same settings as before was performed. However, this time the shape measure 'Skewness' was set to a minimal threshold of 0.4. A denser mesh was opted at the bifurcations by manually subdividing the triangles in these areas. An example of such refinement is given in Figure 3.5. After this, a Gradient Remesh was performed, preserving the locally increased densities of the mesh at the bifurcations. The

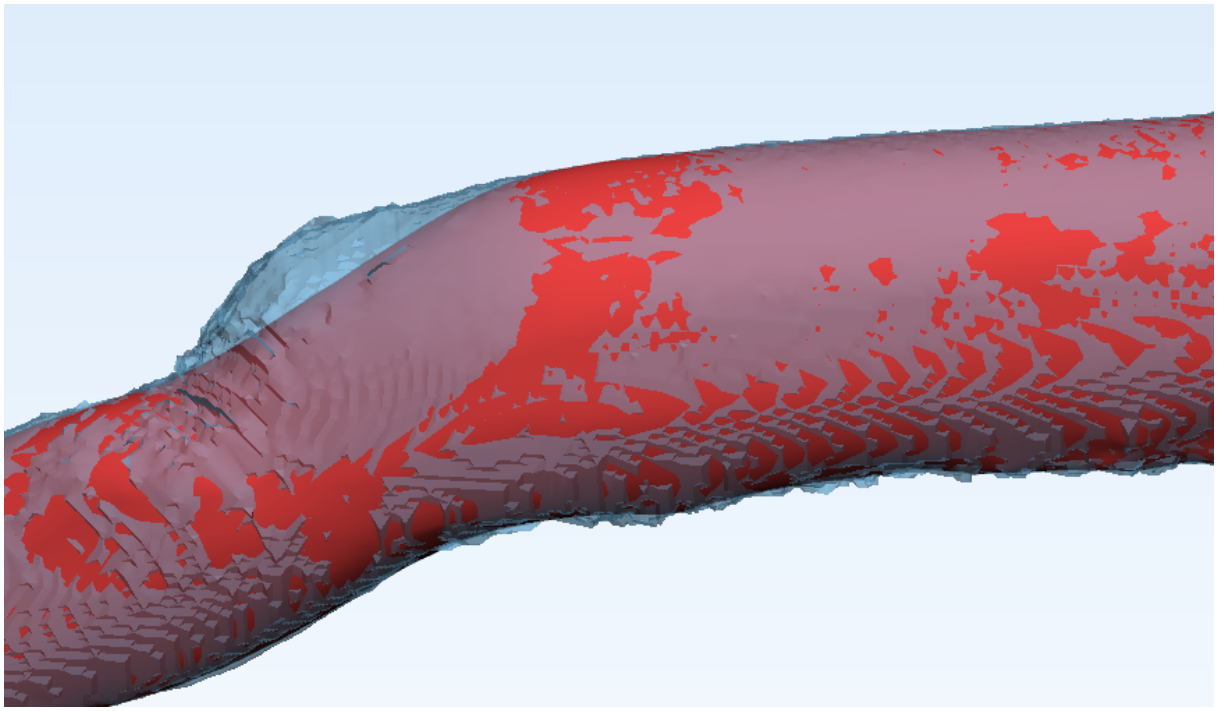

Figure 3.3: Example of a bump that was manually removed and then replaced by a smoother transition. The transparent blue geometry indicates the outline of the original geometry, while the red geometry is the edited, more gradual one.

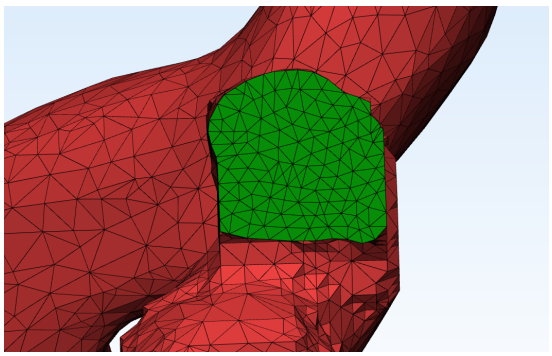

(a) Example of an outlet that had lost its round shape during the segmentation process.

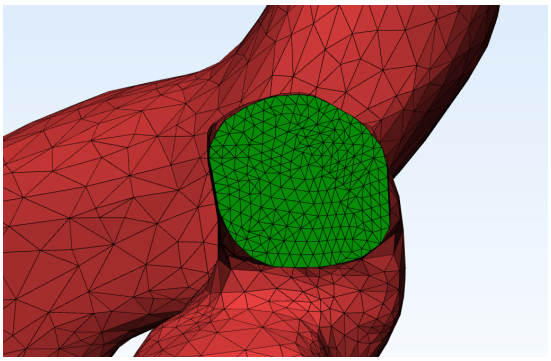

(b) Example of an outlet with a restored roundish shape.

Figure 3.4: Modification of outlet shapes.

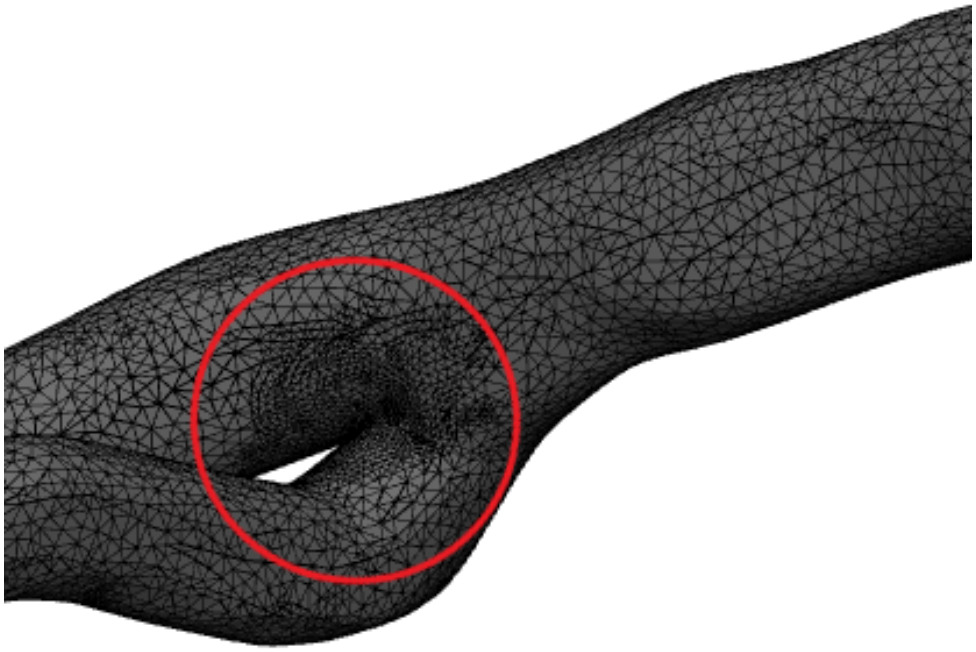

Figure 3.5: Example of a manually edited finer mesh at a bifurcation.

geometrical error was set the same as in the Adaptive Remesh before and the option 'Preserve surface contours' was also checked to prevent shape distortions at the outlets. The histogram in Figure 3.6 visualizes the distribution of the triangles of the surface mesh with regard to the shape measure 'Skewness'. As is visible, there are 0 triangles with a skewness below 0.4.

3.3 Volume mesh

3.3.1 Generation

The surface mesh was converted to .STL format and then exported into ICEM (Ansys, Canonsburg, PA, USA) to compute a volume mesh.

The global and part mesh parameters were set. The scale factor was varied from 1 to 0.1375 to generate meshes with varying densities. The optimal mesh density was determined through a mesh sensitivity analysis. The results from this analysis are reported in Section 3.3.2. The maximum global element seed size was set to 0.2 mm. The number of refinements was varied between 10 and 20 and the minimum size limit was varied

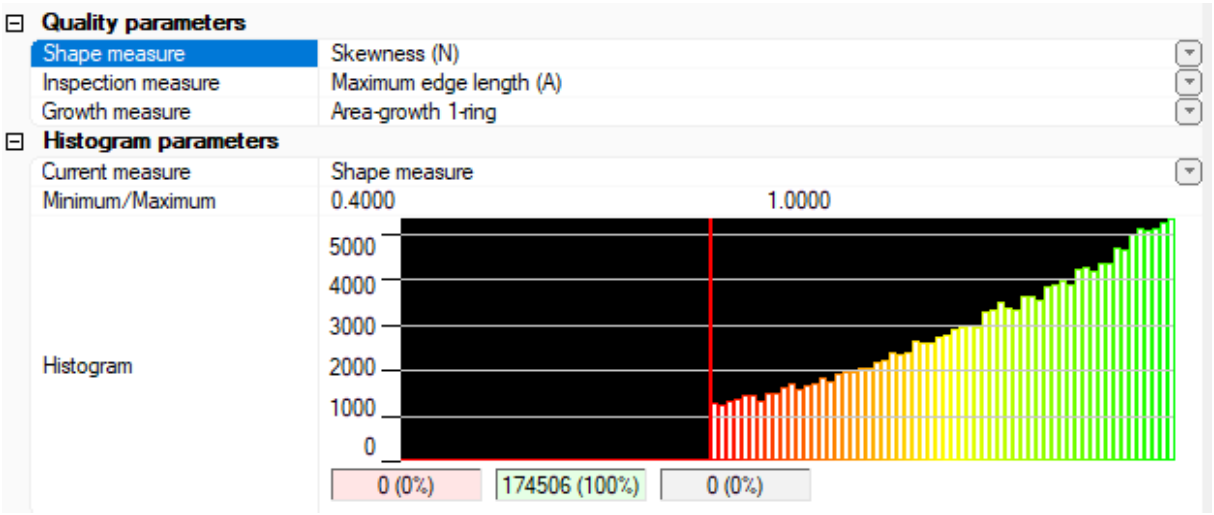

Figure 3.6: Histogram showing the distribution of triangles with regards to the shape measure 'Skewness'.

between 0.5 and 0.2 mm. The global mesh method was chosen as Octree, as this is the most robust method. The bulk of the elements were tetrahedral elements, but three prism layers at the wall of the domain were enabled to ensure a gradual transition zone between the walls and the centre of the domain [43]. The different meshes were then computed. An overview of these meshes, and the most important settings for each mesh, are given in Table 3.1.

Table 3.1: Overview of meshes.

Mesh	Elements [10^6]	Refinements	Min size	Scale	Method
1	0.482	10	0.5	1	Octree
2	1.974	15	0.2	0.5	Octree
3	3.471	20	0.2	0.35	Octree
4	5.224	20	0.2	0.2	Octree
5	7.172	20	0.2	0.1675	Octree
6	9.106	20	0.2	0.15	Octree
7	11.169	20	0.2	0.1375	Octree

Afterwards, the meshes were smoothed globally. As a final step, the meshes were checked for errors and unconnected vertices were deleted. After this, the meshes were exported to Ansys Fluent.

As is visible in Table 3.1, the number of elements in the seven meshes varied from 482 000 elements to 11 169 000 elements. In Section 3.3.2, it is described how one scenario was simulated for all these different meshes. The optimal mesh density was then determined as Mesh 6, with about 9 million elements. The quality after smoothing for the final mesh of 9 million elements is visualized in the histogram in Figure 3.7. A cross-section of this

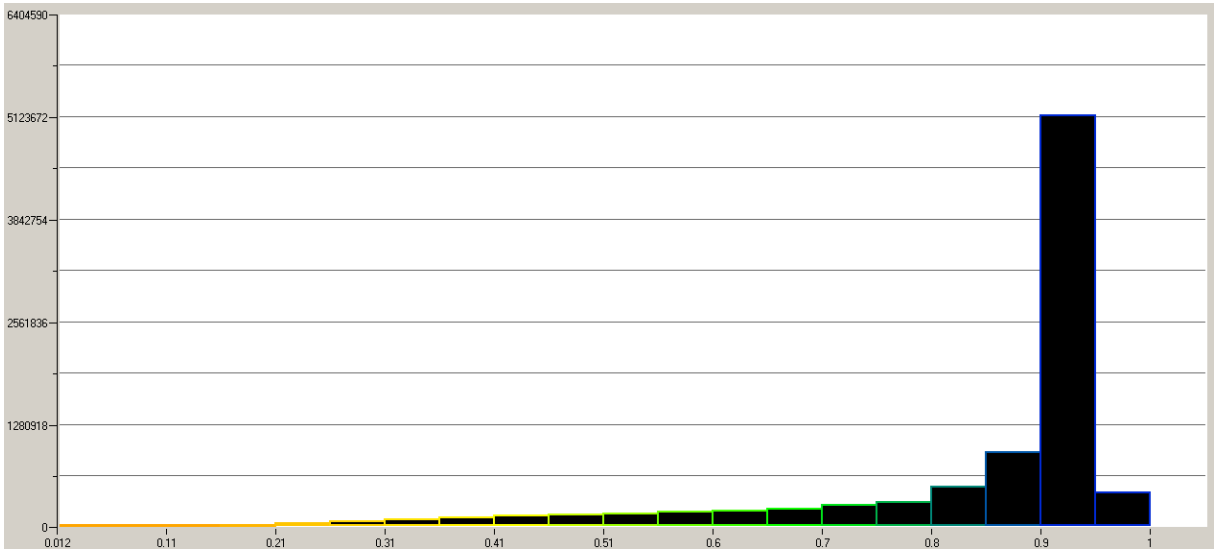

Figure 3.7: Quality histogram of the volume mesh.

mesh is shown in Figure 3.8 to visualize the tetra elements and the prism layers near the wall.

3.3.2 Mesh sensitivity analysis

As already mentioned in Section 2.3.3, models must undergo simplifications to obtain realistic results within favourable computational times. This was the reason one-way coupling between the fluid continuum and the discrete phase particles was opted ahead of two-way coupling, just as a rigid arterial was favoured instead of a vessel wall that deforms during the cardiac cycle. In the case of the volume mesh, it stands to reason that the finer the mesh, the more accurate the results will be. However, at a certain point, the mesh becomes so fine that the computational cost becomes unmanageable. Therefore, a trade-off must always be made between the chosen mesh density and the computational cost.

To this end, a mesh sensitivity analysis (MSA) was performed. The goal of the MSA is to see at what mesh density the results of the simulations begin to converge. When the results of the simulations become more or less independent of the chosen mesh density (i.e. when the changes between meshes fall beneath a critical threshold), then further increasing the number of elements has little to no use and the optimal mesh density can be chosen. For this MSA, the results of seven different mesh densities were compared for Case 1. A detailed overview of these seven meshes was given in Table 3.1. The cases will further be elaborated upon in Section 5.4.

Results

Velocity, pressure and wall shear stress After running the simulations of one case (Case 1) for the seven different meshes in ANSYS Fluent, the results were exported for

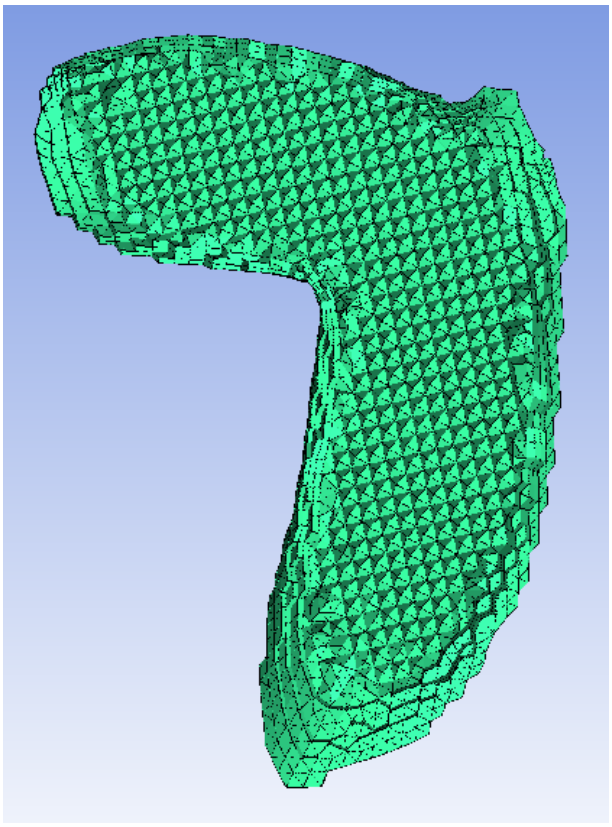

Figure 3.8: Elements of the volume mesh visualized at a bifurcation.

evaluation to CFD-Post. Three parameters were evaluated for this MSA: velocity, pressure and wall shear stress (WSS). For these three parameters, average and maximal values were computed. However, the maximum values can be misleading since they are largely affected by outliers. These outliers are only results from one cell, and do not represent the state of the fluid in the whole computational domain. Therefore, the average values were identified as more suitable.

For each mesh except Mesh 1, the relative changes (in %) with respect to the results of the previous mesh are reported. The results for pressure are reported in Figure 3.9, the results for velocity are reported in Figure 3.10, and the results for wall shear stress are reported in Figure 3.11. For all three parameters, the changes drop below 10% for Mesh 5 with about 7 million elements. However, both for average velocity and average pressure, this value is still too high. For Mesh 6 (without about 9 million elements) the changes for all three parameters drop well beyond 5%.

Particle fates In ANSYS Fluent, the particle fates (i.e. whether they escaped the domain or not, and if so, through which outlet) were reported for each of the seven simulations. With respect to the overall goal of this thesis, these particle fates were arguably an even more important factor to consider than the velocity, pressure and wall shear stress values considered in the previous section. The particle distributions for every mesh are visualized in Figure 3.12. Here, it is visible that the number of particles exiting

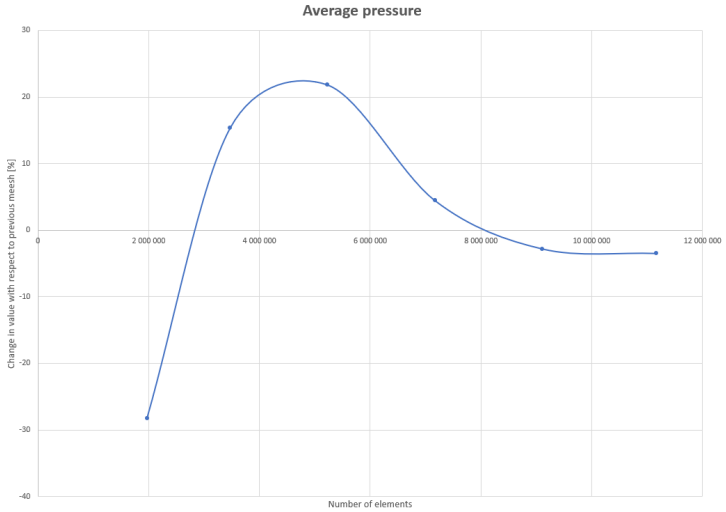

Figure 3.9: Average pressure - changes reported in % with respect to previous mesh

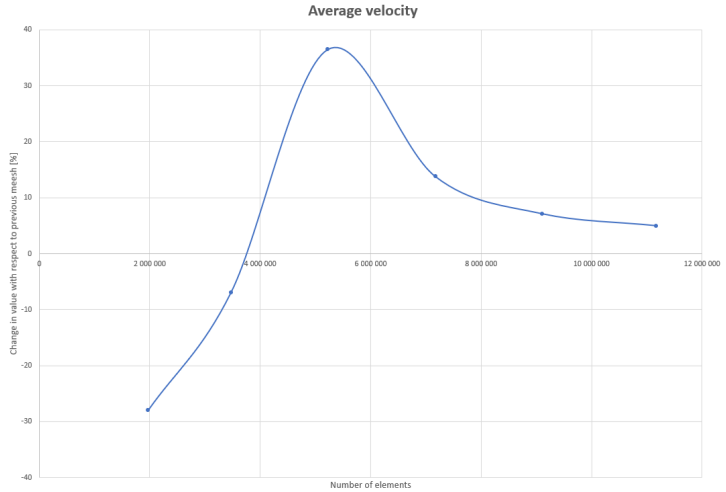

Figure 3.10: Average velocity - changes reported in % with respect to previous mesh

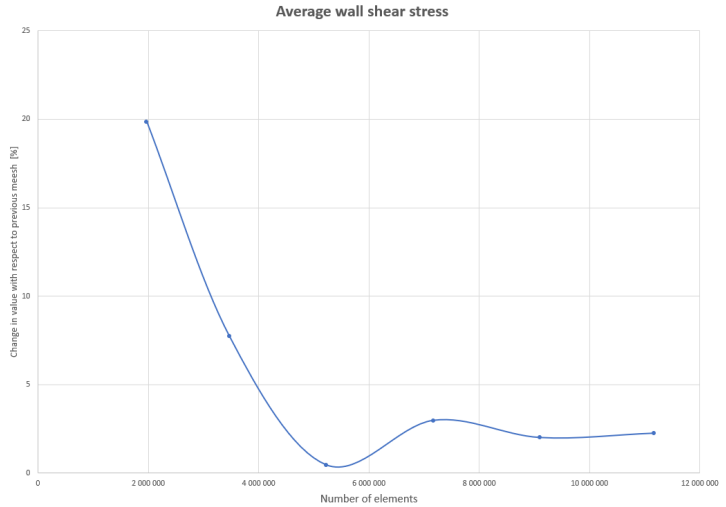

Figure 3.11: Average WSS - changes reported in % with respect to previous mesh

through a certain outlet fluctuate severely for the first meshes, but begin to converge more for the denser meshes.

Again, the values obtained for a certain mesh were compared to the outcome of the previous mesh, i.e. the next densest mesh. To this end, the absolute values of the change (in %) for each outlet was computed and then these values were averaged over all outlets. These averages are visualized in Figure 3.13 for all the different meshes.

As is visible in Figure 3.13, the reported average change for all outlets drops to about 0.36% from the 7 million mesh to the 9 million mesh and then again from the 9 million mesh to the 11 million mesh. However, as the particle distribution for each outlet will be investigated later on, the averages do not paint the full picture. Therefore, the maximum changes for each simulation (again, in absolute values) were computed and plotted in Figure 3.14. As it can be seen there, the maximal changes for both the 9 million mesh and the 11 million mesh are about 1.1%. The maximum values for the first meshes are much larger, which was already identified visually.

As a result of the MSA, the 9 million mesh was chosen as the ideal mesh and it was imported into ANSYS Fluent for the remainder of the simulations.

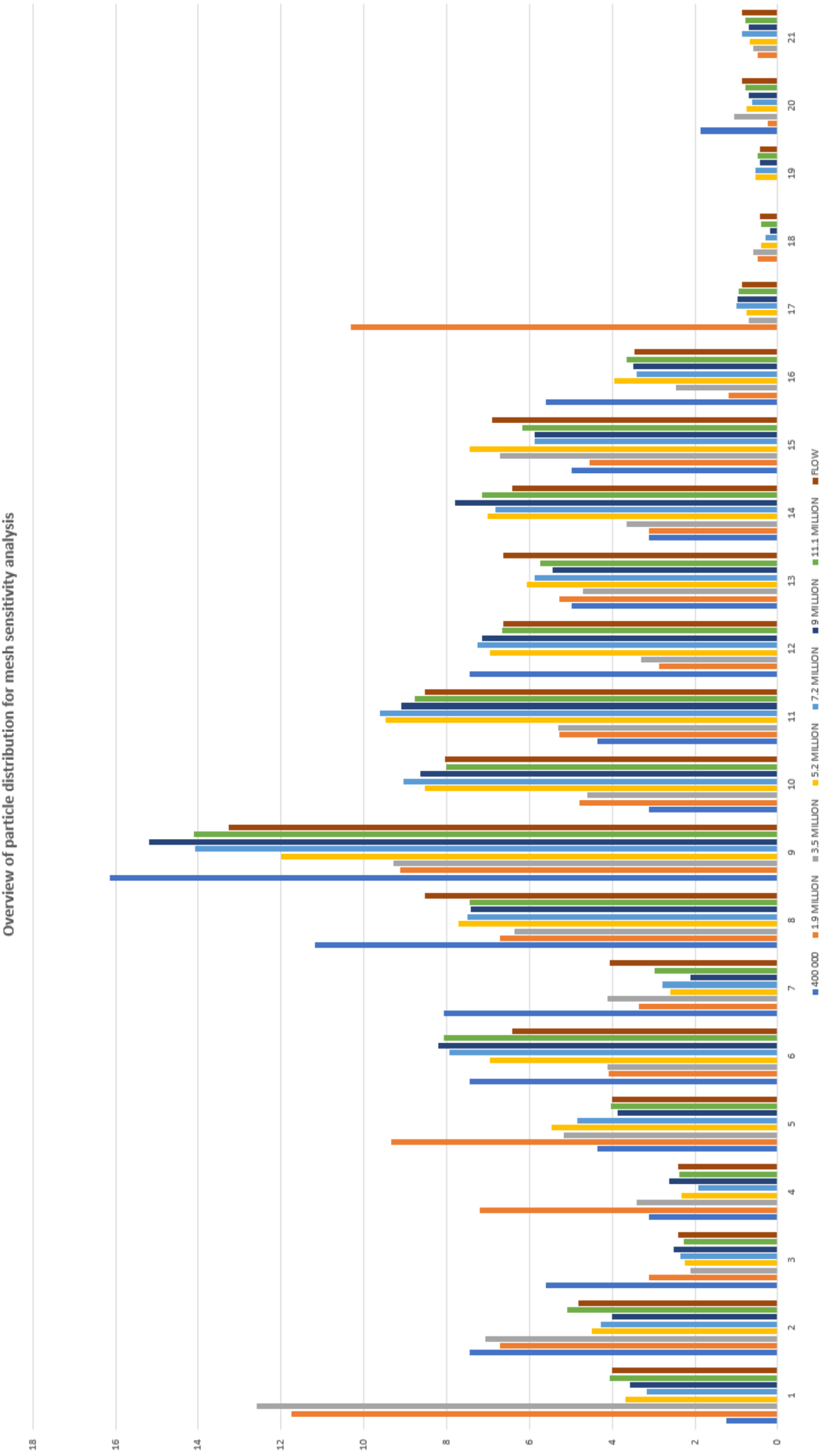

Figure 3.12: Overview of particle distribution for the different meshes.

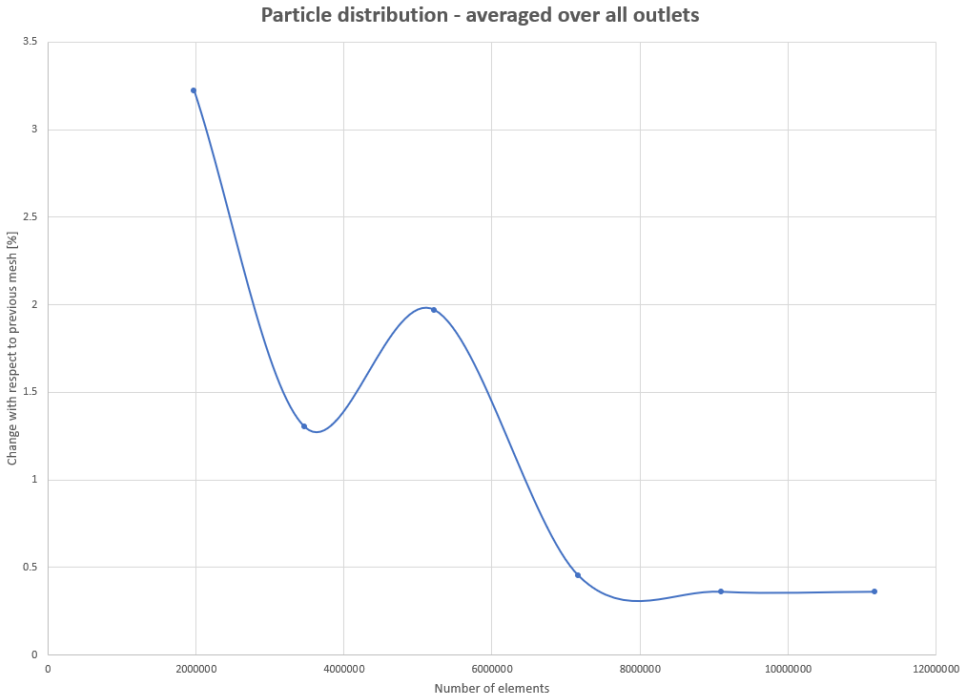

Figure 3.13: Particle distribution - change with respect to previous mesh.

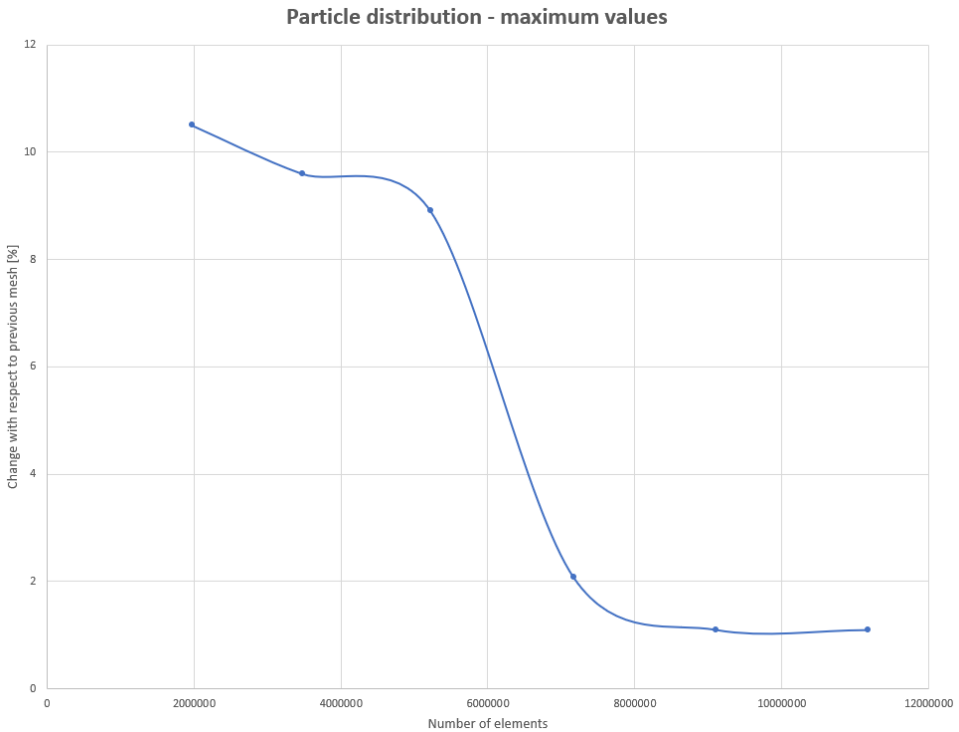

Figure 3.14: Particle distribution - change with respect to previous mesh.

Chapter 4

Computer Simulations

Computer simulations play a crucial role in the ongoing research into targeted drug delivery for liver cancer. As the PRMs are telling factors of the eventual target-specificity of the therapy, running extensive and accurate simulations of the proposed therapy allows for the optimization of treatment parameters and determination of ideal treatment conditions.

Chapter 3 mainly focused on the creation of the computational domain. This chapter will focus on the set-up of the numerical models in ANSYS Fluent. The boundary conditions briefly mentioned at the end of this chapter will be further elaborated upon in Chapter 5.

4.1 Mathematical modelling

Once the meshing of the hepatic arterial geometries was completed, the CFD software package ANSYS Fluent was used to calculate the fluid flow fields and the trajectories of the particles dispersed in the fluid. To this end, the Discrete Phase Model (DPM) was employed. The DPM follows an Euler-Lagrange approach in which the fluid is treated as a continuum in an Eulerian framework and the dispersed particles are tracked using a Lagrangian framework [39]. The mathematical equations that are important to understand the theory behind the Discrete Phase Model are explained in the following sections.

4.1.1 Blood flow

Blood is modelled as an incompressible, non-Newtonian fluid. To calculate the flow field, the following equations of continuity and linear momentum (in index notation) are solved in an Eulerian framework [44]:

$$\bigtriangledown_i u_i = 0 \tag{4.1}$$

$$\rho \frac{\partial u_i}{\partial t} + \bigtriangledown_i u_j u_i = - \bigtriangledown_i p + \bigtriangledown_j \tau_{ij} + F_i^G \tag{4.2}$$

In this set of equations, u_i is the fluid velocity, ρ is the fluid density, p is the fluid pressure, τ_{ij} is the shear stress tensor and F_i^G is the force of gravity acting on the geometry.

From Equation 4.3 it is clear that the stress tensor $\vec{\tau}$ is a function of a shear rate-dependent apparent viscosity. The non-Newtonian behaviour of blood, as represented in Equation 4.4, is given by a Quemada model that was modified to simplify numerical implementation. This model was proposed by Buchanan et al [45] and has been used in similar studies for targeted drug delivery in the liver [26, 13, 15, 37]. To calculate the shear rate, Equation 4.5 is used.

$$\vec{\tau} = \mu(\dot{\gamma})[\bigtriangledown\vec{u} + (\bigtriangledown\vec{u})^T] \tag{4.3}$$

$$\mu(\dot{\gamma}) = max\{\mu_0, (\sqrt{\mu_\infty} + \frac{\sqrt{\tau_0}}{\sqrt{\lambda} + \sqrt{\dot{\gamma}}})^2\} \tag{4.4}$$

$$\dot{\gamma} = \sqrt{\bigtriangledown\vec{u}[\bigtriangledown\vec{u} + (\bigtriangledown\vec{u})^T]} \tag{4.5}$$

In these equations, μ is the dynamic viscosity of the fluid, $\dot{\gamma}$ is the shear rate, μ_0 is the minimum viscosity, μ_∞ is the asymptotic viscosity, τ_0 is the apparent yield stress and λ is the shear stress modifier. These parameters take the following values adapted from literature: $\mu_0 = 0.00309$ Pa·s, $\mu_\infty = 0.002654$ Pa·s, $\tau_0 = 0.004360$ Pa, and $\lambda = 0.02181$ s^{-1} [26, 13, 15, 37, 45].

4.1.2 Particle trajectory calculation

The discrete particle trajectories are calculated by integrating the force balance of the particles, which is written out below in a Lagrangian framework.

$$\frac{d\vec{u_p}}{dt} = F_D(\vec{u} - \vec{u_p}) + \vec{g}\frac{(\rho_p - \rho)}{\rho_p} + \vec{F} \tag{4.6}$$

Here, $\vec{u_p}$ is the particle velocity, $\vec{u}$ is the fluid phase velocity, ρ is the fluid density, ρ_p is the particle density and F_D represents the drag force. The term on the left side of the equation is the particle inertia, which equates the forces acting on the particle (Newton's second law). The first term on the right side of the equation represents the drag force per unit particle mass, the second term represents the force of gravity and the third term represents an additional acceleration caused by the pressure gradient in the fluid [39].

The drag force F_D can be calculated as:

$$F_D = \frac{18\mu}{\rho_p d_p^2}\frac{C_D Re}{24} \tag{4.7}$$

Here, μ is the molecular viscosity of the fluid, d_p is the particle diameter and C_D is the drag coefficient. Re represents the relative Reynolds number of the particle, which

can be calculated as:

$$Re = \frac{\rho d_p \mid \vec{u_p} - \vec{u} \mid}{\mu} \tag{4.8}$$

The drag coefficient C_D, is derived from the drag law for spherical particles [39].
The fluid pressure force, $\vec{F}$, can be calculated as:

$$\vec{F} = \frac{\rho}{\rho_p} \vec{u_p} (\bigtriangledown \vec{u}) \tag{4.9}$$

It should be noted that other forces can be included in the expression of $\vec{F}$, such as the virtual mass force or the Saffmann-type lift force. However, it has been shown that these forces are of negligible influence on the particle trajectories [44]. Therefore, these forces are not included in equation 4.9.

Integration of equation 4.6 directly yields the particle velocities u_p at each point of the trajectory. By integrating again, the particle positions can be obtained, which gives the trajectory itself [39].

4.1.3 Particle properties

Specific properties of the discrete particles, such as diameter and density, were adapted from [19]. Two types of particles were modelled: SIR-Spheres and Thera-Spheres. Both of these are commercially available Y-90 microspheres that are used for radioembolization procedures. Their characteristics are given in Table 4.1. As was already noted in Section 2.3.2, Koudehi [26] and Sánchez [14] both concluded that particle density plays a significant role in the particle distribution. Therefore, both the SIR-Spheres and the denser Thera-Spheres were included in this study.

Table 4.1: Overview of microsphere characteristics. Adapted from [19].

Characteristics	**SIR-Sphere**	**Thera-Sphere**
Sphere material	Resin	Glass
Diameter range [μm]	20-60	20-30
Specific gravity [g/dL]	1.6	3.6
Activity per particle [Bq]	50	2500
Amount of particles per vial [10^6]	40-80	1.2

4.1.4 Vessel walls

The wall was modelled as stationary with a no-slip condition at the boundary. Particle collisions with the vessel walls were considered elastic, which meant that the particles retained all of their momentum after collision. This can easily be done in FLUENT by setting the tangent and normal coefficients or restitution to 1 ("reflect") [39].

4.1.5 Outlet boundary condition

A constant velocity was imposed at the outlets of the arterial network. In both Koudehi's Master's thesis [26] and Sánchez's Bachelor's thesis [14], the velocity values were derived using Murray's law. Below, a short overview of Murray's law is given and a brief note is made on why a different approach was opted for this thesis. The exact computation of the outlet boundary condition for the specific flow values of this liver is done in Sections 5.1, 5.2 and 5.4.

Murray's Law

Murray has reasoned that branching vascular systems, through natural selection, have evolved to an optimum arrangement in which the flow inside a vessel is achieved with the least amount of biological work required. By minimizing the energy function that defines the amount of energy that is necessary to maintain blood flow in a vessel, Murray found that [46]:

$$Q \propto R^3 \tag{4.10}$$

Here, Q is the volumetric flow rate through a vessel and R is the radius of the vessel. This linearity gave rise to the popular Murray's law, which states that the cube of the radius of the parent vessel (upstream of the bifurcation) is the sum of the cubes of the radii of the daughter vessels (downstream of the bifurcation) [46].

$$R_{parent} = \sum R^3_{daughter} \tag{4.11}$$

Alternatively, Murray's law can be stated as:

$$\frac{Q_{daughter}}{Q_{parent}} = \left(\frac{R_{daughter}}{R_{parent}}\right)^3 \tag{4.12}$$

Both Koudehi [26] and Sánchez [14] extracted the radii of the vessels from Mimics and used this information to calculate the flow distribution in the hepatic arterial tree. Sánchez [14] noted that, in the cases where Murray's Law was not perfectly accomplished, Equation 4.12 could be replaced by Equation 4.13:

$$\frac{Q_{daughter}}{Q_{parent}} = \frac{R^3_{daughter}}{\sum_{i=1}^{n} R^3_{daughter,i}} \tag{4.13}$$

Note on the validity of Murray's Law

As is obvious from Equation 4.12, the flow in a certain branch only depends on its radius and the radius of and the flow through its parent vessel. However, cancer burden might have a considerable effect on flow distribution. Since this effect is not included in Murray's Law, an alternate boundary condition was considered which is based on the

arterial perfusion model developed by Aramburu et al [2]. The theoretical framework of the arterial perfusion model and the practical implementation of the alternate boundary condition for specific datasets used in this thesis will be discussed in Sections 5.1 and 5.2.

4.1.6 Inlet boundary condition

A constant velocity was imposed at the inlet plane. However, since the specific flow characteristics of the hepatic arterial system of the patient were not measures, the flow values had to be derived in a different manner. In both Koudehi's Master's thesis [26] as Sánchez's Bachelor's thesis [14], the flow in the proper hepatic artery (PHA) was estimated by drawing reported values from literature and calculating the mean flow. Here, a different workflow was opted since the outlet boundary conditions in this study were very different from the outlet boundary conditions in the works of Koudehi [26] and Sánchez [14]. First, the outlet boundary condition was derived. The overview of this process is given in Sections 5.1, 5.2 and 5.4. Then, by applying the principle of mass conservation, the inlet volumetric flow rate was derived. Once the flow through the inlet plane was determined, the velocity of blood at the inlet plane was calculated as follows:

$$v_{inlet} = \frac{Q_{inlet}}{A_{inlet}} \tag{4.14}$$

Here, the inlet volumetric flow rate is denoted as Q_{inlet}. A_{inlet}, which is the area of the inlet plane given that the diameter of the inlet plane was estimated in Mimics to be around 7.37 mm, equals 42.66 mm^2. The exact computation of the inlet boundary condition for the specific values of this liver is done in Section 5.5.

4.1.7 Solution methods

As for the solution methods in ANSYS Fluent, the SIMPLE scheme was chosen for the pressure-velocity coupling. The spatial discretization technique used was Least Squares Cell Based for the gradient, Standard for the pressure and Second Order Upwind for momentum.

The maximum number of time steps that the particles were tracked was set to 1 million. An automated tracking schema was chosen that switches automatically between the high order trapezoidal schema and the low order implicit scheme. A tolerance of 10^{-5} was set.

All one-way steady simulations were run in ANSYS Fluent. The absolute residuals were always lower than 10^{-3}, which equals a drop of least three orders of magnitude. An overview of the different simulations is given in Table 5.8.

Chapter 5

Boundary Conditions

The alternate boundary conditions as implemented in this thesis aim to more accurately describe the impact of cancer burden on flow and particle distribution throughout the arterial network. The theoretical framework behind this boundary condition (named the arterial perfusion model for future reference) was first proposed by Aramburu et al in [2]. This arterial perfusion model is the focus of Section 5.1, where all the relevant equations and insights of the work done by Aramburu et al [2] are explained. However, to be able to implement this model and determine the actual boundary condition, several key pieces of patient-specific information need to be obtained. In Section 5.2, these necessary pieces of information are identified and the manner in which they were determined, is explained. In Section 5.3, the simplifications and fallacies of the arterial perfusion model are discussed.

In this thesis, the goal is estimate the impact of cancer on particle distribution by investigating the particle distribution in eleven different cancer scenarios. The scenarios are explained in Section 5.4. For each of these scenarios, the arterial perfusion model is implemented and the new outlet boundary conditions are determined. From these results the flow distribution throughout the arterial network can be determined. Since particle distribution tends to match flow split, the flow distribution graphs are given and interpreted for each scenario. Furthermore, from these outlet boundary conditions the inlet boundary condition can be derived. This is done in Section 5.5.

5.1 Arterial perfusion model: theoretical framework

As opposed to Murray's law, the arterial perfusion model describes an outlet boundary condition that heavily depends on the size and location of the tumour nodules within the branching arterial network. The theoretical framework, which was developed by Aramburu et al [2], will be explored here.

5.1.1 Identification of arterial perfusion parameters

The key insight of the study conducted by Aramburu et al [2] is that the arterial perfusion of healthy tissue differs from the arterial perfusion of the cancerous tissue. With this distinction in mind, three different arterial perfusion parameters were identified:

- $k_{1,s}$: arterial perfusion of the healthy liver
- $k_{2,s}$: arterial perfusion of the cancerous tissue in the diseased liver
- $k^{\star}_{1,s}$: arterial perfusion of the normal tissue in the diseased liver

Generally, the arterial perfusion parameter k is obtained as the ratio of arterial flow to a specific segment over the volume of said segment:

$$k = \frac{q}{V}\left[\frac{mL}{min \cdot mL}\right] \tag{5.1}$$

In Figure 5.1, a healthy liver segment and a diseased liver segment are visualized. For the healthy liver segment, the arterial flow to the healthy segment is $q_{0,s}$ and the volume of the healthy segment is $V_{0,s}$. For the cancerous liver segment, $V_{c,s}$ is the volume of the tumour and $q_{c,s}$ is the arterial flow specifically to the tumour. The normal tissue of the cancerous liver segment is again denoted as $V_{0,s}$ while q_s is the total arterial flow to the segment, thus including both the flow terms to the normal and the tumour tissue of that segment. $\triangle V_s$ is an alteration of the normal liver volume, either negative due to liver shrinkage or positive due to regeneration. Adapting Equation 5.1, formulas for each of the three different arterial perfusion parameters can be defined using the information in Figure 5.1:

$$k_{1,s} = \frac{q_{0,s}}{V_{0,s}} \tag{5.2}$$

$$k_{2,s} = \frac{q_{c,s}}{V_{c,s}} \tag{5.3}$$

$$k^{\star}_{1,s} = \frac{q_s - q_{c,s}}{V_{0,s} + \triangle V_s} \tag{5.4}$$

5.1.2 Determination of arterial perfusion parameters

From a practical standpoint, the arterial perfusion parameters k can either be determined through computer tomography (CT) perfusion imaging or by directly computing them as the ratio of total blood flow rate to the liver segment over volume of the liver segment. However, in the case that both CT perfusion images and direct measurements of flow rate or volume are unavailable, Aramburu et al [2] proposed to use arterial perfusion values derived from literature. The three arterial perfusion parameters can then be determined

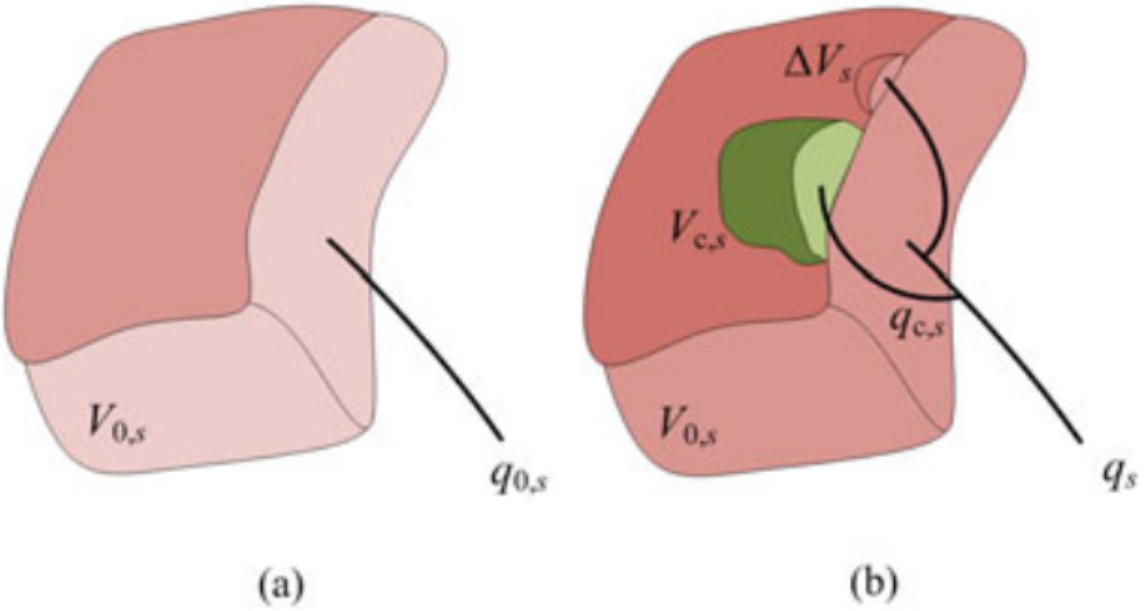

Figure 5.1: Arterial perfusion of a healthy liver segment (a) and a tumour-bearing liver segment (b). Adapted from [2].

as the average of the values collected from literature. Furthermore, Aramburu et al [2] also made several assumptions to simplify the model. First, they assumed that the three perfusion parameters had the same value for each of the liver segments ($k_{1,s} = k_1, k^\star_{1,s} = k^\star_1, k_{2,s} = k_2 \ \forall s$) and that they remained constant within these segments. Second, they assumed that the normal tissue of the cancerous segment behaved similarly to the healthy tissue (at least with respect to perfusion), which resulted in the simplification $k_1 = k^\star_1$. Taking these simplifications into account, Aramburu et al [2] computed literature-averaged values for both perfusion parameters k_1 and k_2: $k_1 = 0.10\ ml\ min^{-1}\ ml^{-1}$ and $k_2 = 0.415\ ml\ min^{-1}\ ml^{-1}$ [2]. It should be noted that the perfusion parameter for cancerous tissue is over four times larger than the perfusion parameter for healthy tissue. This stands in stark contrast with Murray's law, where the same perfusion parameter for all types of tissue was implicitly assumed.

5.1.3 Determination of the outflow boundary condition

From Equations 5.2,5.3 and 5.4 it can be shown that, for healthy liver segments:

$$q_{0,s} = k_1 V_{0,s} \tag{5.5}$$

$$q_s = (V_{0,s} + \triangle V_s)k^\star_1 + V_{c,s}k_2 \tag{5.6}$$

The arterial blood flow rate through diseased tissue can now be linked to the healthy

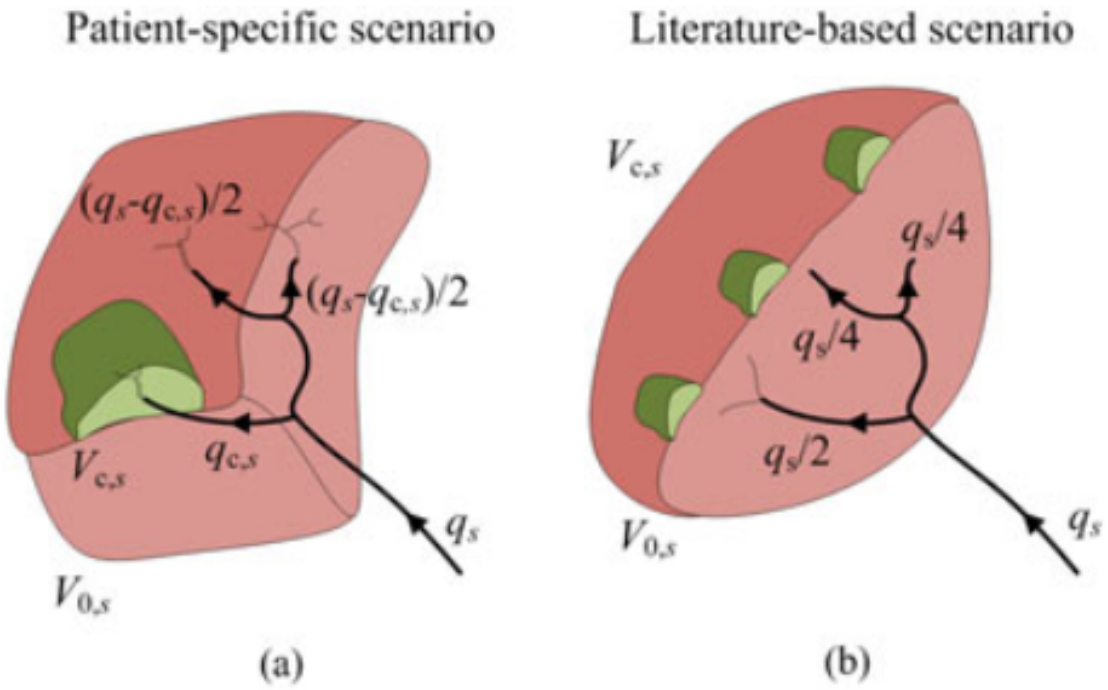

Figure 5.2: Arterial perfusion of a diseased liver segment: patient-specific scenario (a) and a literature-based scenario in which a homogeneous distribution of tumour nodules within the segment is assumed (b). Adapted from [2].

blood flow rate:

$$q_s = (K_{h,s} + K_{c,s})q_{0,s} \tag{5.7}$$

where $K_{h,s} = (1 + \frac{\triangle V_s}{V_{0,s}}) \cdot \frac{k_1^\star}{k_1}$ and $K_{c,s} = \frac{V_{c,s}}{V_{0,s}} \cdot \frac{k_2}{k_1}$.

Note that, if the volume of each healthy liver segment is known, $q_{0,s}$ can easily be determined through Equation 5.5. It should also be noted that Equation 5.7 only gives a formula for the arterial blood flow rate through each segment, while the goal is to determine the arterial flow rate through each outlet. Therefore, the relationship between the segmental flow rate and flow rate through the outlet must be determined. This relation will depend highly on the degree of branching of the arteries and the distribution of the tumours within a segment. This is visualized in Figure 5.2.

Figure 5.2 supposes two scenarios: the patient-specific scenario, in which the relative location and distribution of the tumours within the segment is known, and the literature-based scenario, in which a homogeneous distribution of the tumour nodules within a segment is assumed. In this last case, the flow split can be calculated purely based on the degree of branching for each outlet. To keep the flow split calculations relatively straightforward, the literature-based scenario was assumed from here on.

Thus, the arterial flow rate feeding an outlet m can be found as:

$$q_{m,s} = x_{n,s} q_s = x_{n,s}(K_{h,s} + K_{c,s}) q_{0,s} \tag{5.8}$$

where $x_{n,s}$ is the flow rate ratio determined by the degree of branching n for an outlet m. If the flow rate $q_{m,s}$ through each outlet is found, then, knowing the size of the outlet, a constant velocity can be imposed as the outflow boundary condition.

How the degree of branching can be determined for specific datasets will be the focus of Section 5.2.

5.2 Arterial perfusion model: implementation

To implement the theory as described above into outlet boundary conditions for specific datasets, several key pieces of information are still missing.

First, Aramburu et al [2] stressed the importance of computing several volume measures regarding both the healthy and the diseased state. These are necessary to determine the parameters $K_{h,s}$ and $K_{c,s}$ in Equation 5.7. Since patient-specificity is key throughout this whole process, it is preferred that these volume measures are taken specifically for every patient. However, if such patient-specific measures are not available, Aramburu et al [2] reported that these values could be drawn from literature. The determination of these volume measures are the focus of Section 5.2.1.

Second, it is necessary that for every outlet it is known in which segment it is located, otherwise Equation 5.8 cannot be solved. To compute the flow rate ratio $x_{n,s}$ it must be determined how many bifurcations a particle has to pass before reaching a certain outlet. This is known as the degree of branching. The process of how these two crucial pieces of information were obtained for every outlet is outlined in Section 5.2.2.

When all of this information is obtained, all of the equations presented in Section 5.1 can be solved, and the flow through each outlet of the computational domain can be determined.

5.2.1 Volume measures

For the computation of parameters $K_{h,s}$ and $K_{c,s}$, it is necessary that the following volume measures are known for every patient:

- The total healthy liver volume, V_0
- The volumes of each of the healthy liver segments, $V_{0,s}$
- The volumes of each of the tumour nodules within each segment, $V_{c,s}$ When the total volume of cancerous tissue for each of the liver segments is known, the relative burden of the tumour in that segment can be determined.

- The alteration of the healthy liver volume due to liver shrinkage or regeneration, $\triangle V_s$

These values will be determined one by one in the sections below. Comments will also be made on their patient-specificity.

Healthy liver volume

For the healthy liver used in their study, Aramburu et al reported a total volume of 1510 ml [2]. However, since the cirrhotic liver in this thesis appeared larger than that, the volume was estimated using Mimics. The outline of the liver mass was marked in several slices and then the volume was calculated by interpolating between these slices using the *Multiple Slice Edit* tool. The volume obtained for the total healthy liver was about 2498 ml.

Healthy liver segment volumes: $V_{0,s}$

Since the delineation of the liver segments relies on the identification of hepatic structures that are not visible in all slices (see Section 5.2.2), the estimation of the volumes of each of the segments using the *Multiple Slice Edit* tool as before is significantly more complex than the estimation of the total liver volume. Therefore, it was opted to use the percentages of the total volume that each segment takes up as reported by Aramburu et al [2]. These percentages were multiplied with the total healthy liver volume, determined as 2498 ml above, to obtain the segmental volumes. These percentages and the volumes of the liver segments of the cirrhotic liver used in this thesis are listed in Table 5.1 [2].

Table 5.1: Volumes of healthy liver segments. Adapted from [2].

Liver segment	Percentage of total volume [%]	Segment volume [ml]
1	4.0	101.63
2	7.9	200.71
3	9.5	241.36
4	13.6	345.53
5	12.6	320.12
6	7.9	200.71
7	16.8	426.83
8	26.1	663.11

Relative tumour burden within each segment: $V_{c,s}$

Aramburu et al [2] also reported a tumour-bearing liver volume of 2157 ml, which is an average volume computed from patients with colorectal liver metastases [47]. Keeping

in mind that the total healthy liver volume in their case was 1500 ml, this accounts for a total tumour mass of about 671 ml. However, in this thesis, the total tumour mass and the division of these tumour nodules across the different liver segments were purely hypothetical, as the liver considered here was a cirrhotic one and not a cancerous one. Several hypothetical cases were considered, varying in total tumour burden and relative division of tumour burden across the different segments. These cases were used to estimate the impact of tumour burden on the particle distribution. Since the parameter $V_{c,s}$, which describes the tumour volume for each segment, can only be considered for each case specifically, they will be reported later on when the cases themselves are discussed in Section 5.4.

Alteration of healthy liver volume: $\triangle V_s$

Just as in the study conducted by Aramburu et al [2], the total alteration of the healthy liver volume due to either liver shrinkage or liver regeneration was considered to be zero. This was done because, according to Aramburu et al [2], only in slowly progressing tumours there could appear a regenerative-related increase in liver mass, which they note to be very uncommon. Likewise, the authors note that the shrinkage of liver mass due to tumour compression of the portal venules could also be neglected in most cases. Therefore, $\triangle V_s$ was set to 0.

5.2.2 Domain outlet specificities

To solve Equation 5.8, it is necessary that two things are known for every outlet:

- In which of the 8 liver segments each outlet is located.
- The amount of bifurcations a particle has to pass before reaching the outlet (= the degree of branching).

To determine these two crucial pieces of information, the following steps were taken. First, a schematic map of the arterial network was drawn, visualizing the degree of branching for every outlet. Then, relevant vascular structures such as the hepatic and portal veins were identified on the CT scans and the division of the liver into the 8 segments was done based on these vascular structures. Finally, for each of the outlets, the segment which it perfused was identified, thereby obtaining the last piece of information necessary to implement the arterial perfusion model for this specific dataset.

I. Identification of the branching arterial network

The arterial network was defined by the author by manually scrolling through the 3D model and the accompanying CT scans and then mapping out every branch and bifurcation until an outlet was reached. Every outlet was numbered to make referencing easier.

A schematic overview of all the 21 outlets of the arterial network are given in Figure 5.3. Note that outlets 1 to 5 are located in segments perfused by the left hepatic artery (LHA) and outlets 6 to 21 are located in segments that are perfused by the right hepatic artery (RHA). The lengths of the branches in the arterial map were arbitrarily chosen.

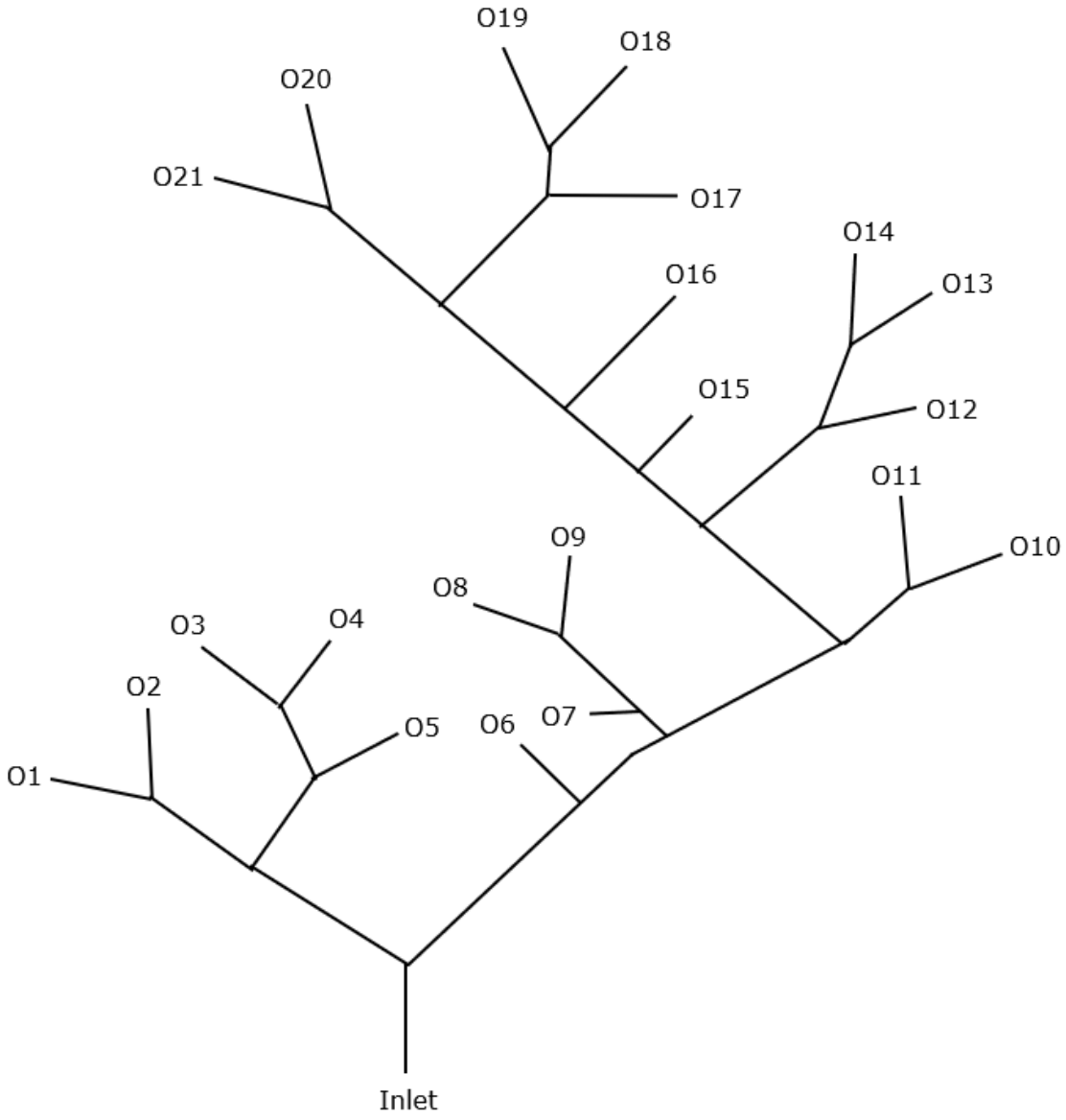

Figure 5.3: Schematic overview of the 21 outlets in the arterial network.

Effective branching factor With the arterial network entirely mapped out, the degree of branching for every outlet can easily be determined by visual inspection. In the model proposed by Aramburu et al [2], the degree of branching at the inlet equals one, and for every bifurcation a hypothetical particle has to pass before reaching a specific outlet, one must be added to the degree of branching. This degree of branching is an important parameter because it determines flow split along the hepatic arterial tree. It was assumed

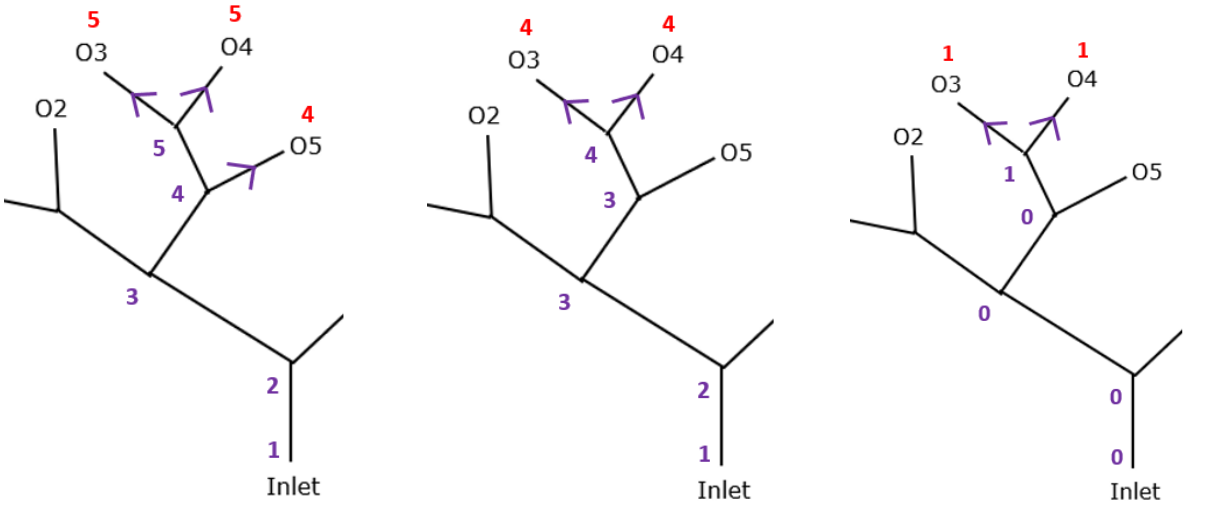

(a) Degree of branching.

(b) Corrected degree of branching, taking into account that Outlet 5 does not perfuse the same segment s as Outlets 3 and 4

(c) Effective branching factor computed for the situation in (b)

Figure 5.4: Widening the concept of degree of branching to *effective branching factor*.

that the flow split of the arteries irrigating the same segment is done symmetrically and homogeneously according to the degree of branching. In practice, this means if Outlets 3, 4 and 5 (denoted as O3, O4 and O5 in Figures 5.3 and 5.4, respectively) perfuse the same segment, Outlets 3 and 4 will each only receive half the blood supply that Outlet 5 receives because their degree of branching is one higher. This situation is shown in the left panel of Figure 5.4. The numbers in purple next to the bifurcation denote the degree of branching.

That being said, it should also be taken into account that outlets perfusing the same segment can be spread throughout the netowrk and have highly varying degrees of branching. If two arteries feeding the same segment are separated by several branches feeding other segments, the extra bifurcations these extra-segmental branches add to the degree of branching should not be taken into account as this would greatly decrease the amount of flow to the second artery (namely, by a factor of two for every extra bifurcation). For example, if Outlet 5 perfuses a different segment than Outlet 3 and Outlet 4, the bifurcation that splits flow among Outlet 5 on the one side and Outlets 3 and 4 on the other side should not be taken into account when computing the effective degree of branching. This situation is shown in the middle panel of 5.4. This also means that, for every outlet perfusing segment s, the degree of branching of the shallowest, least-deep outlet perfusing s should equal one because all shallower outlets are perfusing a different segment than s. For every deeper-lying outlet the degree of branching should increase as described above, only counting the bifurcations that split flow to the same segment s. This makes sense intuitively: it should not matter whether the outlets perfusing segment s are located near

the inlet or far down the hepatic arterial tree, it is only the relative branching within that segment that matters.

These important considerations give rise to a new term, the *effective branching factor*. The effective branching factor corrects the degree of branching for the fact that only flow split among outlets feeding the same segment should be considered. This new effective branching factor in shown in the right panel of 5.4. Note that, if Outlet 5 were to perfuse the same segment s as Outlets 3 and 4, then the effective branching factor of Outlet 5 would increase to 1 and the effective branching factors of Outlets 3 and 4 would increase to 2.

This term was not explicitly defined in the model proposed by Aramburu et al [2] because the organization of the different outlets and feeding segments was more hierarchical there and all the arteries feeding the same segment were neatly grouped together. However, it was also implicitly assumed as Aramburu et al deducted the branching factor of the shallowest outlet feeding a certain segment from the overall branching factor to determine the flow split. In this work, the concept of effective branching factor is made explicit because the architecture of the arterial tree is slightly more chaotic.

This information solves the problem raised by Equation 5.8, which sought to link the segmental flow rate q_s to the flow rate through each outlet, $q_{m,s}$. This gives rise to the following formula:

$$q_{m,s} = \frac{q_s}{2^n} \tag{5.9}$$

where n is the effective branching factor and 2^n plays the role of the flow rate ratio term $x_{n,s}$ first introduced in Equation 5.8.

However, since these effective branching factors depend on the segmental division of the outlets, they can only be determined when it has been identified which outlets perfuse which segments. The segmental perfusion characteristics for each outlet will be determined in the sections below. The degrees of branching and the effective branching factors for every outlet are given in Table 5.2.

II. Identification of the relevant vascular structures

Identification of the eight liver segments according to the Coinaud classification was done by using certain vascular structures as references, most notably the hepatic veins and the portal veins. The middle hepatic vein divides the liver into a right lobe (segments V, VI, VII and VIII) and left lobe (segments II, III and IV). The right hepatic vein further separates the right lobe into an anterior segment (segments V and VIII) and a posterior segment (segments VI and VII). The left lobe can also be divided into a lateral segment (segments II and III) and a medial segment (segment IV) but this division should be done by drawing a line from the confluence of the left hepatic vein and middle hepatic vein at the inferior vena cava to a structure called the falciform ligament [17]. The segmentation

of the liver based on the location of the hepatic veins as described above is visualized in Figure 5.5. So, to properly define the segments of the liver, the hepatic veins must first be identified on the CT scans.

The middle hepatic vein The proximal part of the middle hepatic vein travels more or less horizontally, so it is visible in axial slices as a straight line. This structure is visualized in Figure 5.7. However, the distal part of the middle hepatic vein travels in the craniocaudal direction, so it can only be seen in axial slices as a circle [48]. This is visible in Figure 5.8.

The right and left hepatic veins The right and left hepatic veins can only be visualized in certain axial slices. The right hepatic vein is visualized in Figure 5.9, the left hepatic vein is visualized in Figure 5.10.

The portal vein bifurcation Furthermore, the locations of the segments do not only depend on the location within the axial plane but also on the location of the plane on the body axis. This is clear in Figure 5.6. When a cross-sectional imagine at level A is taken, only segments II, IV(A), VII and VIII can be identified. However, when a cross-sectional image is taken at level C, segments III, IV(B), V and VI are visible. Thus, some sort of anatomical reference for the axial level is also needed. To this end, the plane passing by the portal vein bifurcation will serve as a hallmark [48]. On all axial slices above this plane segments II, IV(A), VII and VIII will be identified, while on all axial slices below this reference plane lie III, IV(B), V and VI will be identified.

Once the relevant vascular structures were identified, the lines defining the different segments were drawn according to the guidelines described above.

III. Determination of the segmental perfusion characteristics of every outlet

To successfully implement the arterial perfusion model, it was necessary to determine which of the eight liver segments are perfused by which of the 21 outlets. To this end, the author used Mimics to manually navigate the cursor to each outlet of the 3D model and then identify in the corresponding CT slice in which segment it was located by using the guidelines as described above. A specific example of this process for Outlet 8 is visualized in Figure 5.12. Since the end of this outlet (visible at the center of the yellow circle) was located just next to the middle hepatic vein, identification was relatively easy. As described above, the middle hepatic vein separates the liver into a right and a left lobe and is used as a division between segment IV on the anatomical left (right side of the image) and V or VIII on the anatomical right (left side of the image). Even the axial level of the slice was not of much importance here, since segment IV is the only segment that stretches both above and below the plane of bifurcation of the portal vein.

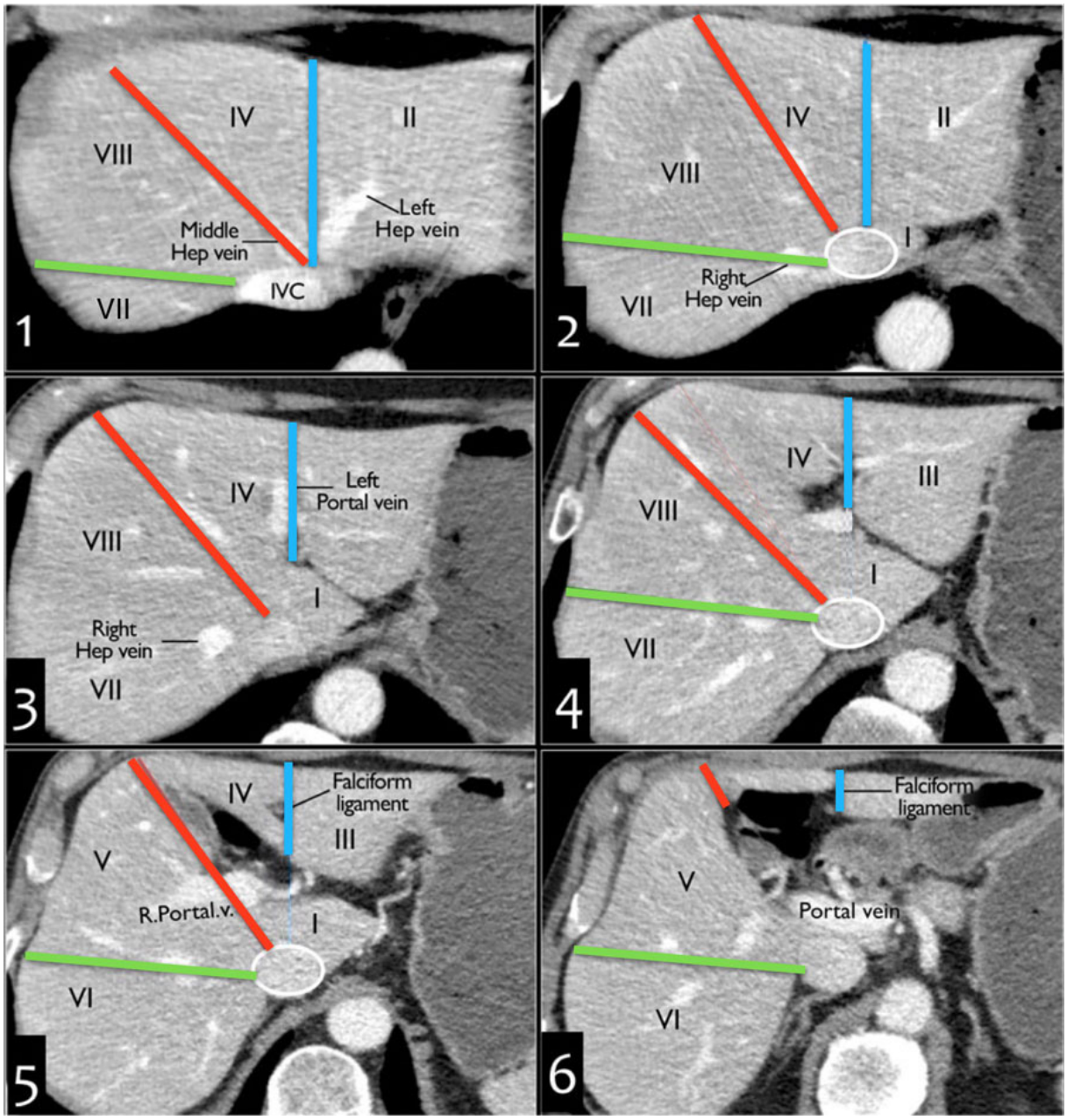

Figure 5.5: Segmentation of the liver by identification of vascular structures. IVC: inferior vena cava. Green line: right hepatic vein, separates the right lobe into segments V and VIII anteriorly and segments VI and VII posteriorly. Red line: middle hepatic vine, separates the liver into segments V and VIII on the right side and segment IV on the left side. Blue line: line from confluence of left and middle hepatic vein at the IVC to the falciform ligament, separates the liver into segments II and III laterally and segments IV medially [17].

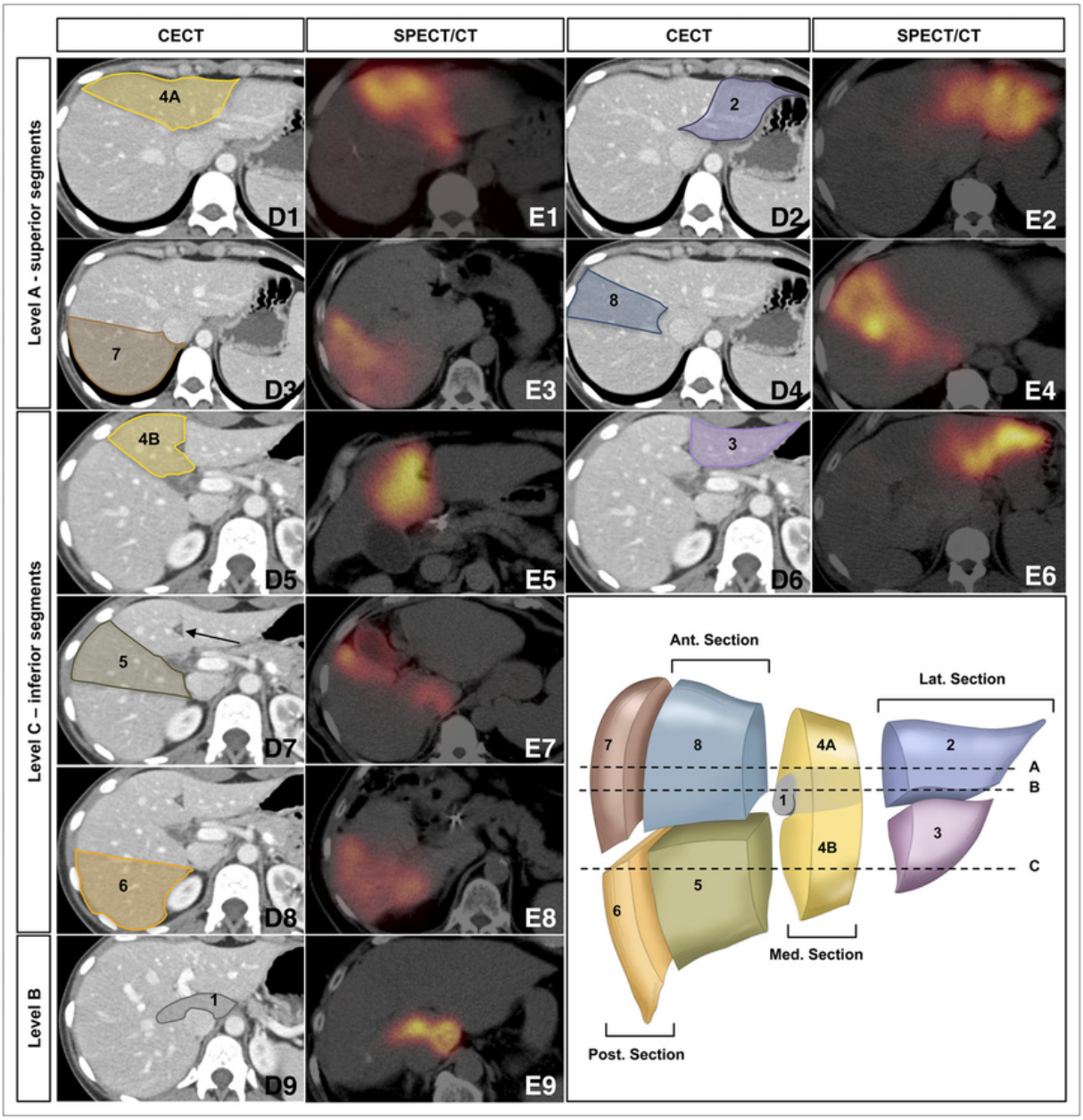

Figure 5.6: Division of the liver in eight segments according to the Couinaud classification. Depending on the axial level of the cross-sectional image, different segments can be identified [18].

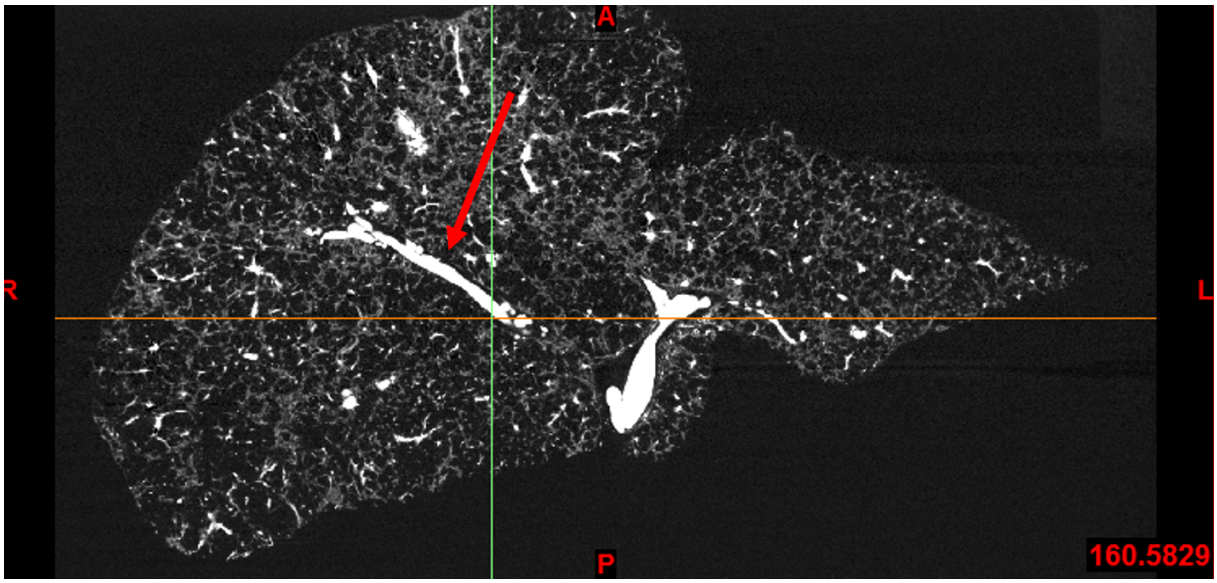

Figure 5.7: The proximal part of the middle hepatic vein, which travels in the horizontal plane, can be identified as a straight line.

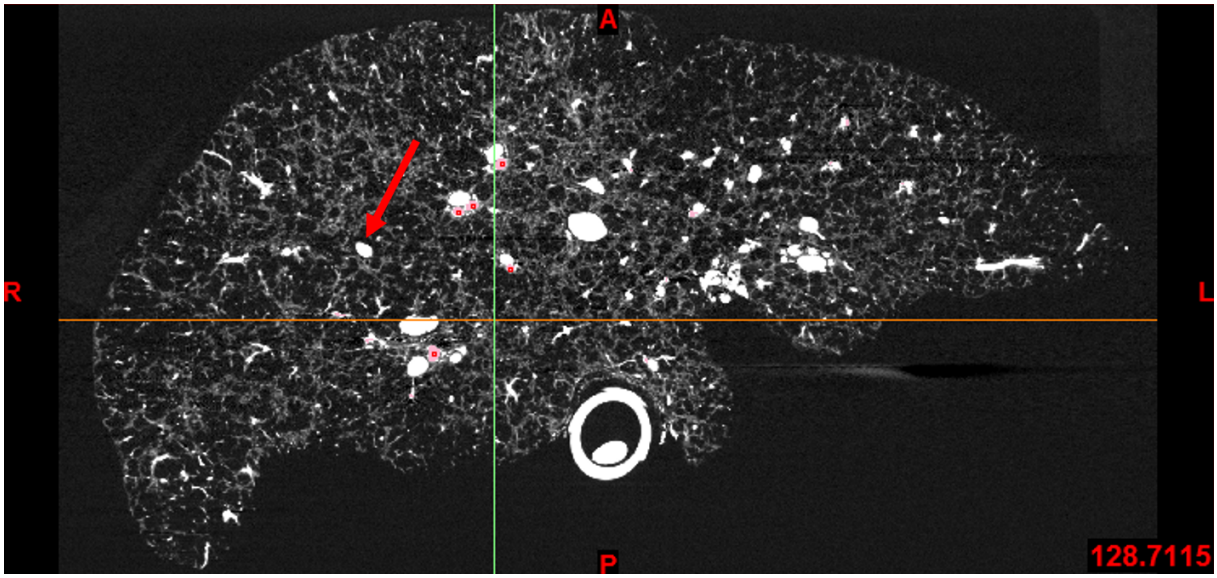

Figure 5.8: The distal part of the middle hepatic vein, which travels in the craniocaudal direction, can be identified as a circle.

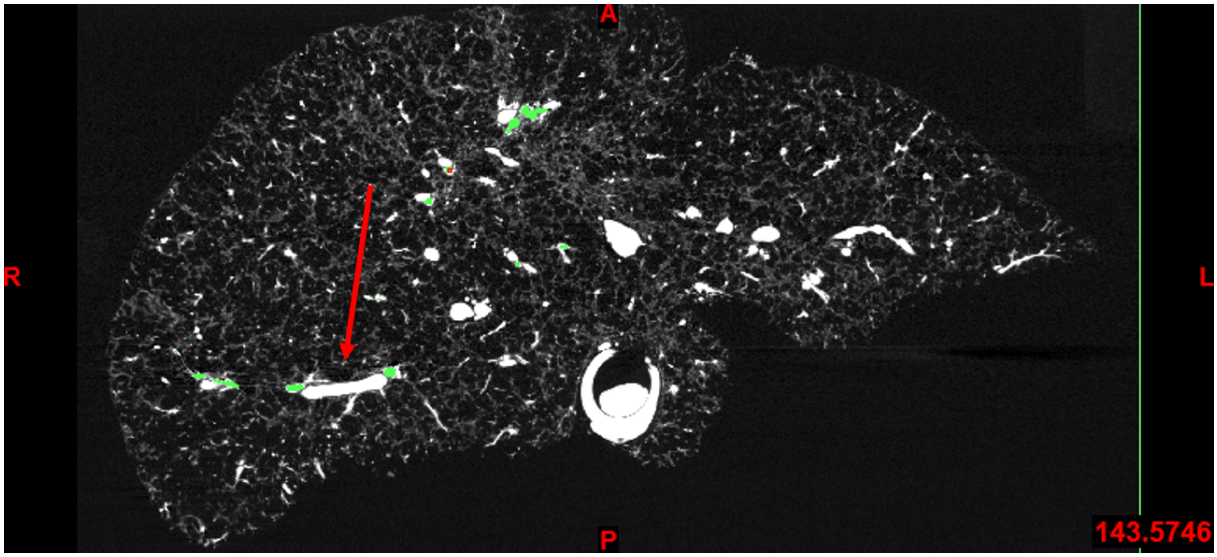

Figure 5.9: The right hepatic vein.

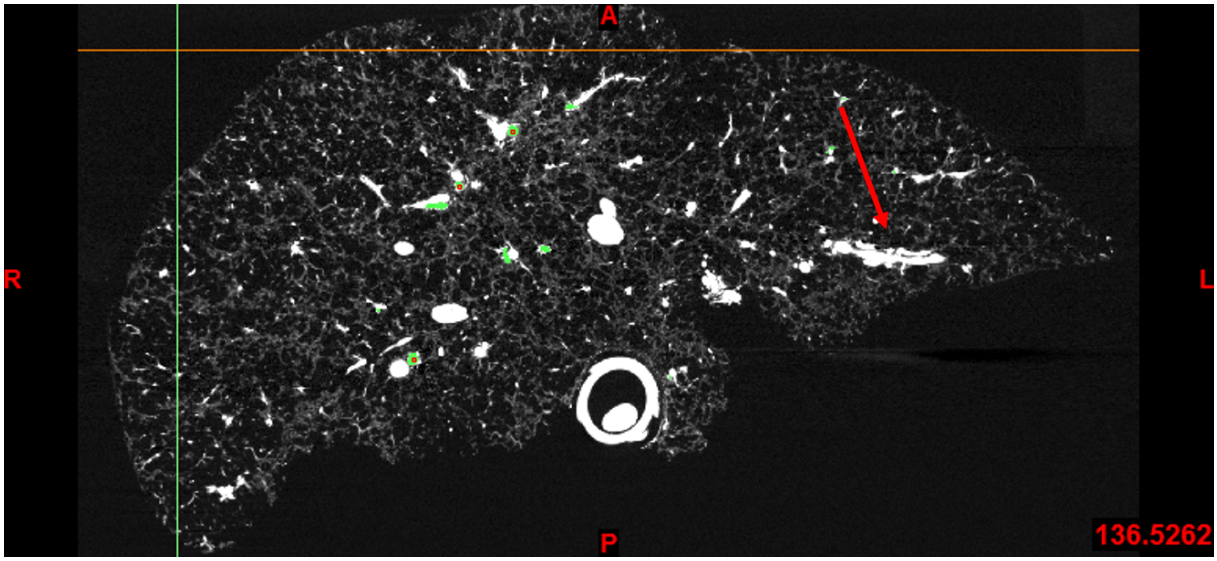

Figure 5.10: The left hepatic vein.

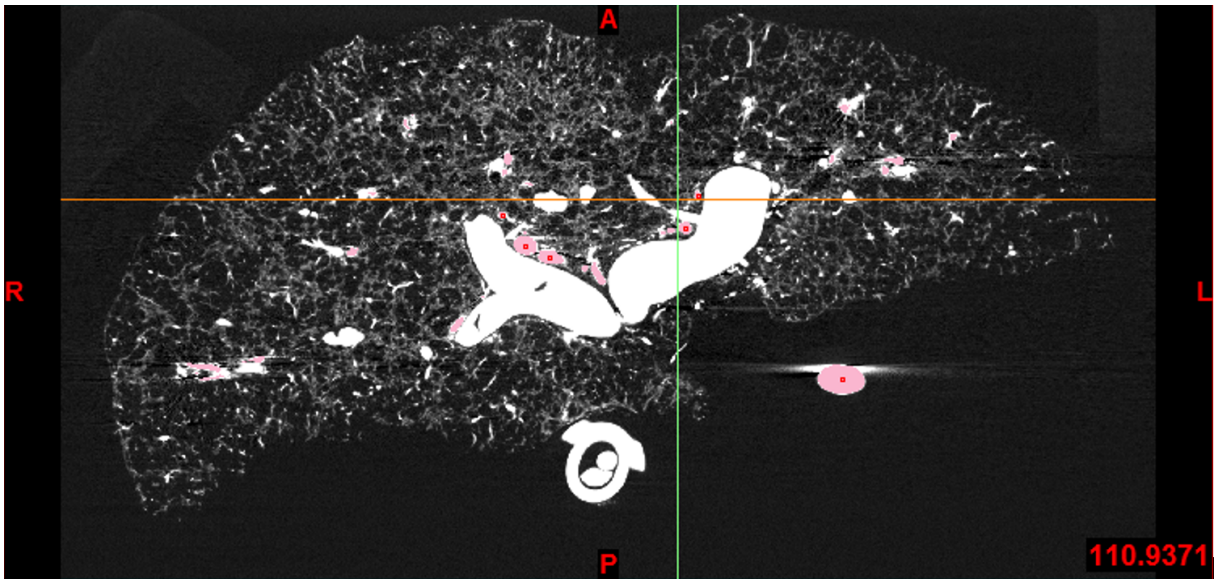

Figure 5.11: The portal vein bifurcation serves as a reference plane along the body axis. Above it lie segments II, IV(A), VII and VIII. Below it lie segments III, IV(B), V and VI.

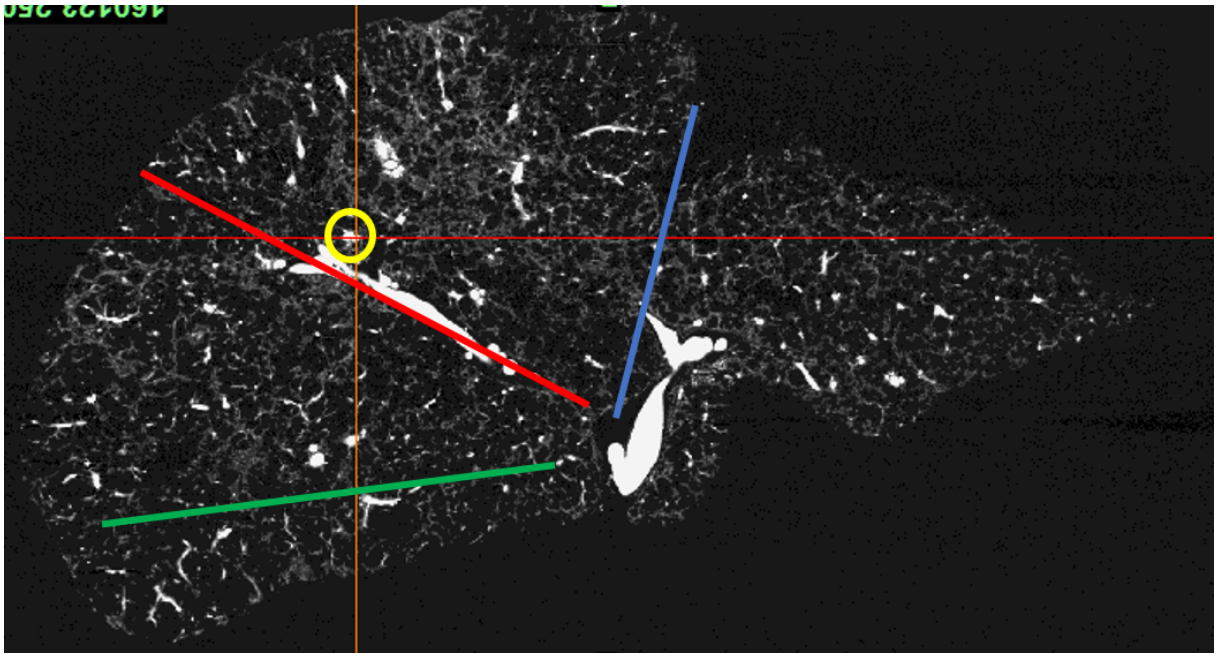

Figure 5.12: Location of Outlet 8. By drawing 3 lines, all of the segments can be identified. The green line follows the right hepatic vein, the red line follows the middle hepatic vein and the blue line follows a hypothetical line that can be drawn from the confluence of the left and middle hepatic vein at the IVC to the falciform ligament. Located in-between the red and blue lines, it can be determined that Outlet 8 is located in segment IV. No distinction is made between segments IVa and IVb.

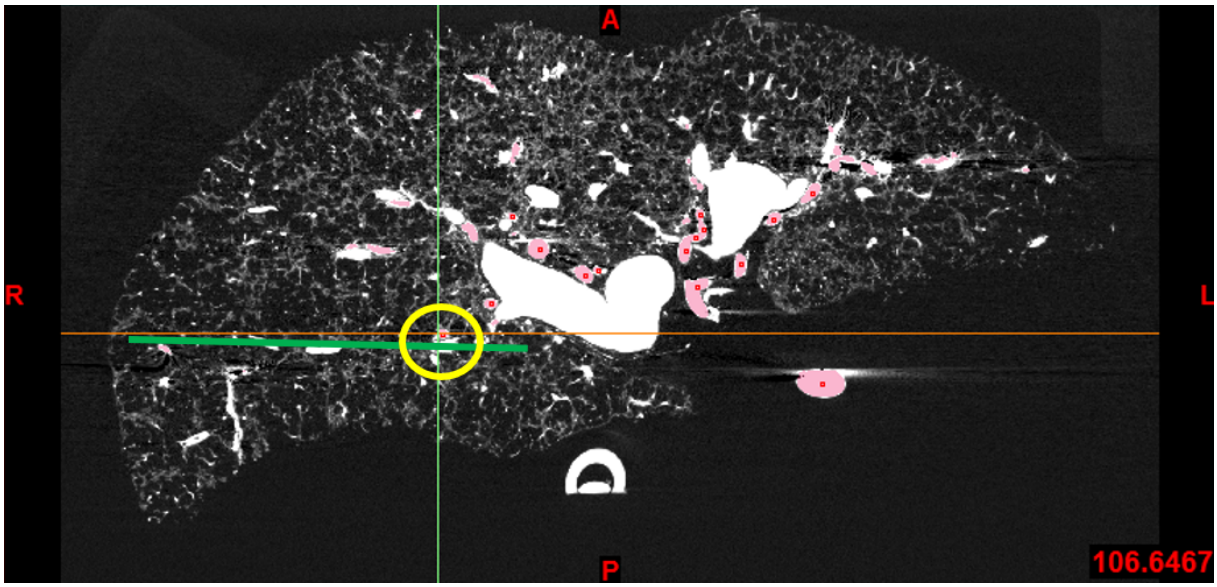

Figure 5.13: Outlet 3 (centre of the yellow circle) is located more or less on the division line that follows the right hepatic artery. To make matters worse, the axial slice is located on the plane of the bifurcation of the portal vein, which makes axial referencing very hard. As a result of this, Outlet 3 could belong to either of the following segments: V, VI, VII and VIII.

However, the issue with using the 3D model as provided by Claerebout was that most of the branches were already cut off at a specific level. This made identification significantly harder, as most of the outlets were located in zones that could be interpreted as belonging to two, three or even four different segments. This was the case for Outlet 3, as seen in Figure 5.13. To solve this problem, the author resorted to an earlier dataset, which had not yet been edited and contained longer branches, most of which also branched further into even smaller sub-branches. These sub-branches, with a higher degree of branching, were easier to allocate to different segments, and with that information it became only a case of linking the right sub-branches with the right outlets. For Outlet 3, this solution method is visualized in Figure 5.14.

5.2.3 Overview

At the start of Section 5.2.2, the goal was to obtain the degree of branching and the segmental perfusion characteristics for every outlet for this specific cirrhotic liver. Once these two crucial pieces of information were obtained, Equation 5.8 can be used to calculate the arterial flow rate through every outlet of the model. In turn, with knowledge of the size of the outlet plane, the velocity of blood flow through the outlet can be computed. These values can then used to set the outflow boundary conditions, as was the goal of implementing the arterial perfusion model. In Section 5.4, the boundary conditions for every outlet are set for several hypothetical cancer scenarios.

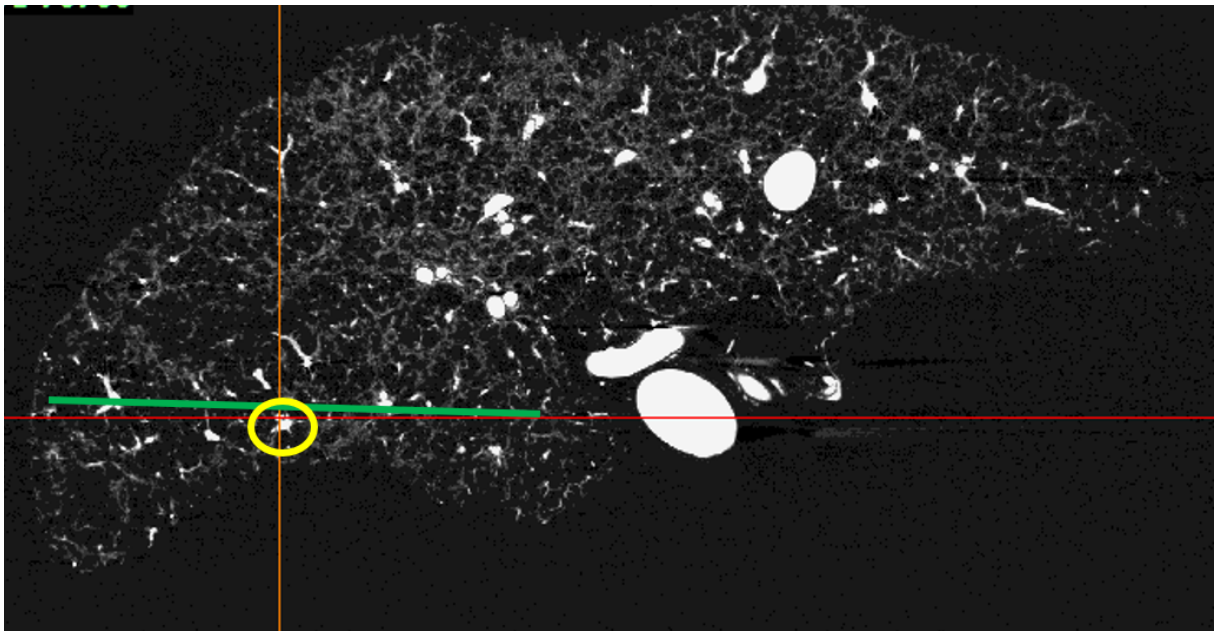

Figure 5.14: The extension of Outlet 3 (centre of the yellow circle) is located more clearly beneath the green division line. Also, it is now located on a slice that is clearly beneath the plane of bifurcation. Outlet 3 can now be classified as belonging to segment VI.

Table 5.2: Overview of the information obtained in Section 5.2.

Outlet	Diameter [mm]	Segment	Degree of branching	Effective branching factor
1	2.88	2	4	1
2	1.49	3	4	1
3	1.22	3	5	2
4	1.14	3	5	2
5	1.98	2	4	1
6	1.36	5	3	1
7	1.77	1	5	0
8	2.21	7	5	1
9	2.34	8	5	1
10	2.36	6	6	0
11	2.57	5	6	1
12	2.31	8	7	2
13	1.54	8	7	2
14	1.77	5	8	1
15	1.6	4	7	1
16	1.91	4	8	2
17	2.01	4	10	4
18	2.35	4	11	5
19	1.63	4	11	5
20	1.77	4	10	4
21	2.66	4	10	4

5.3 Fallacies of the arterial perfusion model

One of the key steps of this thesis is undoubtedly determining which segment is perfused by which outlet(s). The accuracy of the arterial perfusion model hinges entirely on the correct implementation of this information. For this reason, the amount of assumptions made by the author was limited, but it should be noted that any assumption made could have a significant impact on the overall results. Therefore, the assumptions made during the implementation, and the limitations of the model as noted by the author during the implementation process, are listed below.

- The process of computing the effective branching factors for each of the outlets and identifying which outlets fed which segments was done manually by the author. However, this made the overall process time-consuming and mistake-prone. If these steps are to be performed on a clinical day-to-day basis, then an automated recognition software should be developed in order to perform this identification process more smoothly.

- In contrary to the model developed by Aramburu et al [2], outlets feeding a similar segment are not neatly grouped together. However, it is unknown whether the angioarchitecture of the tumour-bearing liver in the study conducted by Aramburu et al developed from a cirrhotic liver or not. Since the arteries of a cirrhotic liver are generally more tortuous, this could offer a possible explanation as to why the angioarchitecture of this dataset is significantly more chaotic than the one considered in the study conducted by Aramburu et al.

- In theory, the left hepatic artery (LHA) feeds segments II, III and IV, while the left hepatic artery (RHA) feed segments I, V, VI, VII and VIII. However, in the map of the arterial network (Figure 5.3) it can be seen that the segmental arteries feeding segment IV are actually branching off the right hepatic artery instead of the left hepatic artery.

- It is possible that a computational domain-outlet branches into different sub-branches that end up feeding different segments. In this work, inspired by the model developed by Aramburu et al, it was assumed that one outlet could only feed one segment. This was done to limit the overall complexity of the model. The sub-branches were only considered when the computational domain-outlet was not clearly located in one segment, as described in Section 5.2.2.

- The perfusion parameters k_1, k_2 and $k_1^\star$ are considered constant in both space and time. In a transient simulation, the considered parameters should vary in time. In [2], they have a pulsatile nature. Moreover, the perfusion parameters may vary spatially within a segment because of the relative position of the tumours with

Table 5.3: Overview of the cancer scenarios.

Case	Burden	Location
1	None	-
2	High	Distributed
3	High	Right lobe
4	High	Left lobe
5	Moderate	Distributed
6	Moderate	Right lobe
7	Moderate	Left lobe
8	Moderate	Segment 4
9	Low	Distributed
10	Low	Right lobe
11	Low	Left lobe

respect to the normal masses. This spatial complexity was not considered as tumour nodules were assumed to be distributed homogeneously through a segment.

5.4 Case studies

The goal of this thesis is to investigate the impact of cancer burden on the particle distribution throughout the arterial network. To this end, several hypothetical scenarios were considered, each with a different distribution of tumour nodules throughout the liver. In Section 5.4.1, a general overview of these scenarios (named Cases) is given. In Sections 5.4.2 to 5.4.5, each of these scenarios are described and the outflow characteristics are calculated based on the arterial perfusion model as explained in Section 5.1. The results of the simulations will compare the different scenarios with each other and aim to give a broad view of the impact of modelling cancer burn on overall particle distribution for this patient-specific liver. These results and implications will be the focus of Chapter 6.

5.4.1 General overview

In Case 1, the healthy liver was modelled. Note that healthy in this sense means non-cancerous, since the liver considered here is still cirrhotic.

In Cases 2 to 11, three different cancer burdens were modelled. An overview of all of the different cases is given in Table 5.3.

For the cases with high cancer burden, a total cancerous volume of 1129 ml was chosen. This value is in accordance with the total tumour volume in the study conducted by Aramburu et al, which was 671 ml. However, the total healthy liver volume there was about 1500 ml, while here the total liver volume was estimated to be around 2500 ml. Therefore, the total cancerous volume was scaled with the same factor as the total

healthy liver volume to obtain a total cancer burden with a relatively similar impact on the normal tissue as in [2]. For the cases with moderate cancer burden, the total tumour volume was reduced to 50% of the original value, thus giving 565 ml in total cancerous tissue. For the cases with low cancer burden, the total tumour volume was reduced to 135 ml.

The exact locations of the tumour nodules were varied for the different scenarios. For each of the three cancer burdens, the same three scenarios were modelled: "Distributed", "Right lobe" and "Left lobe". In the scenario denoted as "Distributed", the total tumour volume was distributed equally across all eight segments, regardless of the initial size of the segment. In the scenario "Right lobe", only tumour nodules in the right lobe were considered, i.e. in segments I, IV, V, VI, VII and VIII. In the scenario "Left lobe", only tumour nodules in the left lobe were considered, i.e. in segments II and III. Furthermore, for moderate cancer burden, an extra fourth scenario was considered. In this scenario, denoted as "Segment 4", the tumour nodules were modelled in only one segment.

5.4.2 Case 1: Healthy

The healthy liver scenario served as the baseline against which all other scenarios were compared. Since no cancerous tissue was modelled, all the parameters $V_{c,s}$ were set to 0. The outflow through each outlet was calculated as described in Sections 5.1 and 5.2. The distribution of flow among the different outlets is visualized in Figure 5.15.

Interpretation of the flow distribution graph

The highest flow value is reported for Outlet 9. As is visible in Table 5.2, Outlet 9 is the only segment feeding Segment VIII with an effective branching factor of 1. This means that half of the perfusion directed towards Segment VIII flows through Outlet 9. Since Segment VIII is the liver segment with the largest healthy volume, this explains the high flow value. On the other hand, the lowest flow values are reported for Outlets 17 through 21. These outlets all feed Segment IV, with effective branching factors going up to 5, which are the largest reported in Table 5.2.

5.4.3 Case 2-4: High tumour burden

For Cases 2 to 4, a high tumour burden with a total cancerous volume of 1129 ml was modelled.

In Case 2, "Distributed", a wide distribution of tumour nodules across all eight liver segments was considered. With a total tumour volume of 1129 ml distributed equally across the segments, the volumes of cancerous tissue modelled in each segment were 141.12 ml.

In Case 3, "Right lobe", only tumours in the segments perfused by the right hepatic artery were modelled, i.e. segments I, IV, V, VI, VII and VIII. This is the same scenario

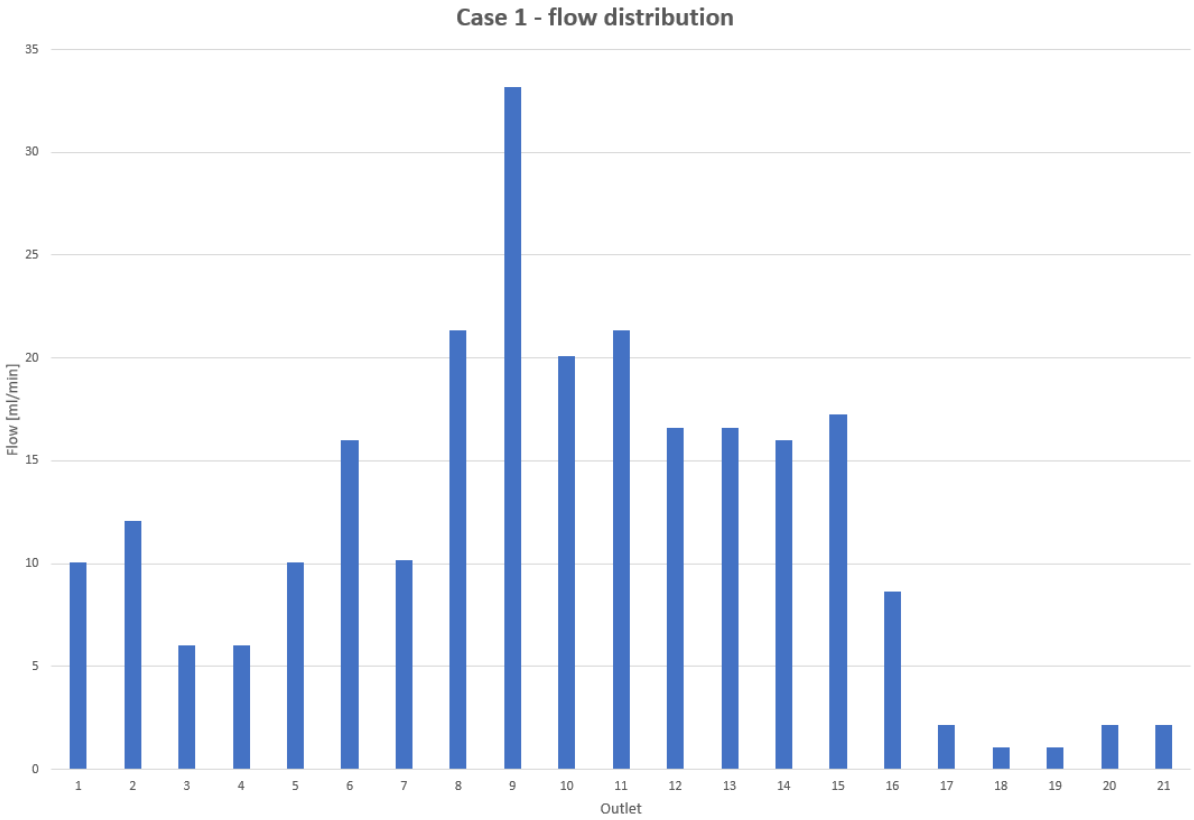

Figure 5.15: Distribution of flow among all 21 outlets.

as considered in the study conducted by Aramburu et al [2]. The tumour volumes were chosen to mimic the values chosen in [2]. However, these values had to be adapted slightly since the angioarchitecture of the specific liver considered in [2] differed from the angioarchitecture of the cirrhotic liver considered in this study. More specifically, in the liver considered here, segments I and IV are perfused by the right hepatic artery and are thus included in this case, while in [2], segments I and IV are perfused by the left hepatic artery, and are thus excluded.

In Case 4, "Left lobe", only tumours in segments perfused by the left hepatic artery were modelled, i.e. segments II and III. The total tumour volume of 1129 ml was distributed equally across both segments.

For each of these three cases, the specific volumes of cancerous tissue for each segment are reported in Table 5.4. Furthermore, the impact of the flow pattern for each of these cases is visualized Figure 5.16. In this graph, the healthy scenario (Case 1) is also visualized as a reference (blue bars).

Interpretation of the flow distribution graph

Distributed For Case 2, in which the tumour volume of 1129 ml was equally distributed across all eight segments, the flow distribution is visualized by the orange bars in Figure

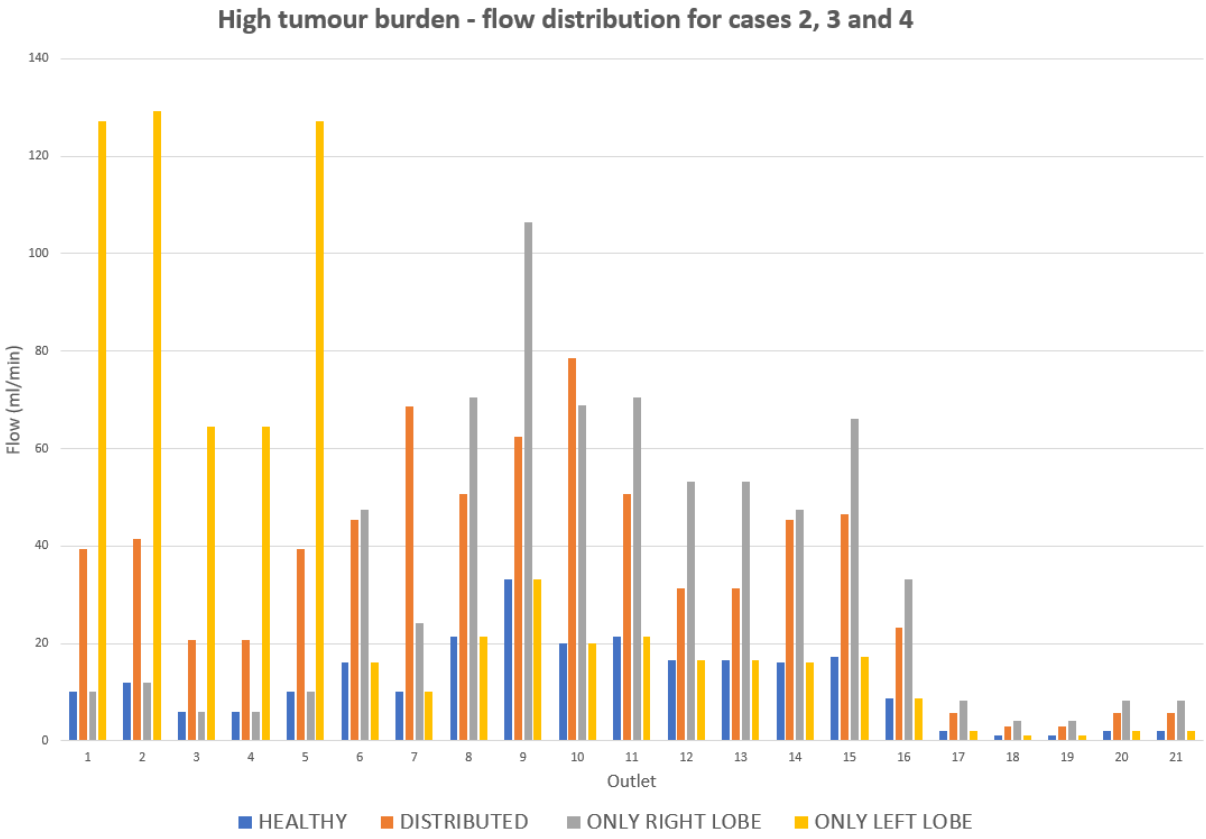

Figure 5.16: Flow distribution among the outlets for high tumour burden.

Table 5.4: Overview of the case studies - high burden.

Segment	Tumour volume [ml] Case 2	Tumour volume [ml] Case 3	Tumour volume [ml] Case 4
1	141.12	33.65	0
2	141.12	0	564.5
3	141.12	0	564.5
4	141.12	235.56	0
5	141.12	151.43	0
6	141.12	117.78	0
7	141.12	237.24	0
8	141.12	353.34	0

5.16. The largest increase in flow with respect to the healthy scenario (the blue bars in Figure 5.16) is found in Outlet 7. Furthermore, for Outlets 1 to 5 and Outlet 10 the flow values also increase sharply. Outlet 7 feeds Segment I and Outlets 1 to 5 and Outlet 10 feed Segments II and III and Segment VI, respectively. This sharp increase in flow can be explained by the fact that Segments I, II, III and VI are the four smallest segments of the liver. Because the tumour tissue of 1129 ml was divided equally among all eight segments, irrespective of their original size, the relative impact of the tumour nodules is higher in the smaller segments. In Equation 5.7, it can be seen that the ratio of tumour volume over total volume plays an important role. Since the relative volume fraction that the tumour takes up is the largest in Segments I, II, III and VI, the reported increases in flow are also the highest there.

Right lobe For Case 3, only tumours were modelled in segments I, IV, V, VI, VII and VIII. In Figure 5.16, the flow distribution is visualized by the grey bars. It can be seen that for Outlets 6 to 21, the flow increase as compared to the healthy scenario is significant. For Outlets 1 to 5, which feed the unaffected segments II and III, the absolute flow values stay the same. However, only so much significance can be attached to the absolute flow values. To understand the dynamics of flow competition occurring in these scenarios better, the fractions of total flow for each outlet, ranging from 0 to 1, are visualized in Figure 5.17. Note that the flow fractions denoted here are relative *increases* compared to the healthy scenario - thus, 0% meaning that the flow fraction is exactly the same as in the healthy scenario, 100% meaning that the flow fractions have doubled and a negative value implying that the flow fraction has decreased. By inspecting this graph, it can be stated that the flow fractions in Outlets 1 to 5 decrease and the flow fractions for Outlet 6 and Outlets 8 to 21 increase, even though, from an absolute point of view, these flow values are all the same or higher than the healthy scenario. Perhaps unexpectedly, the relative flow fraction for Outlet 7 decreases slightly compared to the healthy scenario. This is most probably due to the fact that Outlet 7 feeds Segment I, in which only a small nodule of 33.65 ml was modelled in this specific case. Due to the phenomenon of flow competition, the sharpest increases in flow fraction favour the segments that harbour the largest tumours. Therefore, the flow fraction in Segment I most probably decreases slightly because the cancer burden is much lower there than compared to other segments.

Left lobe For Case 4, only tumours were modelled in segments II and III. In Figure 5.16, the flow distribution is visualized by the yellow bars. In Figure 5.17, the relative flow fraction increase as compared to the healthy scenario is depicted (again in yellow). In this graph, it can be seen that the relative flow fractions of Outlets 6 to 21 decrease in favour of a large increase in relative flow fraction for Outlets 1 to 5, where the local cancer burden is very high.

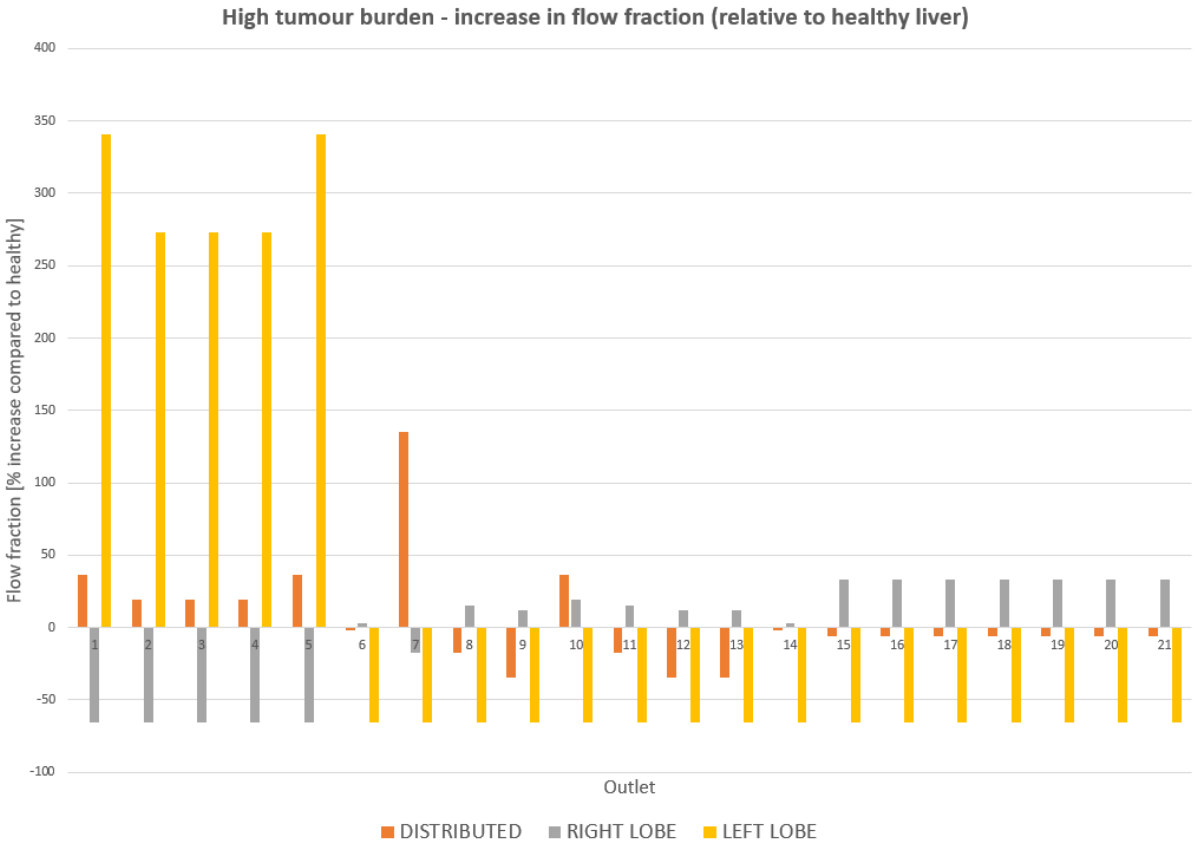

Figure 5.17: Increase in flow fraction, compared relatively to the healthy scenario, for high tumour burden.

Table 5.5: Overview of the case studies - moderate burden.

Segment	Tumour volume Case 5	Tumour volume Case 6	Tumour volume Case 7
1	70.56	16.83	0
2	70.56	0	282.25
3	70.56	0	282.25
4	70.56	117.78	0
5	70.56	75.71	0
6	70.56	58.89	0
7	70.56	118.62	0
8	70.56	176.67	0

5.4.4 Case 5-8: Moderate tumour burden

For the cases with moderate tumour burden, the same methodology was adapted as for the ones with high cancer burden.

For Case 5, "Distributed", the total tumour volume of 564.5 ml was distributed equally across all eight segments. For Case 6, "Right lobe", the volumes of the cancerous tissue for each segment perfused by the right hepatic artery were scaled with 50% as compared to the values for Case 3 reported in Table 5.4. For Case 7, the total tumour volume was split equally across the segments perfused by the left hepatic artery, i.e. segments II and III.

The volumes of cancerous tissue for each segment in each of the three cases are given in Table 5.5. The flow distribution for these three cases and the healthy case are visualized in Figure 5.18.

For Case 8, the total tumour volume of 564.5 ml was modelled in Segment IV alone. Since the flow values reported here are considerably higher, the flow distribution is plotted separately in Figure 5.20.

Interpretation of the flow distribution graph

Distributed For Case 5, the flow distribution is visualized in Figure 5.18 by the orange bars. Just as in Case 2, the largest increases in flow values as compared to the healthy scenario are reported in Outlets 1 to 6, Outlet 7 and Outlet 10. This is because these outlets feed Segments I, II, III and VI, which are the smallest segments and thus the ones that are most affected - volume-wise - by the tumour nodule of 70.56 ml. The calculation of the relative fraction the tumour tissue takes up in a certain segment is an important part of the calculations in 5.7 and explain these large increase for these reported segments.

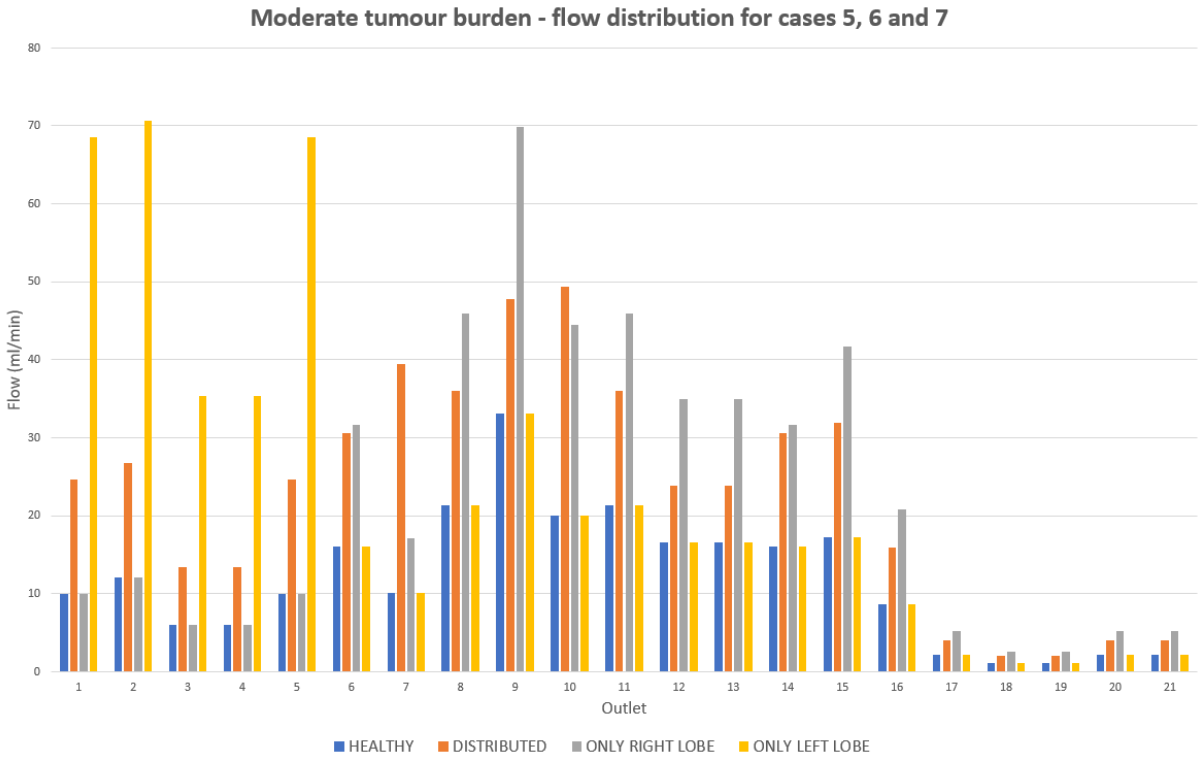

Figure 5.18: Flow distribution among the outlets for moderate tumour burden.

Right lobe For Case 6, in which only tumours were modelled in Segments I, IV, V, VI, VII and VIII, the same conclusions as reported for Case 4 still stand. The flow distribution is visualized in Figure 5.18 by the grey bars, while the relative flow fraction increases compared to the healthy scenario are visualized in Figure 5.19 (also in grey). While the absolute flow values in Figure 5.18 either stay the same or increase for all segments, it can be seen in Figure 5.19 that the relative flow fractions of Outlets 1 to 5 (which are fed by the left hepatic artery) decrease and the relative flow fraction of Outlets 6 and Outlet 8 to 21 increase to match the increase in hepatic arterial blood supply demanded by the tumour tissue. Again, the relative flow fraction in Outlet 7 decreases, most probably due to the relatively low local cancer burden in Segment I.

Left lobe For Case 7, in which only tumours were modelled in Segments II and III, the same conclusions that were reported for Case 5 still stand. The flow distribution is visualized in Figure 5.18 by the yellow bars, the flow fraction increases as compared to the healthy scenario are visualized in Figure 5.19 (also in yellow). In short, the relative flow fraction of Outlets 6 to 21 decrease in favour of the increase in relative flow fraction of Outlets 1 to 5, which feed the affected Segments II and III.

Only Segment 4 For moderate tumour burden, an extra case was modelled in which all the cancerous tissue is concentrated in only one segment, Segment 4. The flow distribution graph is visualized in Figure 5.20. As can be seen, the absolute flow values are the largest

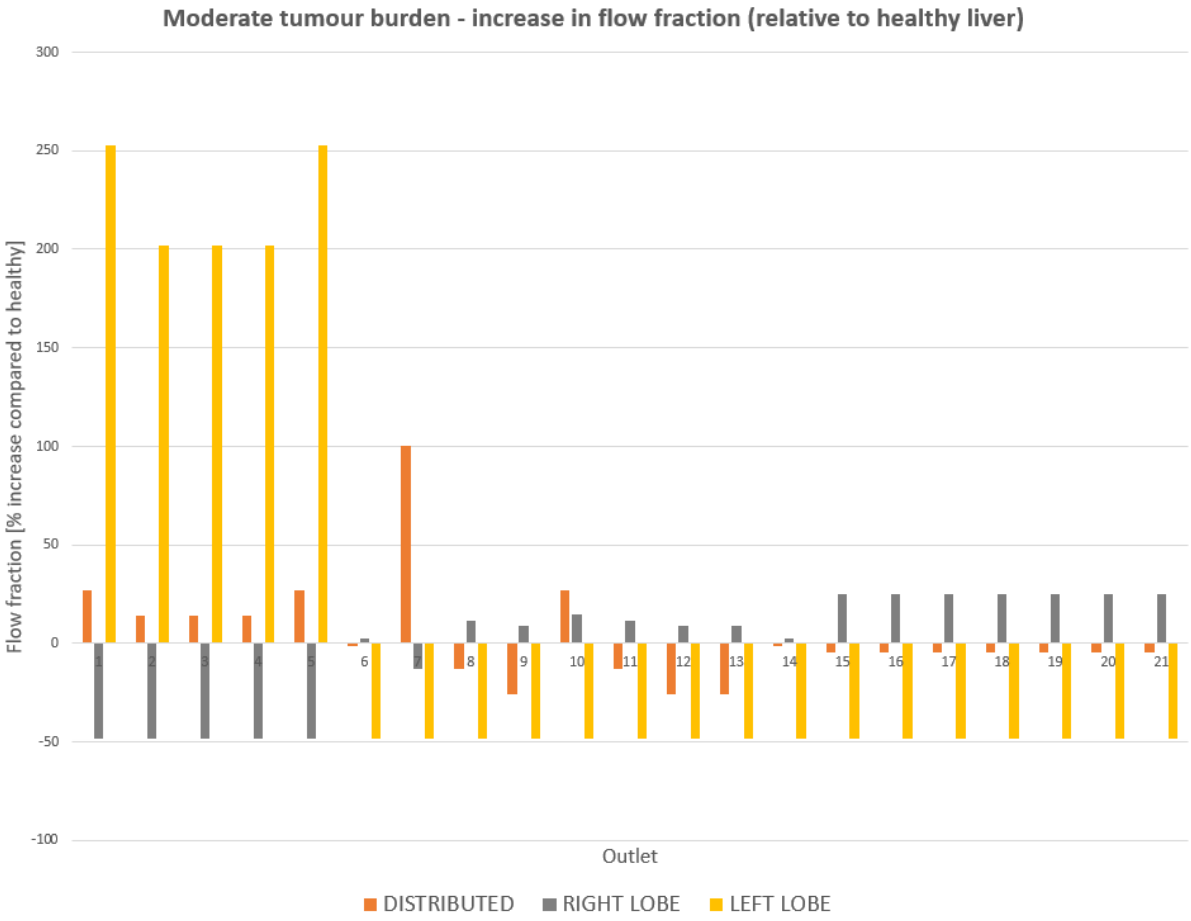

Figure 5.19: Increase in flow fraction, compared relatively to the healthy scenario, for moderate tumour burden.

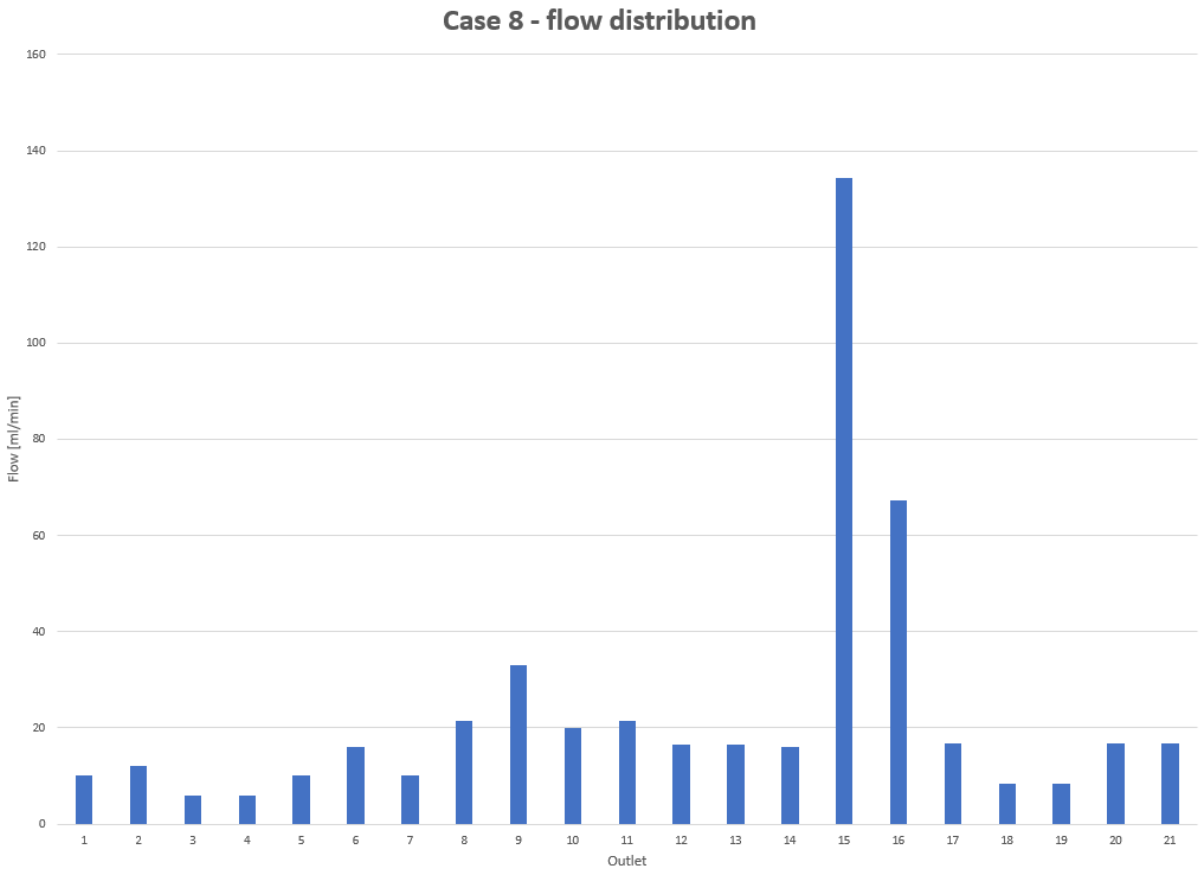

Figure 5.20: Flow distribution among the outlets for moderate tumour burden. Tumour nodules are restricted to Segment 4.

Table 5.6: Overview of the case studies - low burden.

Segment	Tumour volume Case 9	Tumour volume Case 10	Tumour volume Case 11
1	16.875	4.02	0
2	16.875	0	67.5
3	16.875	0	67.5
4	16.875	28.17	0
5	16.875	18.11	0
6	16.875	14.08	0
7	16.875	28.37	0
8	16.875	42.25	0

for Outlets 15 and 16, which feed Segment 4 with an effective branching factor of 1 and 2 respectively. While the absolute flow values for Outlets 18 to 21 are more in the range of the other outlets, this is a notable result since in the healthy scenario the flow values of Outlets 18 to 21 were an order of magnitude smaller than the other outlets. This can be seen in Figure 5.15. Overall, the flow through Outlets 15 to 21, which are the outlets perfusing Segment IV, increase over tenfold.

5.4.5 Case 9-11: Low tumour burden

For the cases with moderate tumour burden, the same methodology was adapted as for the cases with high and moderate cancer burden.

For Case 9, the total tumour volume of 135 ml was distributed equally across all eight segments. For Case 10, the volumes of the cancerous tissue for each segment perfused by the right hepatic artery were scaled with 12% with respect to the values for Case 3 reported in Table 5.4. This was done to account for the lower overall cancer burden. For Case 11, the total tumour volume was split equally across the two segments perfused by the left hepatic artery, i.e. segments II and III.

The volumes of cancerous tissue for each segment in each of the three cases are given in Table 5.6. The flow distribution for these three cases and the healthy case are visualized in Figure 5.21. The relative flow fraction increases for all three cases as compared to the healthy scenario are visualized in Figure 5.22.

Interpretation of the flow distribution graph

Distributed Just as in Cases 2 and 5, the highest increases in absolute flow values are reported for Outlets 1 to 6, Outlet 7 and Outlet 10 because of the relatively high local tumour burden in these segments. This can be seen in the yellow bars of both Figure 5.21 and Figure 5.22. However, it should also be noted that in these figures it is clear that the increase in flow is much lower than for Cases 2 and 5, where the overall tumour burden

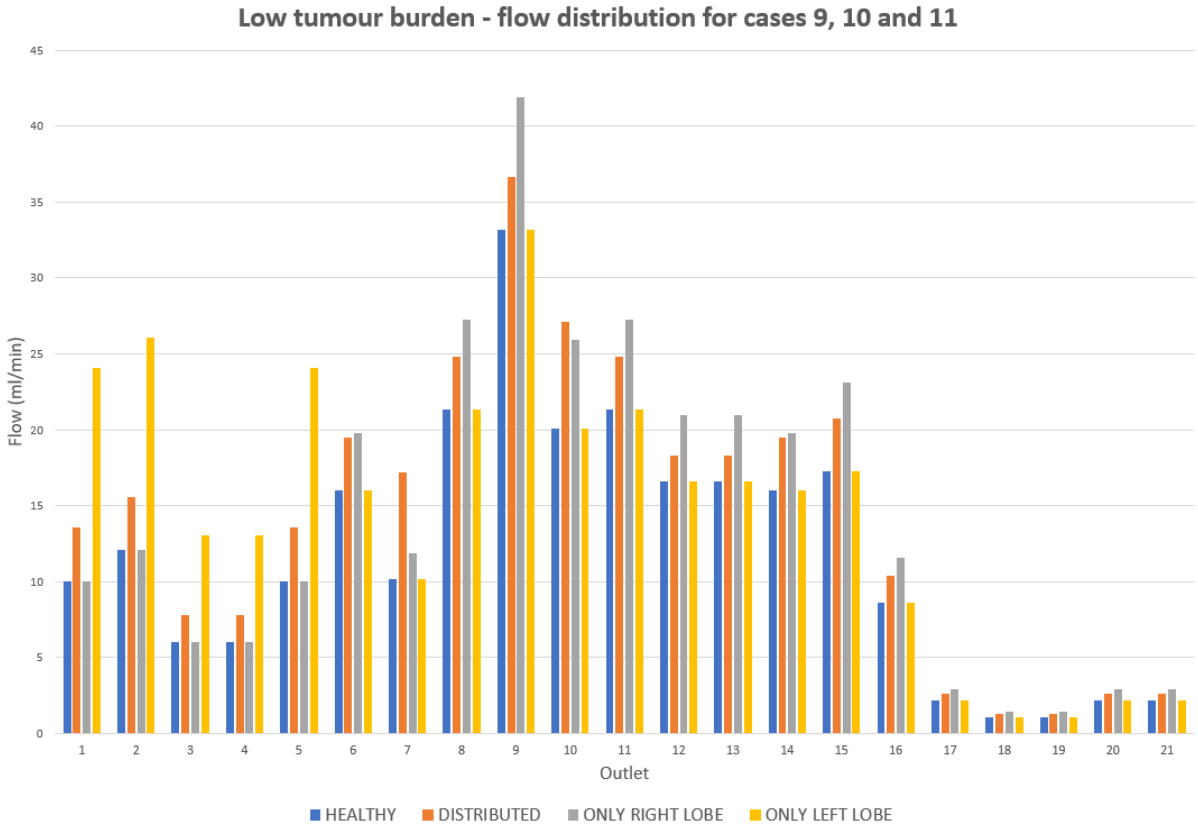

Figure 5.21: Flow distribution among the outlets for low tumour burden.

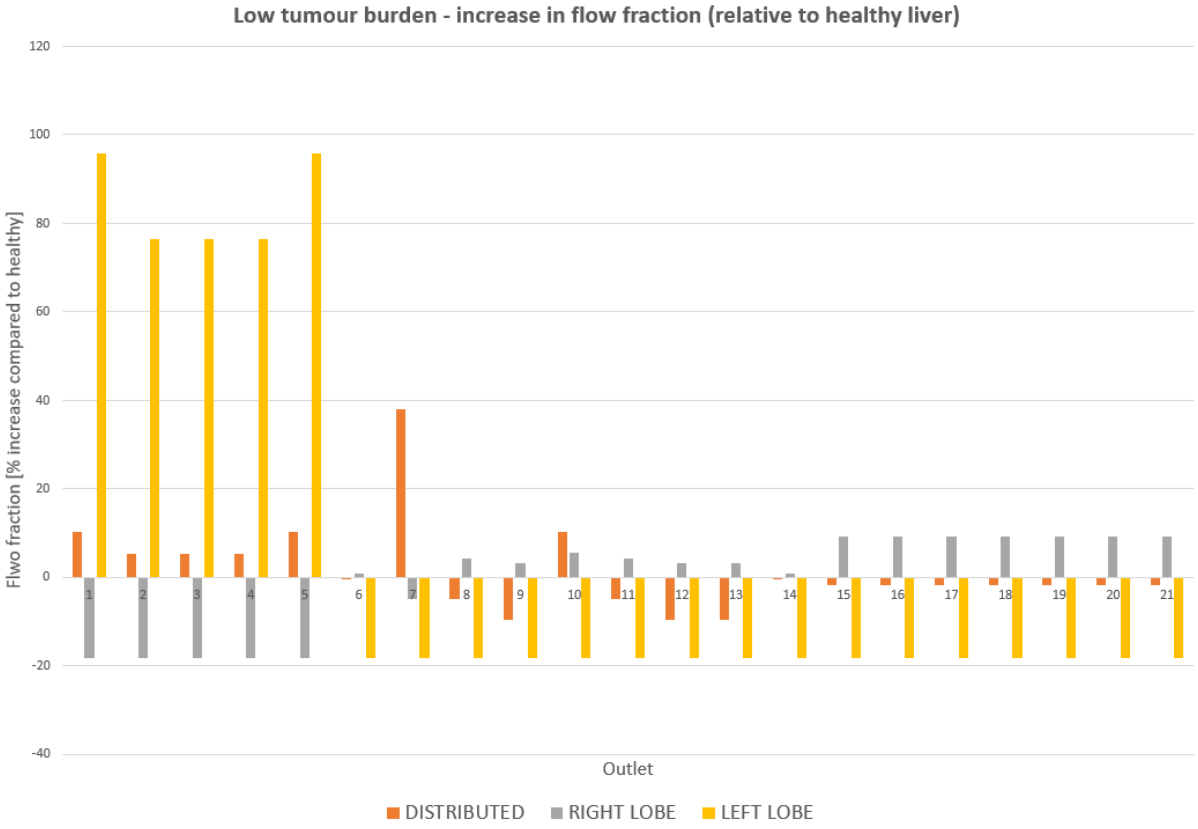

Figure 5.22: Increase in flow fraction, compared relatively to the healthy scenario, for low tumour burden.

was much higher. More notes on the impact of cancer burden on the absolute flow values will be made in Section 5.4.6.

Right lobe For Case 10, the conclusions made for Case 3 and 6 still stand. By inspection of the grey bars in Figure 5.21, it can be concluded that the flow fractions in Outlets 1 to 5 decrease and the flow fractions in Outlet 6 to 21 increase to match the higher metabolic demand of the tumour tissue at this side of the hepatic arterial tree.

Left lobe For Case 11, the conclusions drawn for Case 4 and 7 still stand. The increase in relative flow fraction for Outlets 1 to 5 (visualized by the yellow bars in Figure 5.22) is sharp, to match the higher blood supply demand at the left lobe of the tumour, but noticeably less sharp than for the previous cancer burdens.

To summarize, it can be stated that varying the degree of cancer burden impacts both the distribution of flow among the outlets for different scenarios as well as the absolute flow values. More comments on the absolute flow values are made in Sections 5.4.6 and 5.5.

5.4.6 The impact of cancer burden on absolute flow values

The total liver blood flow is divided between supply through the proper hepatic artery on the one hand and the portal venous supply on the other hand. The Doppler Perfusion Index (DPI) measures the fraction of blood supply through the hepatic arterial system over the total blood flow rate (through the hepatic arteries and the portal veins). It is reported in literature that the DPI increases for patients with colorectal liver metastases [2, 47]. The exact factor by which the DPI increases, differs from patient to patient and depends on the type and size of the tumours. It is expected that, for high cancer burden, the DPI increases more than for low cancer burden. This effect is visualized in Figure 5.23. Here, the flow distribution is given for the same hypothetical cancer scenario (only tumour nodules in segments perfused by the right lobe), but for the three varying degrees of cancer burden. It can be seen that the maximal reported flow value in the hepatic arteries occurs for high cancer burden, namely 106.47 ml/min. For moderate cancer burden, the maximal reported flow value is 69.81 ml/min. For low cancer burden, the maximal reported flow is 41.92 ml/min. The reference value for a healthy liver is 33.15 ml/min. These findings support the conclusions already drawn in literature regarding the increase of DPI for patients with hepatic metastatic cancers [2, 47].

5.4.7 Computing outflow BC from flow distribution

Throughout Sections 5.2 and 5.4, the flow distribution for the 21 outlets in the healthy scenario and the hypothetical tumour-bearing scenarios for the cirrhotic liver considered

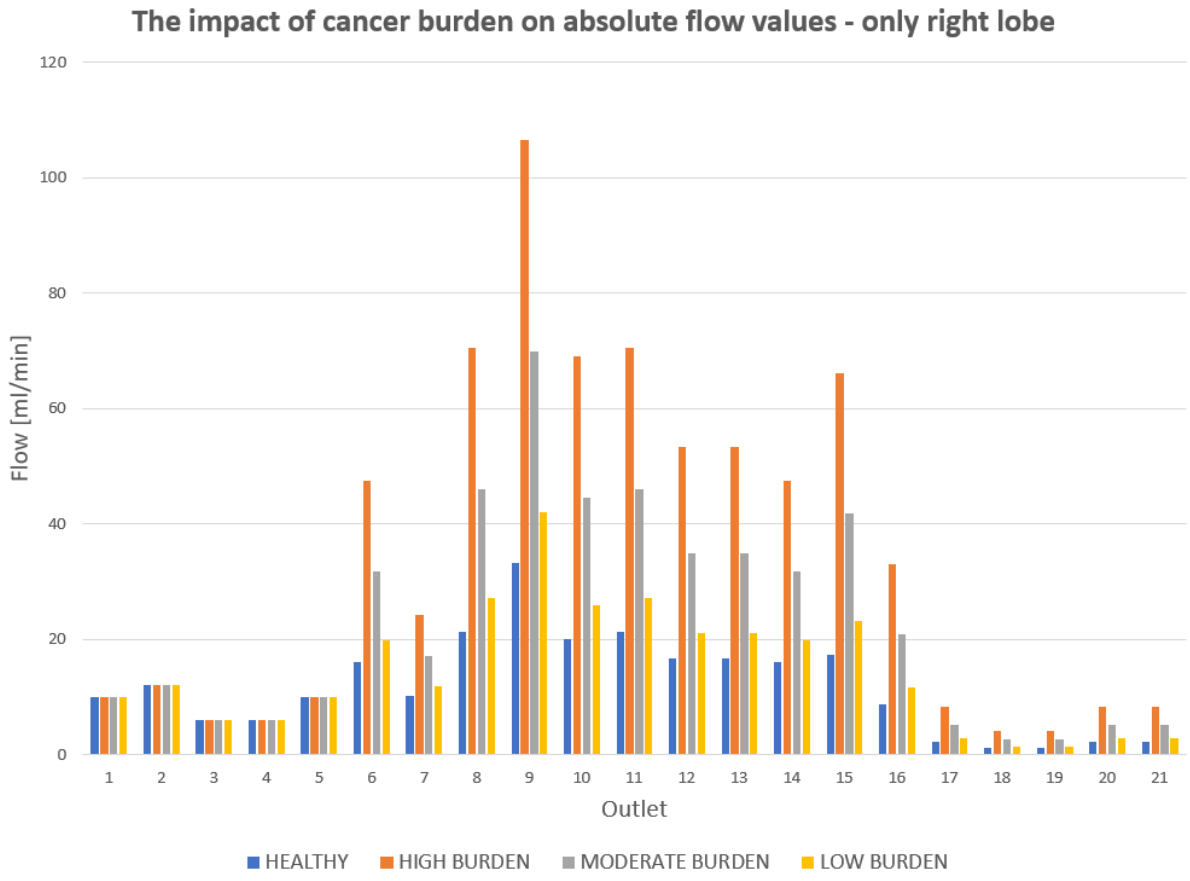

Figure 5.23: The impact of cancer burden on absolute flow values.

in this thesis were determined. The diameters of every outlet were calculated using the tool *Best Fit Diameter*. With knowledge of the volumetric flow rate through each of the outlets and the dimensions of the outlet planes, the velocities at each of the outlets were calculated using the following formula:

$$v_m = \frac{q_{m,s}}{A_m} \tag{5.10}$$

In this equation, the index m denotes a certain outlet (ranging from 1 to 21), $q_{m,s}$ is the flow through outlet m and A_m is the area of outlet m. Note that, in $q_{m,s}$, the index s denotes the segment which is perfused by outlet m and could strictly be dropped since it was assumed that one outlet only perfuses one segment.

At this point, the outflow boundary conditions have been fully determined. This was the goal of the arterial perfusion model.

5.4.8 Side-to-side comparison with Murray's law

As this thesis proposes an alternative boundary condition to Murray's law, it makes sense to compare the two boundary conditions side-to-side. The discussion here will be limited to the flow distribution.

In Figure 5.24, the flow distribution as calculated with Murray's law is compared side-to-side with the flow distribution of Case 1 (the healthy, non-cancerous scenario) as calculated with the arterial perfusion model. As is obvious from Figure 5.24, the two flow distributions look largely different. The largest discrepancies are found in Outlets 1, 6, 9, 15 and 17 to 21 (all above 5%). The flow fractions in Outlets 17 to 21 are notably larger for Murray's law than they are for the arterial perfusion model. Since such large differences are reported for all outlets perfusing Segment 4 except for Outlet 16, Section 6.1.3 will focus more on the particle distribution in this segment. Furthermore, it was noted in Section 5.4 that the flow in Outlet 9 was the highest of all outlets. This conclusion can clearly not be made for Murray's law. The smallest differences between the two boundary conditions are reported in Outlets 3, 4, 10, 11 and 16 (all below 1%).

The differences between Murray's law and the arterial perfusion model will be further elaborated upon in Chapter 6. There, the particle distributions will be compared. Special attention will be paid to Segment 4.

5.5 Inflow boundary condition

Once the outflow boundary conditions were fully determined, the inflow boundary condition was calculated based on a simple application of the principle of conversation of mass. Since Equation 5.7 gives the volumetric flow rate for each segment, the volumetric flow

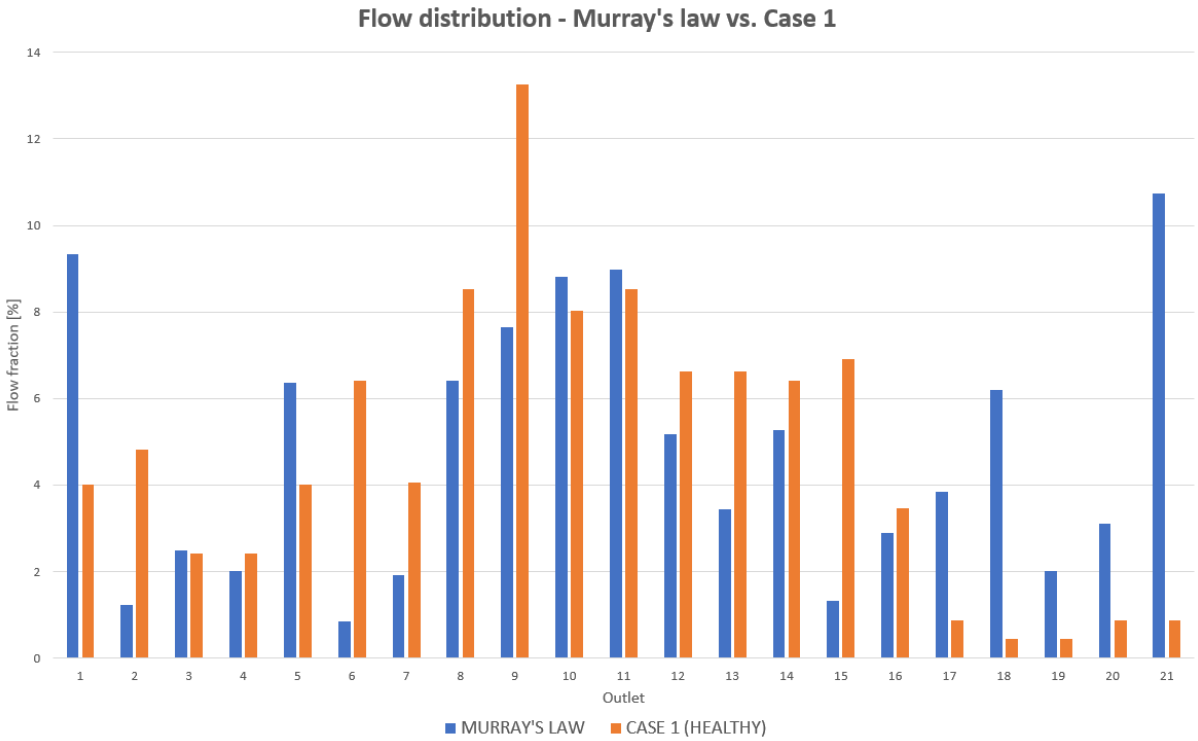

Figure 5.24: The impact of cancer burden on absolute flow values.

Table 5.7: Overview of the inflow boundary conditions.

Case	Cancer burden	Inflow [ml/min]	Inflow velocity [mm/s]
1	None	250	97.67
2, 3, 4	High	718.53	280.72
5, 6, 7, 8	Moderate	484.27	189.2
9, 10, 11	Low	306.03	119.56

rate through the inlet is given by summarizing these flow rates over every segment:

$$q_{inlet} = \sum_{s=S1}^{S8} (K_{h,s} + K_{c,s}) q_{0,s} \tag{5.11}$$

Then, as already mentioned in Section 4.1.6 , the velocity of blood at the inlet plane can be calculated knowing the flow rate through the inlet and the dimensions of the inlet plane. The relationship between flow and velocity was already stressed in Equation 4.14.

It should be mentioned that the higher the cancer burden, the higher the metabolic demands of the tumour tissue are, and thus the higher the volumetric flow rate through the inlet will be. This was already noted in Section 5.4.6. Table 5.7 gives an overview of the four inflow boundary conditions for the four different cancer burdens considered in the simulations.

5.6 Simulations

The computation of the new boundary conditions for each hypothetical cancer scenario is the focus of Chapter 5. Once the boundary conditions were fully determined, the simulations were run in ANSYS Fluent. In total, fourteen steady-state simulations were run. Specifically, all eleven hypothetical cancer scenarios (including a healthy case) were simulated for the SIR-Spheres. The properties of these particles were given in Table 4.1. Cases 4 and 9 were repeated for the Thera-Spheres, which are a different type of particle that are also typically used in TARE procedures. Finally, a final simulation was run using Murray's law as the boundary condition. This allowed to compare the results of the arterial perfusion model with the results obtained for Murray's law. An overview of the simulation specifics is given in Table 5.8.

Table 5.8: Overview of injection characteristics for the computer simulations.

Simulation number	**Particle type**	**Injection velocity [mm/s]**	**Outlet BC**
1	SIR	97.67	Case 1
2	SIR	280.72	Case 2
3	SIR	280.72	Case 3
4	SIR	280.72	Case 4
5	SIR	189.20	Case 5
6	SIR	189.20	Case 6
7	SIR	189.20	Case 7
8	SIR	189.20	Case 8
9	SIR	119.56	Case 9
10	SIR	119.56	Case 10
11	SIR	119.56	Case 11
12	Thera	280.72	Case 4
13	Thera	119.56	Case 8
14	SIR	280.72	Murray's Law

Part III

Results and Discussion

Chapter 6

Evaluation

In this chapter, the results for the fourteen simulations are given. In Section 6.1.1, the Particle Release Maps (PRM) for different cancer scenarios are compared with each other. They are also compared with the PRM generated with Murray's law to highlight the difference between the two types of boundary conditions. In Section 6.1.2, the distribution of Thera-Spheres is compared with the distribution of SIR-Spheres for two specific cancer scenarios. Finally, in Section 6.1.3, the focus is shifted to Segment 4. Segment 4 is irrigated by arteries that were very tortuous, which can make targeted particle delivery rather difficult. Therefore, in scenarios in which tumour nodules are spread throughout Segment 4, it makes sense to evaluate the fraction of particles that are able to reach the outlets that perfuse this segment.

6.1 Results

The particle tracks were exported from ANSYS Fluent to CFD-Post. CFD-Post is an especially useful tool for visualizing the particle tracks for a set selection of particles. An example of 75 particle tracks for Mesh 3 in the Healthy scenario is given in Figure 6.1. From this visualization, it can be seen that certain outlets are very hard to reach. This will be discussed further in Section 6.1.3.

The information regarding the particle tracks was then further processed using Matlab. For each case, the PRMs were generated. These maps are convenient visual aids that visualize the fate of each particle at the injection plane, as already described in Section 2.3.

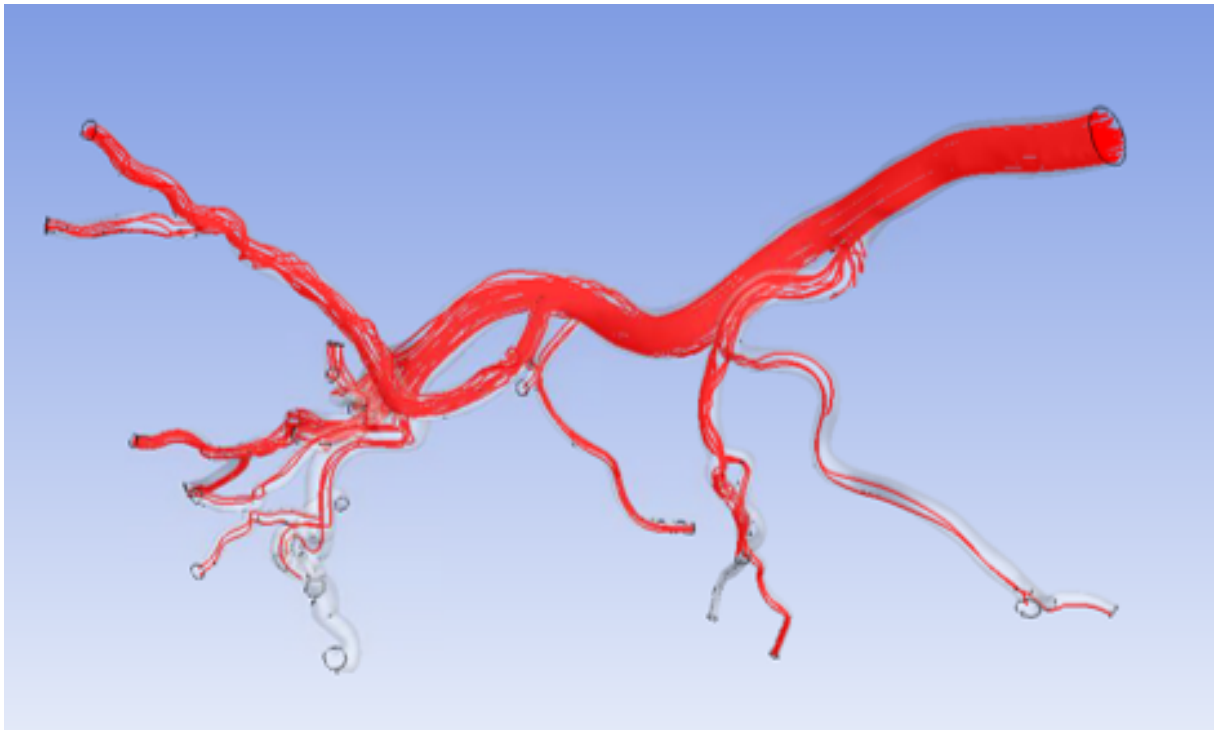

Figure 6.1: Particle track visualization for Healthy scenario.

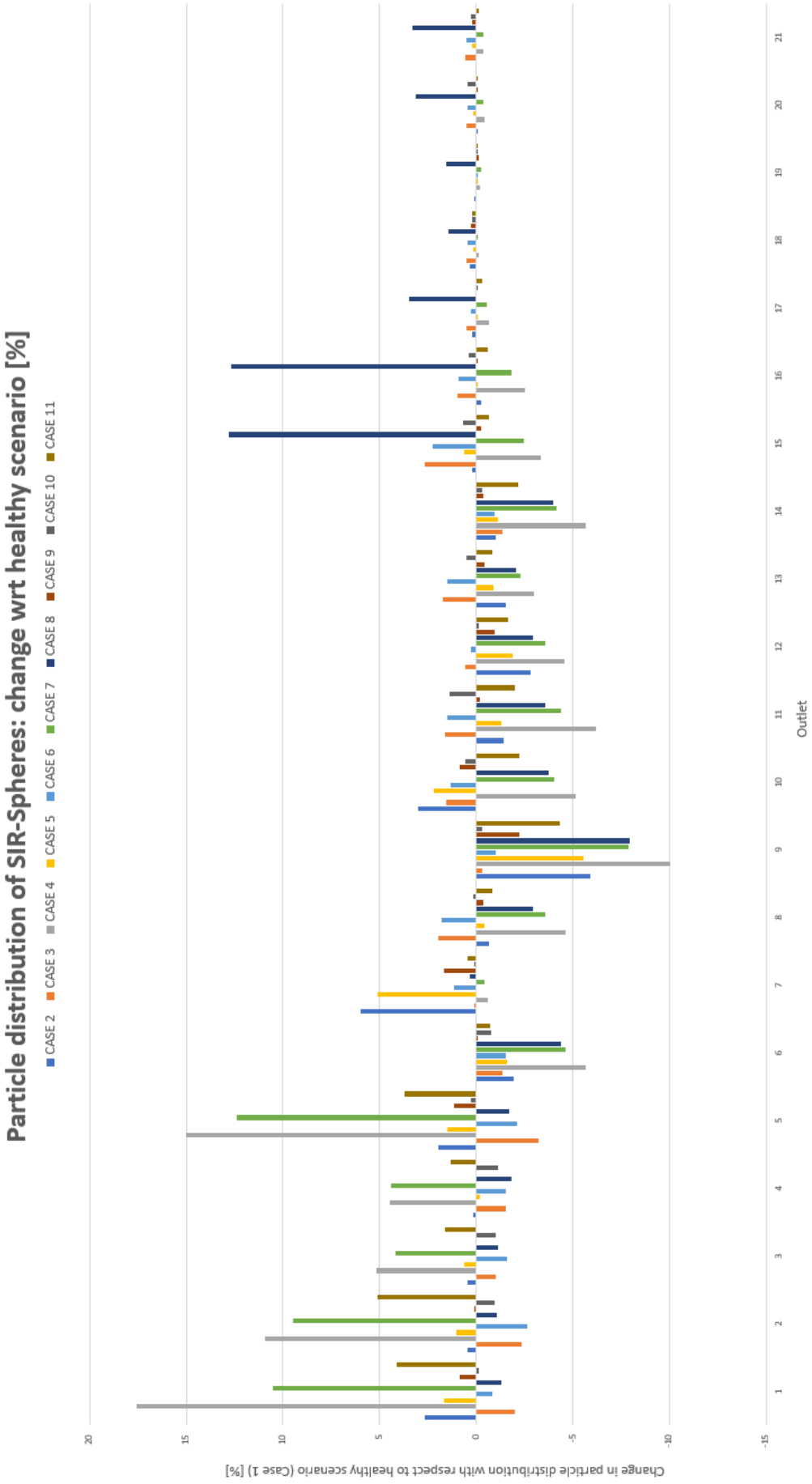

Figure 6.2: Change in SIR-Sphere distribution [%] with respect to the Healthy scenario (Case 1).

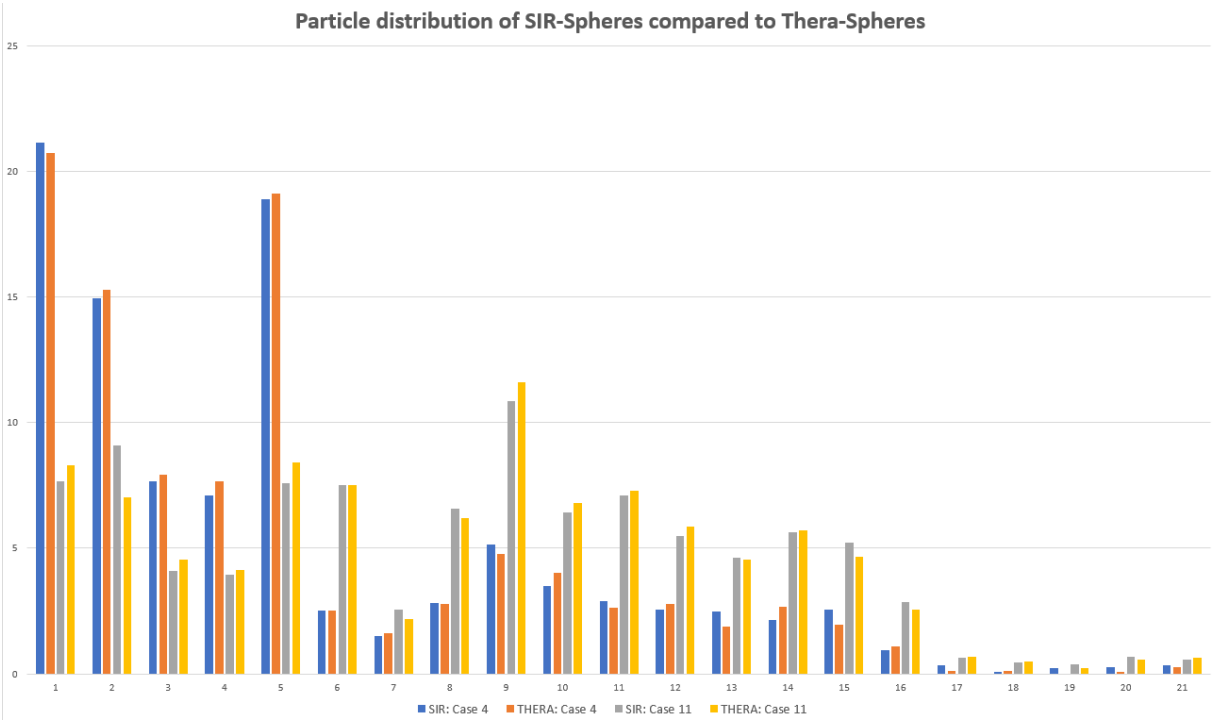

Figure 6.3: Distribution of Thera-Spheres compared to distribution of SIR-Spheres for Cases 4 and 11.

6.1.1 Inter-segmental particle distribution: boundary conditions

For eleven different cancer scenarios (including one healthy scenario) the particle distribution of SIR-Spheres was modelled (Case 1 to 11). The change in particle distribution (in %) with respect to the healthy scenario (Case 1) is visualized in 6.2. For two cases in particular (Cases 4 and 9), the distribution of Thera-Sphere particles was modelled as well. These particle distributions are compared to the distribution of the SIR-Spheres in Section 6.1.2.

In general, it can be stated that particle distribution tends to match flow split. To zoom in on this difference, the flow and particle distribution are compared side-to-side for one specific case in Figure 6.4, namely Case 2 ("Distributed", high tumour burden).

In Figure 6.5, four PRMs are visualized: the PRM for the Healthy scenario (in the top left corner) and the PRMs for the Distributed cases with varying cancer burden (Cases 2, 5 and 9). As is visible, the variation between these different PRMs is limited.

In Figure 6.6, six PRMs are displayed for the cases in which the cancer burden was restricted to the right lobe (Cases 3, 6 and 10). These figures are ordered from top to bottom for increasing cancer burden. On the right panels, Figures 6.6b, 6.6d and 6.6f, the area of the injection plane where injection leads to particle deposition in the cancerous branches is marked as red while the area of the injection plane where injection leads to deposition in the healthy tissue is marked as green. These figures are particularly helpful

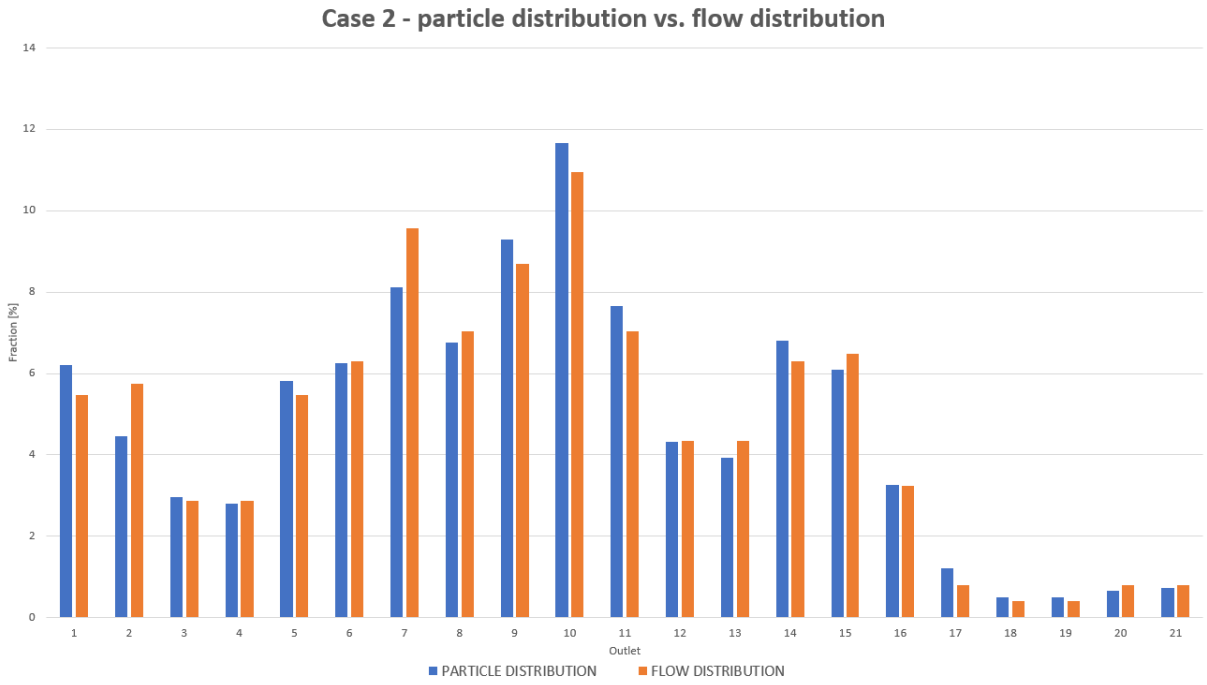

Figure 6.4: Side-to-side comparison of flow distribution and particle distribution for Case 2 (high tumour burden - distributed).

in evaluating target-specificity. As is visible, the area of tumour-targeting increases as tumour burden grows larger. Particularly, in 6.6f, particle deposition in healthy tissue only seems to occur when particles are injected at the outer left periphery of the injection plane.

However, if certain segments within the right lobe need to be targeted, then the attention needs to shift to Figures 6.6a, 6.6c and 6.6e. There, it is also visible that the injection regions for the left lobe (the blue-ish areas) grow increasingly smaller as tumour burden increases. The injection areas for outlets 6 to 21 grow larger from top to bottom. In Figure 6.6e, targeting zones such as 21 (pink zone) and 12 (yellow zone) grow larger, while, for example, the targeting zones for outlets 13 and 14 (orange-ish zone) noticeably decrease.

For Figure 6.7, the same structure was used as in Figure 6.6. These figures displayed the particle release maps for the cases in which tumours were restricted to the left lobe. On the right side of Figure 6.7, injection areas are marked red or green (depending whether they lead to deposition in the cancerous or healthy tissue, respectively), while, on the left side, injection zones for each of the outlets are coloured independently. In these six panels, the region of healthy tissue (outlets 6 to 21) is remarkably larger than in the previous case of the right lobe (Figure 6.6). This is only because the right lobe of the liver is in itself much larger than the left lobe. As is visible in Figures 6.7f, 6.7d and 6.7b, the targeting zone for the cancerous tissue grows larger as cancer burden increases. This is the same conclusion that was drawn for Figure 6.6.

Figures 6.6 and 6.7 both show that, as cancer burden increases, the targeting zones for

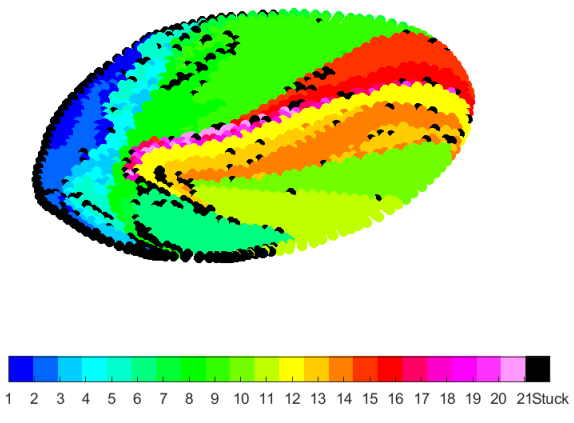

(a) Healthy

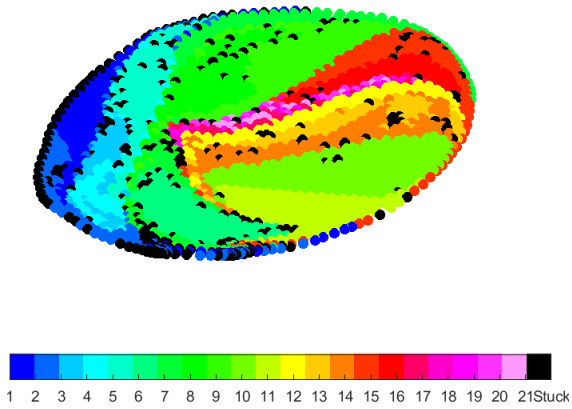

(b) Distributed - high tumour burden

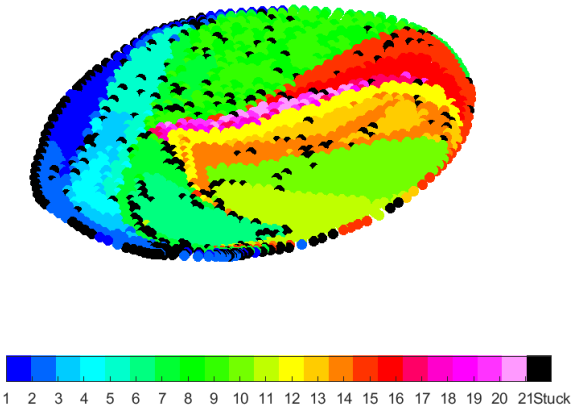

(c) Distributed - moderate tumour burden

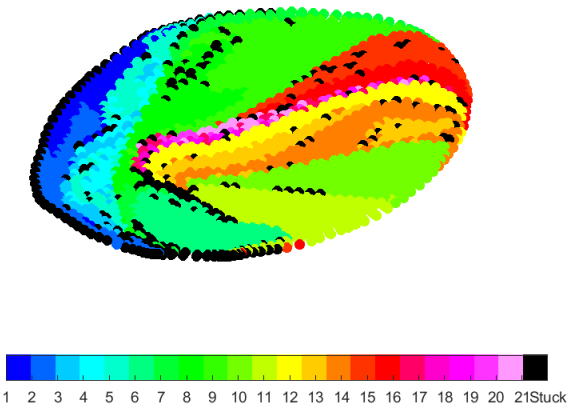

(d) Distributed - low tumour burden

Figure 6.5: Particle Release Maps for Cases 2, 5 and 9. Evaluating target-specificity for tumours distributed in the left lobe of the liver.

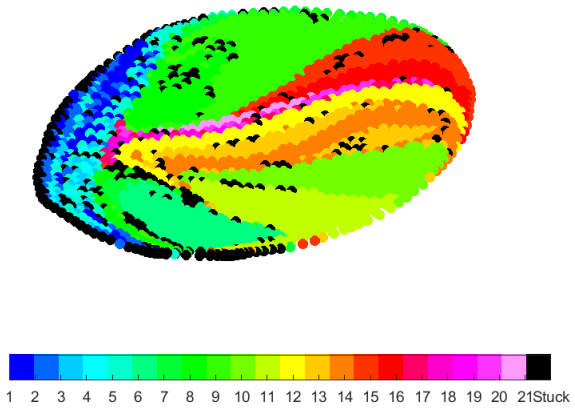

(a) PRM: low tumour burden - right lobe.

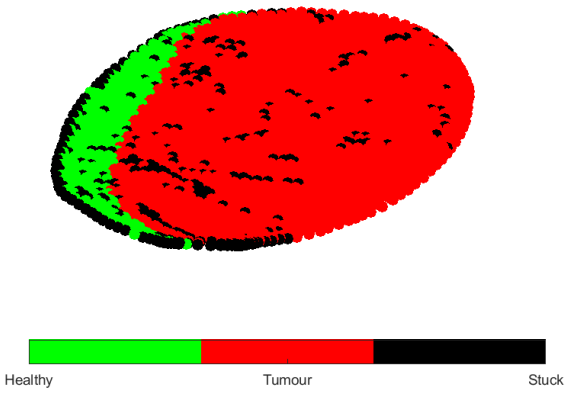

(b) Injection area for targeting - low burden.

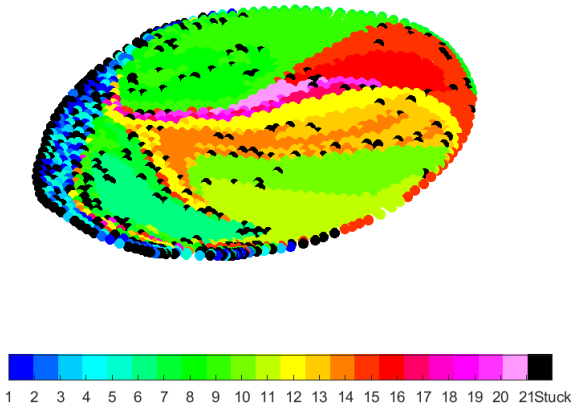

(c) PRM: moderate tumour burden - right lobe.

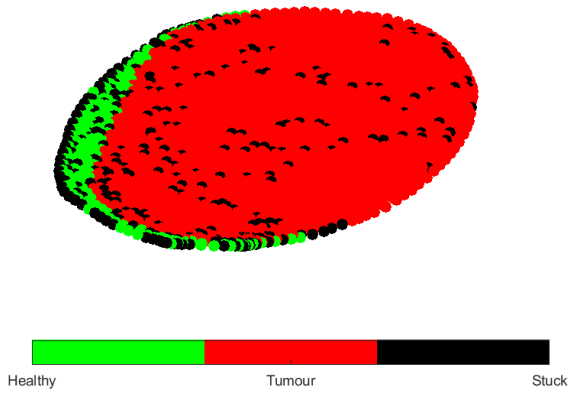

(d) Injection area for targeting - moderate burden.

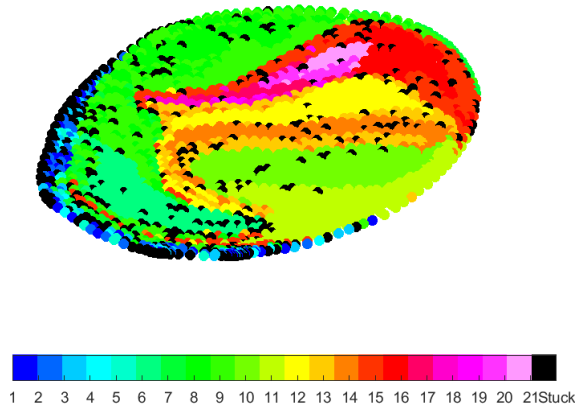

(e) PRM: high tumour burden - right lobe.

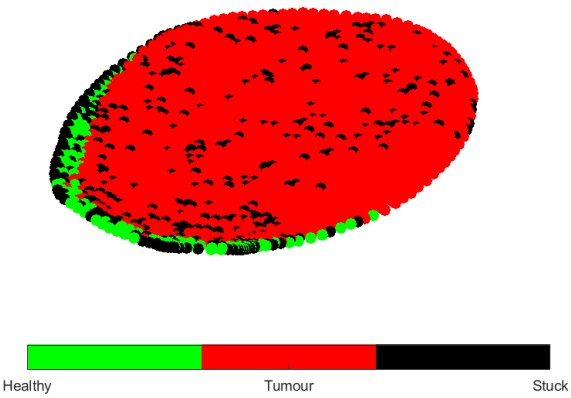

(f) Injection area for targeting - high burden.

Figure 6.6: Particle Release Maps for Cases 3, 6 and 10. In all of these cases, tumours were restricted to the right lobe only (outlets 6-21).

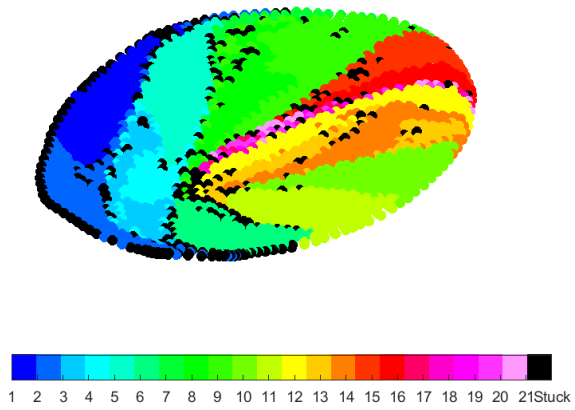

(a) Low tumour burden - left lobe

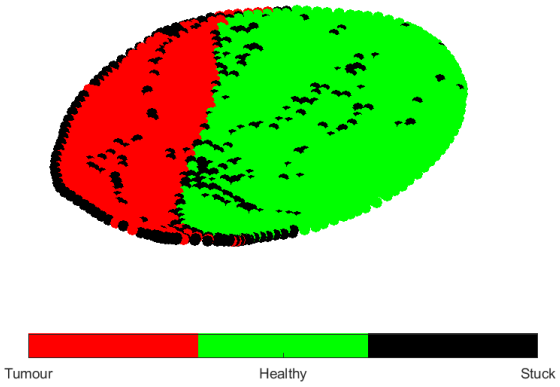

(b) Tumour-targeting

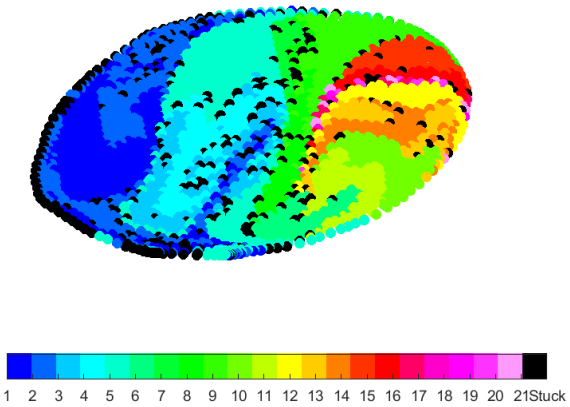

(c) Moderate tumour burden - left lobe

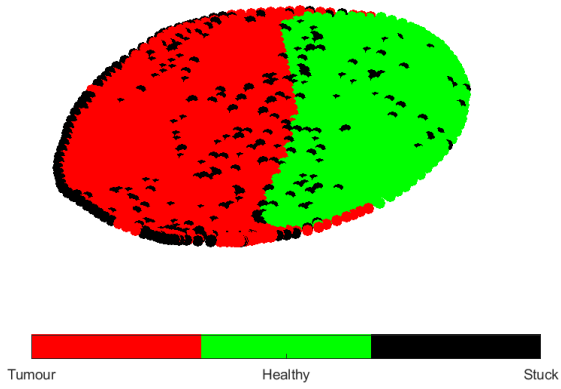

(d) Tumour-targeting

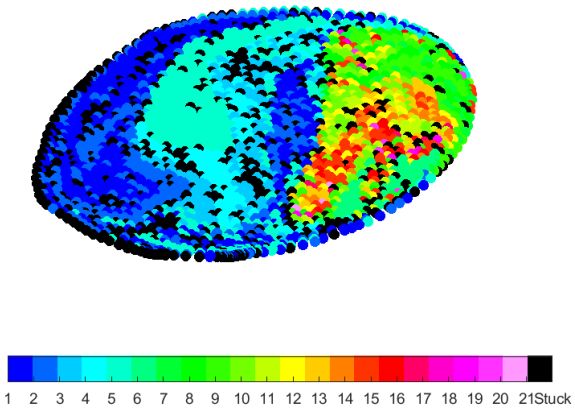

(e) High tumour burden - left lobe

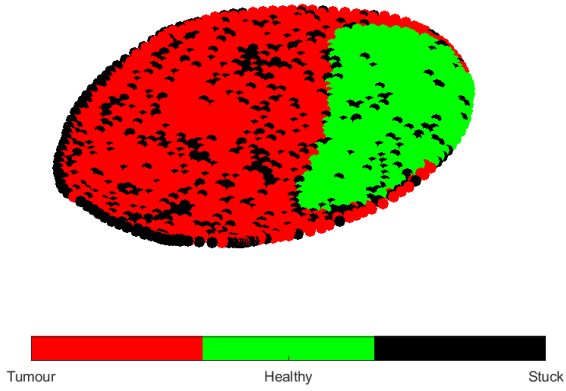

(f) Tumour-targeting

Figure 6.7: Particle Release Maps for Cases 4, 7 and 11. Evaluating target-specificity for tumours distributed in the left lobe of the liver.

the cancerous tissue grow larger. This can be attributed to the fact that increase in cancer burden is coupled with increase in arterial perfusion of the cancerous tissue, and since particle distribution tends to mimic overall flow distribution, it makes sense that larger fractions of particles will be deposited at the tumour tissue for these larger flow values. Although Figures 6.6 and 6.7 indicate that these tumour-targeting zones at the injection plane increase with higher cancer burden, it would be wrong to oversimplify these findings and state that targeting would become easier in the cases with higher cancer burden. As explained in Section 2.1.3, the work done in this thesis aimed to optimize the route of the drug particles between the injection site and target site. What happens at the target site itself at the micro-scale, is not considered here. It is obvious that the barriers of dense tumour mass and high interstitial pressure, which were first mentioned in Section 2.1.2, could prove to be a higher limit in the cases of high cancer burden compared to the cases with relatively low cancer burden.

The conclusion that can be drawn from all of the above is that it is of crucial importance to model the flow distribution throughout the arterial network as physiologically accurate as possible, because this flow distribution has an enormous impact on the eventual particle distribution. In this respect, the choice of boundary conditions becomes increasingly important. The boundary conditions implemented here (as described in Chapter 5), stand in stark contrast with Murray's Law, which does not take cancer burden into account in any way. Therefore, in Figure 6.8, Murray's Law is compared with the arterial perfusion model.

In Figure 6.8a, the general PRM for Murray's Law is given. To compare the outcome for Murray's Law with the outcome obtained by the arterial perfusion model, two specific cancer scenarios were considered: tumours constricted to the right lobe with moderate burden (Case 4) and tumours constricted to segment 4 with moderate burden (Case 8). It should be noted that the particle distribution for Murray's Law remains the same for these two cases, since the flow distribution calculated with Murray's Law depends only on the geometrical aspects of the arterial network and not on cancer burden. Therefore, the PRMs in Figures 6.8c and 6.8e reflect the same particle distribution as in Figure 6.8a. The only difference is that the segments are coloured in differently, depending whether they belong to cancerous tissue in that specific scenario or not.

In Figure 6.8, it is clear that the targeting regions differ between the two boundary conditions (left to right), even if the supposedly underlying pathological condition is the same. This difference is significant: as the PRM depends on the chosen boundary condition, this result creates an ambiguity that can make the clinician-in-charge inject particles in the wrong area of the injection plane. Since the clinical outcome of this therapy highly depends on the accuracy of the PRMs, questions can be asked regarding the validity of Murray's Law in these applications.

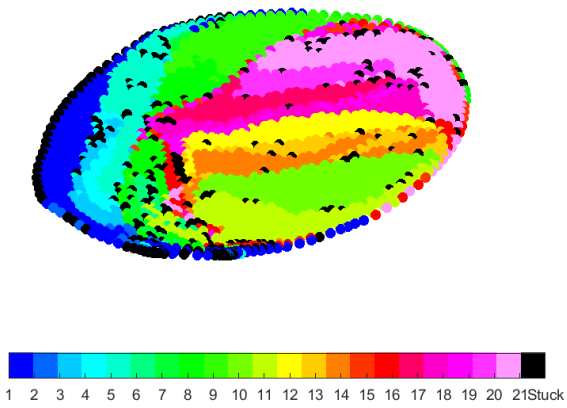

(a) PRM - Murray's Law.

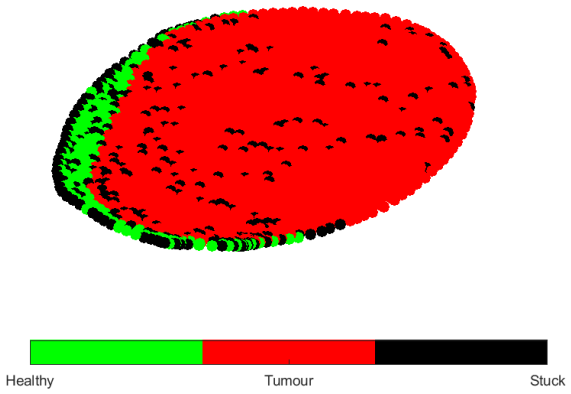

(b) Tumours constricted to the right lobe. Flow distribution calculated with arterial perfusion model (moderate burden).

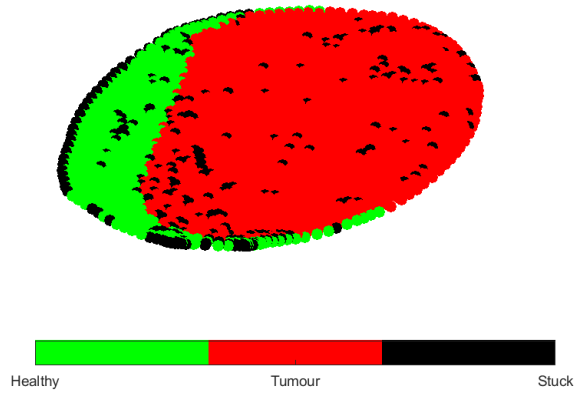

(c) Tumours constricted to the right lobe. Flow distribution calculated with Murray's Law.

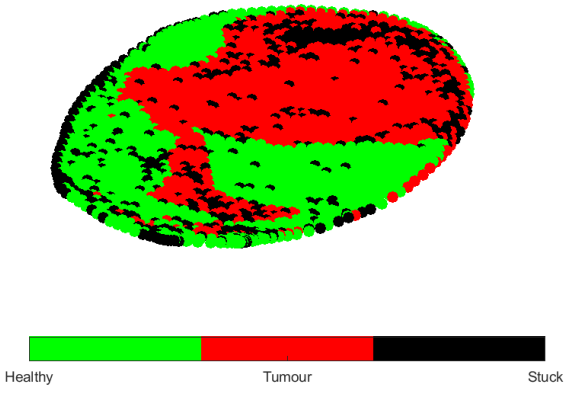

(d) Tumours constricted to Segment 4. Flow distribution calculated with arterial perfusion model (moderate burden).

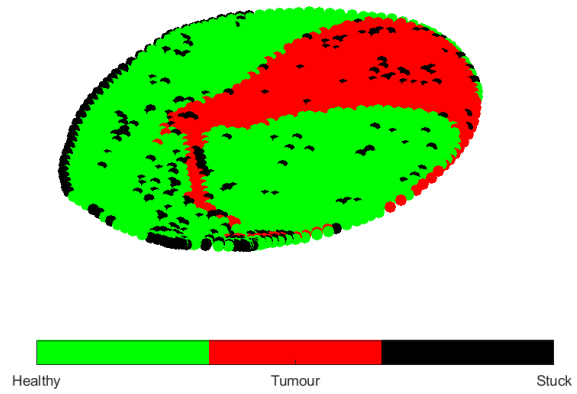

(e) Tumours constricted to Segment 4. Flow distribution calculated with Murray's Law.

Figure 6.8: Comparing Murray's Law (right column and top centre) with arterial perfusion model (left column). Middle row: tumour constricted to right lobe. Bottom: tumour constricted to Segment 4.

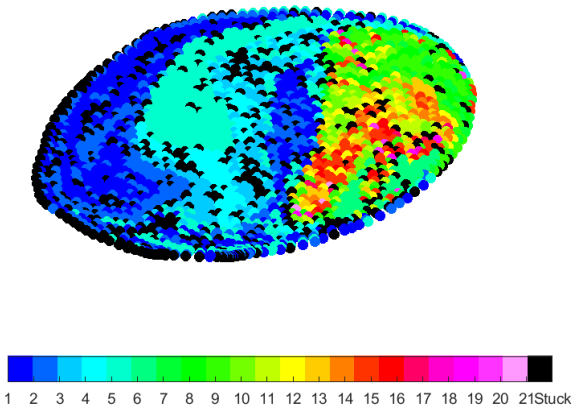

(a) High tumour burden - left lobe. Particles modelled are SIR-Spheres

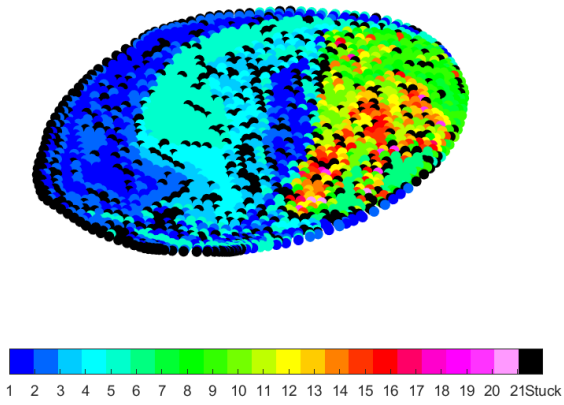

(b) High tumour burden - left lobe. Particles modelled are Thera-Spheres.

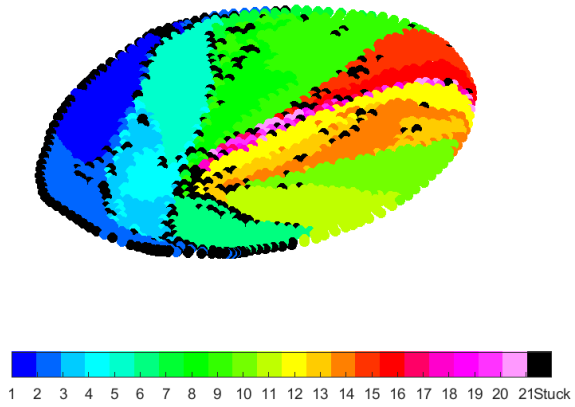

(c) Low tumour burden - left lobe. Particles modelled are SIR-Spheres.

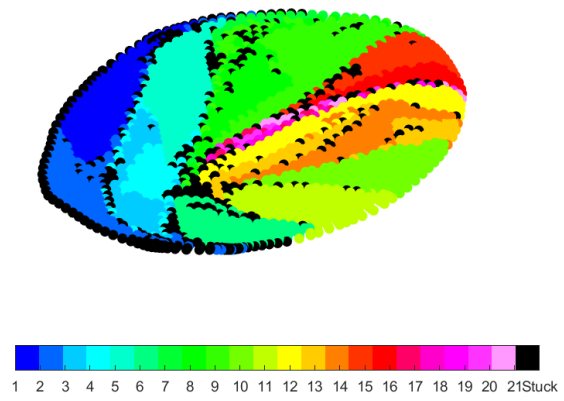

(d) Low tumour burden - left lobe. Particles modelled are Thera-Spheres.

Figure 6.9: Evaluating the influence of particle properties for left lobe cases

6.1.2 Inter-segmental particle distribution: particle properties

In Figure 6.9, the PRMs are shown for Case 4 (top) and Case 11 (down), modelled for the SIR-Spheres (left) and the denser Thera-Speheres (right). As is visible, the variations between the two particle types are minimal. The differences are much larger from top to bottom, which compares the high cancer burden of Case 4 to the low cancer burden of Case 11.

6.1.3 Intra-segmental particle distribution: Segment 4

In Sections 6.1.1 and 6.1.2 the focus was on the impact of boundary conditions and particle properties on the inter-segmental particle distribution. In this section, the focus is shifted to the intra-segmental particle distribution in Segment 4 for various cancer scenarios. Segment 4 was chosen because several arteries irrigating this segment looked very tortuous. Especially Outlets 17 to 19 looked particularly hard to reach. The arteries

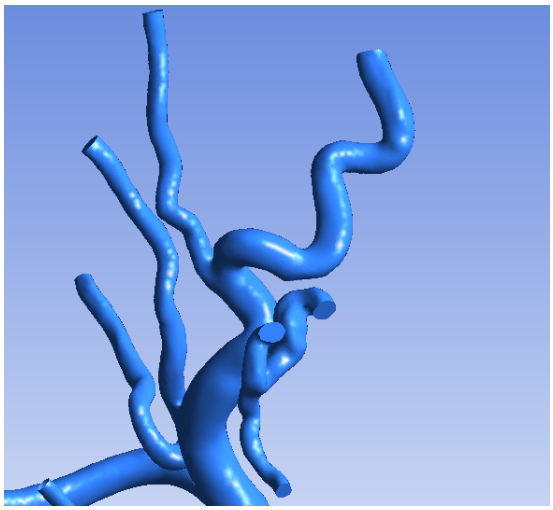

Figure 6.10: View of the tortuous arteries feeding Segment 4.

feeding Segment 4 are visualized in Figure 6.10. Furthermore, in Figure 5.24, it was noted that the discrepancy in flow distribution between Murray's law and the arterial perfusion model was notably large for all outlets perfusing Segment 4 (except for Outlet 16).

In Figure 6.11 the particle distribution (in % of total) for all outlets irrigating Segment 4 was visualized for several cancer scenarios: the healthy scenario is represented by the blue bars (Case 1), the scenario in which tumours were constricted to Segment 4 alone by the orange bars (Case 8, moderate burden), the scenario in which tumours were constricted to the right lobe by the yellow bars (Case 3, high burden) and the scenario in which tumours with high burden were spread throughout the entire liver by the cyan bars (Case 2, high burden). The grey bars denote the particle distribution as simulated with Murray's law, and therefore do not represent a specific cancer scenario. From Figure 6.11, it is obvious that Murray's law predicts a lower percentage of particles in Outlets 15 and 16 than all other scenarios and a higher percentage of particles in Outlets 17 to 21. In the distributed case especially, particle fractions drop as low as 0.5% in Outlets 17 to 21. In the right lobe case particle fractions are notably low as well, which indicate that targeting in these cases might become very difficult.

In Figure 6.12, the PRMs for three different cancer scenarios are visualized: in Figure 6.12b tumours were constricted to Segment 4, in Figure 6.12c tumour nodules were spread throughout the whole liver and in Figure 6.12d tumours were constricted to the right lobe. In Figure 6.12a the PRM for Murray's law is visualized. In all PRMs, the green section denotes the section of the inlet plane where particle injection leads to deposition in segments other than Segment 4. The other coloured sections each represent a specific outlet that irrigates Segment 4. As is visible in Figure 6.12a, Murray's law predicts a total injection area for Segment 4 that is smaller than the injection area predicted by the scenario in which tumours were constricted to Segment 4. However, Murray's law also predicts a total injection area that is larger than the injection areas predicted by the other two scenarios. More specifically, for Murray's law, Outlets 20 and 21 take

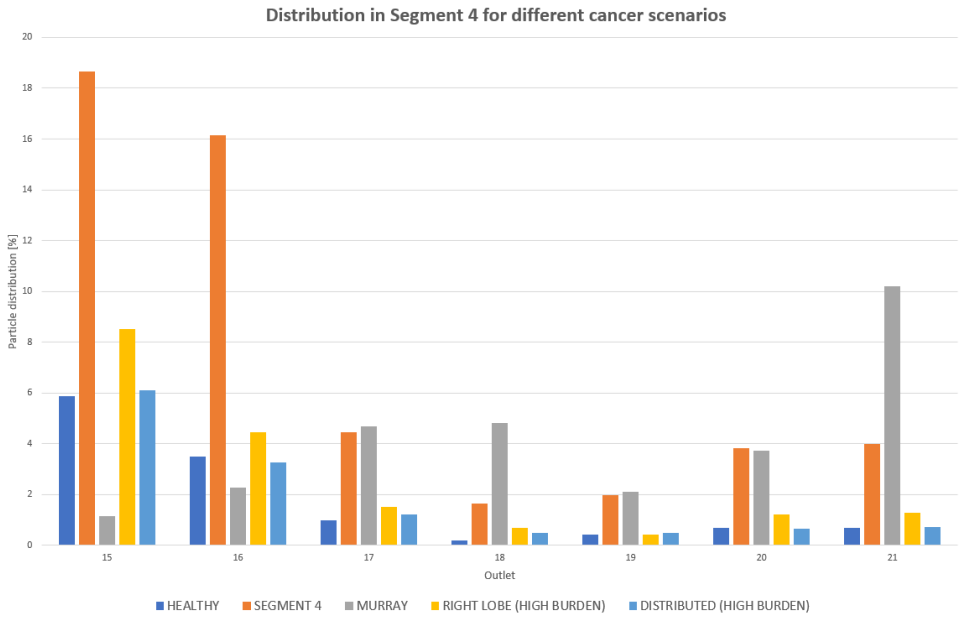

Figure 6.11: Particle distribution in Segment 4 for different cancer scenarios (healthy, Murray's Law, tumours constricted to right lobe (high, moderate and low burden) and tumours constricted to Segment 4).

up the largest fraction of the injection area, which indicates that targeting these outlets would be the easiest of all outlets irrigating Segment 4. This is not the case for all other scenarios. Especially in the scenario where tumour nodules are distributed throughout the whole liver, the injection areas for Outlets 20 and 21 are almost impossibly small. The scenario in which tumours were constricted to Segment 4 seems to predict a relatively large injection area for Segments 15, 16 and 21.

While the cancer scenarios considered in Figures 6.11 and 6.12 are still hypothetical, the results indicate that certain outlets could become very hard to target in certain scenarios. In the above scenarios, a homogeneous distribution of tumour nodules within one segment were assumed, meaning that all outlets were similarly affected. In the case that certain outlets would have a relatively higher local cancer burden than other outlets, the flow to these outlets would increase with respect to the less affected outlets. However, in this case perfusion parameters $k_{1,s}$, $k_{2,s}$ and $k^{\star}_{1,s}$ should not be assumed constant within one segment. This model is not complex enough to account for such tumour nodule distributions. This was already noted upon in Section 5.3.

End-note on the range of cancer burden

In general, it should be noted that for all of these results cases ranging from relatively high to relatively low cancer burden were considered. However, in Section 1.5, it was explained that the treatment options of HCC depend on the progression on the cancer. Specifically, it was mentioned that transarterial therapies such as TARE or TARE are usually only applied in the intermedium or advanced stage of HCC. Since these cases are

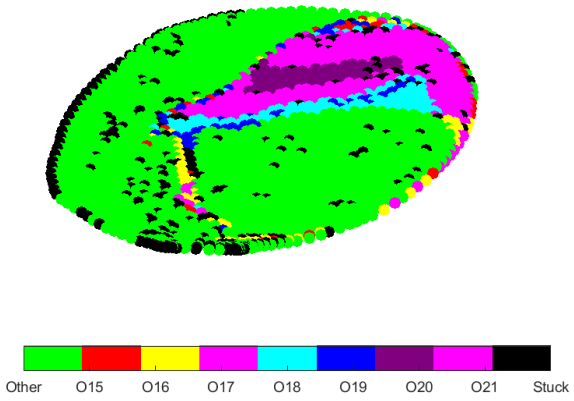

(a) Murray's law.

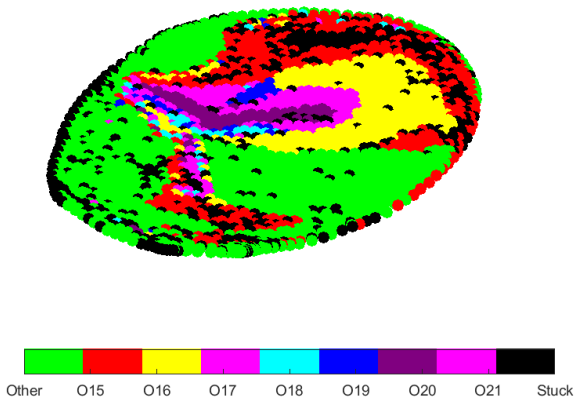

(b) Tumours constricted to Segment 4.

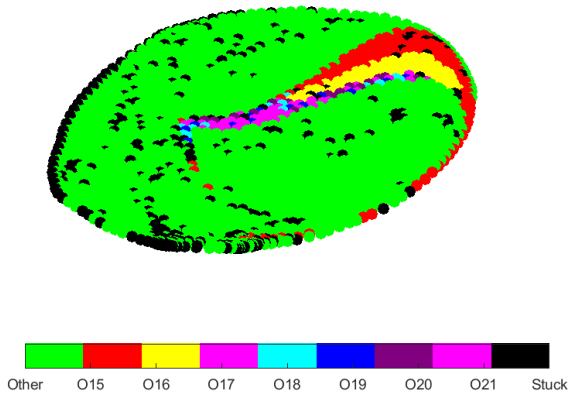

(c) Tumour nodules distributed throughout the liver.

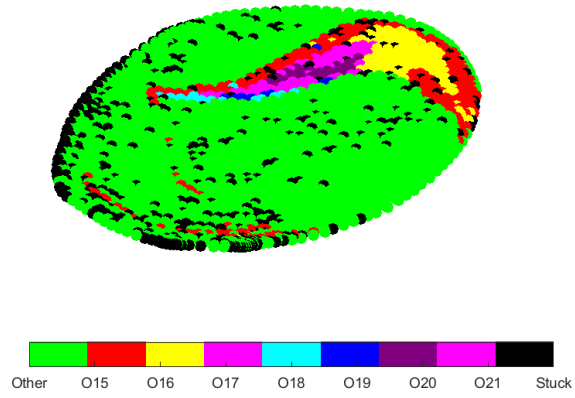

(d) Tumours constricted to right lobe (high burden).

Figure 6.12: Intra-segmental particle distribution for different cancer scenarios and boundary conditions

all hypothetical, it is entirely within the range of possibility that some of these cases would not have been treated with TARE or TACE in the first place, had they been presented as real-life scenarios to a clinician. However, the outset of this thesis was to investigate the impact of cancer burden on particle distribution, and therefore, the range of total cancer burden was set as large as possible.

6.2 General conclusions

In Section 6.1, the particle distribution was evaluated on different levels, namely on an inter-segmental level and an intra-segmental level particularly for Segment 4. From all the generated PRMs, it is clear that the choice of boundary conditions has a huge impact on both flow and particle distribution. Murray's law, which depends only on the geometrical aspects of the arterial network, does not discriminate between different cancer scenarios. The arterial perfusion model as proposed by Aramburu et al [2] predicts that both global and local cancer burden play an important role in assessing downstream particle distribution. Particle properties have an impact as well, although not as large as the choice of boundary conditions.

Moving forward, it is instrumental that a clear choice regarding boundary conditions is made. As Murray's law seems to inadequately assess the impact of cancer distribution and burden, the author's preferred boundary condition of choice is the arterial perfusion model.

6.3 Reflection and refinements

The strengths of this research lie in the consideration of a geometry that is both patient-specific and derived from a cirrhotic liver. As has been stated numerously throughout this thesis, the arterial network of a cirrhotic liver looks very different than the one of a healthy liver. For the specific geometry considered here, many of the arteries were torturous, which made certain segments almost unreachable. Furthermore, a wide range of cancer scenarios was considered. The arterial perfusion model as described by Aramburu et al [2] allows to differentiate between these different scenarios, which Murray's law does not. The resulting Particle Release Maps have shown that total tumour volume and nodule distribution throughout the liver play a crucial role in particle fate.

Of course, there is much room for improvement. The limitations of the arterial perfusion model as implemented in this thesis were already listed in Section 5.3. Although certain important measures (e.g. the perfusion characteristics, the total volume of the liver, etc.) were computed on a patient-specific basis, many of these limitations deal with the fact that not all measures were computed specifically for this patient. A considerable amount of volume and flow measures, which should be patient-specific, were adapted from literature.

Also, assumptions were made regarding the irrigation of certain liver segments. For example, it was assumed that one outlet of the computational domain could only perfuse one segment. This is a simplification that was done to reduce the complexity of the model. However, there is no physiological reason why this would be the case for all outlets, as this depends on the level where the outlets were cut off during the segmentation process performed by Claerebout. Perfusion parameters were also assumed to be constant in space and time for one segment, which probably does not reflect the true physiological nature of these parameters.

Moreover, the cancer scenarios considered in this thesis were purely hypothetical, as the patient's liver was cirrhotic but not specifically cancerous. Therefore, several hypothetical assumptions were also made regarding the development of tumour nodules in the liver segments. The next step in this workflow would undoubtedly be to focus on actual HCC patients. By mapping out the distribution of tumour nodules throughout the liver, a realistic cancer scenario can be obtained. Then, by repeating the workflow as outlined in Section 5.2, a more accurate boundary condition can be obtained.

Furthermore, the computational model can be expanded to investigate the impact of two-way coupling and fluid-structure interaction, which were discarded in Section 2.3.3 to simplify the model. Transient simulations could be run, taking into account the pulsatile nature of the perfusion parameters as determined in [2].

It stands to reason that for actual cancer patients, the methods of data acquisition described in Section 3.1 are inadequate. In general, the steps of the Computational Medical Management Program as described in Section 2.4 will need to be adapted in order to make the whole process smoother and less time-consuming. Preferably, certain aspects of the process, such as the delineation of the liver segments, should be automated. The eventual goal is the full implementation of the CMMP in clinical practice.

Chapter 7

Conclusions

HCC is the third leading cause of cancer-related deaths worldwide. Due to its high prevalence, HCC has become a global economic burden on society. The Barcelona Clinical Liver Cancer staging system tracks the progression of the cancer in several stages: very-early-stage, early-stage, intermedium, advanced and end-stage. For each of the stages a certain type of treatment is preferred. For the intermedium stage of HCC, the preferred treatment option is transarterial therapy. The main goal of these types of treatments is to cut off the blood supply of the tumour tissue by local administration of embolizing particles. Since tumour tissue in the liver is generally fed by arterial blood, obstruction of these arteries will lead to starvation and tumour cell death. The objective of these therapies is to maximize the deposit of particles at the tumour tissue and minimize the leak to healthy tissue. Numerical modelling plays a crucial role in this workflow as it is typically used to simulate the particle distribution in the patient-specific hepatic vasculature and determine the influence of parameters such as catheter placement, particle type, etc. Since particle distribution tends to mimic overall flow distribution, the choice of boundary conditions in these numerical models in crucial. Whereas in the past Murray's law has been used, this thesis implements an alternate boundary condition that more accurately describes the impact of cancer burden or, more specifically, the impact of the size and distribution of tumour nodules. The particle distribution for eleven different cancer scenarios is compared with Murray's law, with two specific scenarios also repeated for a different particle type. While particle properties also play a role in downstream particle distribution, the results show that both global and local cancer burden have a considerable impact on the particle distribution throughout the arterial network. This means that the choice of boundary conditions is crucial in the development of accurate numerical models and that, going forward, a clear choice regarding the use of boundary conditions should be made. Since the arterial perfusion model discriminates between the different cancer scenarios and Murray's law does not, the author's preferred choice of boundary conditions is the arterial perfusion model.

Bibliography

[1] Y. A. Ghouri, I. Mian, and J. H. Rowe, "Review of hepatocellular carcinoma: Epidemiology, etiology and carcinogenesis," *Journal of Carcinogenesis*, vol. 16, no. 1, 2017, doi:10.4103/jcar.JCar-9-16.

[2] J. Aramburu, R. Anton, A. Rivas, J. C. Ramos, B. Sangro, and J. I. Bilbao, "Liver cancer arterial perfusion modelling and CFD boundary conditions methodology: a case study of the haemodynamics of a patient-specific hepatic artery in literature-based healthy and tumour-bearing liver scenarios," *International Journal for Numerical Methods in Biomedical Engineering*, vol. 32, no. 11, 2016, doi: 10.1002/cnm.2764.

[3] A. Tang, O. Hallouch, V. Chernyak, A. Kamaya, and C. B. Sirlin, "Epidemiology of hepatocellular carcinoma: target population for surveillance and diagnosis," *Abdominal Radiology*, vol. 43, no. 1, pp. 13–25, 2018, doi:10.1007/s00261-017-1209-1.

[4] H. B. El-Serag and K. L. Rudolph, "Hepatocellular carcinoma: Epidemiology and molecular carcinogenesis," *Gastroenterology*, vol. 132, no. 7, pp. 2557–2576, 2007, doi: 10.1053/j.gastro.2007.04.061.

[5] A. Waghray, A. R. Murali, and K. N. Menon, "Hepatocellular carcinoma: From diagnosis to treatment," *World Journal of Hepatology*, vol. 7, no. 8, pp. 1020–1029, 2015.

[6] J. Trojan, S. Zangos, and A. A. Schnitzbauer, "Diagnostics and treatment of hepatocellular carcinoma in 2016: Standards and developments," *Visceral Medicine*, vol. 32, no. 2, pp. 116–120, 2016, doi: 10.1159/000445730.

[7] A. Villanueva, "Hepatocellular carcinoma," *New England Journal of Medicine*, vol. 380, pp. 1450–1462, 2019, doi:10.1056/NEJMra1713263.

[8] S. D. Smedt, "Nanomedicines and cutting edge technologies for drug delivery," Department of Pharmaceutical Sciences, UGENT, 2018.

[9] T. Lammers, F. Kiessling, W. E. Hennink, and G. Storm, "Drug targeting to tumors: Principles, pitfalls and (pre-) clinical progress," *Journal of Controlled Release*, vol. 161, no. 2, pp. 175–187, 2011, doi: 10.1016/j.jconrel.2011.09.063.

[10] C. Kleinstreuer, Y. Feng, and E. Childress, "Drug-targeting methodologies with applications: A review," *World Journal of Clinical Cases*, vol. 2, no. 12, pp. 742–756, 2014, doi: 10.12998/wjcc.v2.i12.742.

[11] M. E. Hanami *et al.*, "SPECT/CT with 99m-Tc-MAA in radioembolization in patients with hepatocellular cancer," *The Journal of Nuclear Medicine*, vol. 50, pp. 688–692, 2009, doi: 10.2967/jnumed.108.058347.

[12] A. Marusyk, V. Almendro, and K. Polyak, "Intra-tumour heterogeneity: a looking glass for cancer?" *Nature Reviews Cancer*, vol. 12, no. 5, pp. 323–334, 2012, doi: 10.1038/nrc3261.

[13] J. Aramburu, R. Anton, A. Rivas, J. C. Ramos, B. Sangro, and J. I. Bilbao, "The role of angled-tip microcatheter and microsphere injection velocity in liver radioembolization: A computational particle-hemodynamics study," *International Journal for Numerical Methods in Biomedical Engineering*, vol. 33, no. 12, 2017, doi: 10.1002/cnm.2895.

[14] E. J. Sanchez, "Targeted drug delivery for liver cancer: a patient-specific computational model of the particle transport during radio-embolisation," Master's thesis, UGent, 2018.

[15] C. Kleinstreuer, C. A. Basciano, E. M. Childress, and A. S. Kennedy, "A new catheter for tumor targeting with radioactive microspheres in representative hepatic artery systems. Part I: Impact of catheter presence on local blood flow and microsphere delivery," *Journal of Biomechanical Engineering*, vol. 134, no. 5, 2012, doi: 10.1115/1.4006684.

[16] E. Childress and C. Kleinstreuer, "Impact of fluid-structure interaction on direct tumor-targeting in a representative hepatic artery system," *Annals of Biomedical Engineering*, vol. 42, no. 3, pp. 461–474, 2014, doi: 10.1007/s10439-013-0910-7.

[17] Radiology assistant: Anatomy of the liver segments. Accessed: 2019-02-28. [Online]. Available: http://www.radiologyassistant.nl/en/p4375bb8dc241d/anatomy-of-the-liver-segments.html

[18] M. Darcy, H. Royal, L. Uliel, D. A. Zuckerman, A. Sharma, and N. E. Saad, "From the angio suite to the -camera: Vascular mapping and 99m-Tc-MAA hepatic perfusion imaging before liver radioembolization: A comprehensive pictorial review," *Journal of Nuclear Medicine*, vol. 53, no. 11, pp. 1736–47, 2012.

[19] A. Kennedy *et al.*, "Recommendations for radioembolization for hepatic malignancies using yttrium-90 microsphere brachytherapy: a consensus panel report from the radioembolization brachytherapy oncology consortium," *International journal of radiation oncology, biology, physics*, vol. 68, no. 1, pp. 13–23, 2007.

[20] J. Balogh *et al.*, "Hepatocellular carcinoma: a review," *Journal of Hepatocellular Carnicoma*, vol. 3, pp. 41–53, 2016, doi: 10.2147/JHC.S61146.

[21] H. B. El-Serag, "Hepatocellular carcinoma," *The New England Journal of Medicine*, vol. 365, no. 12, pp. 1118–1127, 2011, doi: 10.1056/NEJMra1001683.

[22] J.-H. Kao, "Hepatitis B vaccination and the prevention of hepatocellular carcinoma," *Clinical Gastroenterology*, vol. 29, no. 6, pp. 907–917, 2015, doi: 10.1016/j.bpg.2015.09.011.

[23] K. Schütte, F. Balbisi, and P. Malfertheiner, "Prevention of hepatocellular carcinoma," *Gastroinestinal Tumors*, vol. 3, no. 1, pp. 37–43, 2016, doi: 10.1159/000446680.

[24] K. Schütte *et al.*, "Delayed diagnosis of hcc with chronic alcoholic liver disease," *Liver cancer*, vol. 1, no. 3, pp. 257–266, 2012, doi: 10.1159/000343840.

[25] L. Charach, L. Zusmanovitch, and G. Charach, "Heptacellular carcinoma. part 2: Clinical presentation and diagnosis," *Journal of Hepatology*, vol. 5, no. 1, pp. 81–88, 2017.

[26] G. A. Koudehi, "Targeted drug delivery for liver cancer: modeling drug carrier transport for to optimize treatment efficacy," Master's thesis, UGent, 2016.

[27] J. Fang, H. Nakamura, and H. Maeda, "The EPR effect: Unique features of tumor blood vessels for drug delivery, factors invoolved, and limitations and augmentation of the effect," *Advanced Drug Delivery Reviews*, vol. 63, no. 3, pp. 136–151, 2011, doi: 10.1016/j.addr.2010.04.009.

[28] H.-J. Li *et al.*, "Smart superstructures with ultrahigh ph-sensitivity for targeting acidic tumor microenvironment: Instantaneous size switching and improved tumor penetration," *ACS Nano*, vol. 10, no. 7, pp. 6753–6761, 2016, doi:10.1021/acsnano.6b02326.

[29] J. Namur *et al.*, "Embolizatin of hepatocellular carcinoma with drug-eluted beads: Doxorubicin tissue concentration and distribution in patient liver explants," *Journal of Hepatology*, vol. 55, no. 6, pp. 1332–1338, 2011, doi: 10.1016/j.jhep.2011.03.024.

[30] R. Lencioni, P. Patruzzi, and L. Crocetti, "Chemoembolization of hepatocellular carcinoma," *Seminars in Interventional Radiology*, vol. 30, no. 1, pp. 3–11, 2013, doi: 10.1055/s-0033-1333648.

[31] H.-C. Kim, "Radioembolization for the treatment of hepatocellular carcinoma," *Clinical and Molecular Hepatology*, vol. 23, no. 2, pp. 109–114, 2017, doi: 10.3350/cmh.2017.0004.

[32] C. Mosconi, A. Cappelli, C. Pettinato, and R. Golfieri, "Radioembolization with yttrium-90 microspheres in hepatocellular carcinoma: Role and perspectives," *World Journal of Hepatology*, vol. 7, no. 5, pp. 738–752, 2015, doi: 10.4254/wjh.v7.i5.738.

[33] H. Woo and J. Heo, "Transarterial chemoembolization using drug eluting beads for the treatment of hepatocellular carcinoma: Now and future," *Clinical and Molecular Hepatology*, vol. 21, no. 4, pp. 344–348, 2015, doi: 10.3350/cmh.2015.21.4.344.

[34] W. Wondergem *et al.*, "99mtc-macroaggregated albumin poorly predicts the intrahepatic distribution of 90y resin microspheres in hepatic radioembolization." *Journal of Nuclear Medicine*, vol. 54, no. 8, pp. 1294–1301, 2013, doi: 10.2967/jnumed.112.117614.

[35] M. T. Reinders, M. L. Smits, C. van Roekel, and A. J. Braat, "Holmium-166 microsphere radioembolization of hepatic malignancies," *Seminars in Nuclear Medicine*, vol. 49, no. 3, 2019.

[36] D. Y. Kim and K.-H. Han, "Transarterial chemoembolization versus transarterial radioembolization in hepatocellular carcinoma: optimization of selecting treatment modality," *Hepatology International*, vol. 10, no. 6, pp. 883–892, 2009, doi: 10.1007/s12072-016-9722-9.

[37] J. Aramburu, R. Anton, A. Rivas, J. C. Ramos, B. Sangro, and J. I. Bilbao, "Computational particle-haemodynamics analysis over liver radioembolization pretreatment as an actual treatment surrogate," *International Journal for Numerical Methods in Biomedical Engineering*, vol. 33, no. 2, 2016, doi: 10.1002/cnm.2791.

[38] S. Jernigan, J. Osborne, C. Mirek, and G. Buckner, "Selective internal radiation therapy: quantifying distal penetration and distribution of resin and glass microspheres in a surrogate arterial model," *Journal of Vascular and Interventional Radiology*, vol. 26, no. 6, pp. 897–904, 2015, doi: 10.1016/j.jvir.2015.02.022.

[39] *ANSYS Fluent Theory Guide*. Ansys Inc., 2013.

[40] C. Kleinstreuer, C. A. Basciano, E. M. Childress, and A. S. Kennedy, "A new catheter for tumor targeting with radioactive microspheres in representative hepatic artery systems. Part II: Solid tumor-targeting in a patient-inspired hepatic artery system," *Journal of Biomechanical Engineering*, vol. 134, no. 5, 2012.

[41] G. Peeters *et al.*, "A multilevel modeling framework to study hepatic perfusion characteristics in case of liver cirrhosis," *Journal of Biomedical Engineering*, vol. 137, no. 5, 2015, doi: 10.1115/1.4029280.

[42] C. Debbaut *et al.*, "From vascular corrosion cast to electrical analog model for the study of human liver hemodynamics and perfusion," *IEEE Transactions on Biomedical Engineering*, vol. 58, no. 1, 2011, doi: 10.1109/TBME.2010.2065229.

[43] *ANSYS ICEM CFD User Manual.* Ansys Inc., 2012.

[44] C. Bascanio, C. Kleinstreuer, A. S. Kennedy, W. A. Dezarn, and E. Childress, "Computer modeling of controlled microsphere release and targeting in a representative hepatic artery system," *Annals of Biomedical Engineering*, vol. 38, no. 5, pp. 1862–1879, 2010, doi: 10.1007/s10439-010-9955-z.

[45] J. Buchanan, Jr., C. Kleinstreuer, and J. Comer, "Rheological effects on pulsatile hemodynamics in a stenosed tube," *Computers and Fluids*, vol. 29, no. 6, pp. 695–724, 2000, 10.1016/S0045-7930(99)00019-5.

[46] T. Sherman, "On connecting large vessels to small. the meaning of murray's law," *Journal of General Physiology*, vol. 78, no. 4, 1981, doi: 10.1085/jgp.78.4.4319.

[47] S. Özhan Oktar *et al.*, "Doppler sonographic evaluation of hemodynamic changes in colorectal liver metastases relative to liver size," *Journal of Ultrasound in Medicine*, vol. 25, no. 5, pp. 575–582, 2006.

[48] Brian's radiology diary: Liver vasculature and segmentation in ct scan. Accessed: 2019-02-28. [Online]. Available: https://briansradiologylearningdiary.wordpress.com/2017/12/31/liver-vasculature-and-segmentation-in-ct-scan/

FACULTY OF ENGINEERING AND ARCHITECTURE

Targeted drug delivery for liver cancer: modelling the impact of cancer burden on the particle distribution in a patient-specific cirrhotic liver

Tim Bomberna
Student number: 01404812

Supervisors: Prof. dr. ir. Charlotte Debbaut, Prof. dr. ir. Patrick Segers
Counsellor: Ghazal Adeli Koudehi

Master's dissertation submitted in order to obtain the academic degree of
Master of Science in Biomedical Engineering

Academic year 2018-2019

GHENT UNIVERSITY